REPORT DOCUMENTATION PAGE

Form Approved OMB NO. 0704-0188

1. REPORT DATE (DD-MM-YYYY)	2. REPORT TYPE	3. DATES COVERED (From - To)
28-07-2015	Ph.D. Dissertation	-

4. TITLE AND SUBTITLE	5a. CONTRACT NUMBER
Step-Tapered Active-Region Mid-Infrared Quantum Cascade Lasers and Novel Fabrication Processes for Buried Heterostructures	
	5b. GRANT NUMBER
	W911NF-12-C-0033
	5c. PROGRAM ELEMENT NUMBER
	665502

6. AUTHORS	5d. PROJECT NUMBER
Chun-Chieh Chang	
	5e. TASK NUMBER
	5f. WORK UNIT NUMBER

7. PERFORMING ORGANIZATION NAMES AND ADDRESSES	8. PERFORMING ORGANIZATION REPORT NUMBER
Intraband LLC 200 N. Prospect Ave. Madison, WI　　　　　53726 -4027	

9. SPONSORING/MONITORING AGENCY NAME(S) AND ADDRESS (ES)	10. SPONSOR/MONITOR'S ACRONYM(S)
U.S. Army Research Office P.O. Box 12211 Research Triangle Park, NC 27709-2211	ARO
	11. SPONSOR/MONITOR'S REPORT NUMBER(S)
	60653-EL-ST2.7

12. DISTRIBUTION AVAILIBILITY STATEMENT

Approved for public release; distribution is unlimited.

13. SUPPLEMENTARY NOTES

14. ABSTRACT

The active region of conventional 4.5 – 5.0 micron-emitting QCLs is composed of quantum wells and barriers of fixed alloy composition. They suffer severe carrier leakage from the upper laser level, evidenced by low characteristic temperatures for both threshold-current density and slope efficiency over a wide range of heatsink temperatures above room temperature. To suppress carrier leakage, the energy separation between the upper laser level and the next-higher energy state, E54 (or E43) needs to be increased. Here, we propose 4.8 micron-emitting, step-tapered active-region (STA) QCLs for complete suppression of carrier leakage. Due to the stepwise tapering of

15. SUBJECT TERMS

quantum cascade lasers, conduction-band engineeering, phase-locked arrays, buried heterostructures

16. SECURITY CLASSIFICATION OF:			17. LIMITATION OF ABSTRACT	15. NUMBER OF PAGES	19a. NAME OF RESPONSIBLE PERSON
a. REPORT	b. ABSTRACT	c. THIS PAGE	UU		Dan Botez
UU	UU	UU			19b. TELEPHONE NUMBER
					608-231-3432

Step-Tapered Active-Region Mid-Infrared Quantum Cascade Lasers and Novel Fabrication Processes for Buried Heterostructures

ABSTRACT

The active region of conventional $4.5 - 5.0$ micron-emitting QCLs is composed of quantum wells and barriers of fixed alloy composition. They suffer severe carrier leakage from the upper laser level, evidenced by low characteristic temperatures for both threshold-current density and slope efficiency over a wide range of heatsink temperatures above room temperature. To suppress carrier leakage, the energy separation between the upper laser level and the next-higher energy state, E54 (or E43) needs to be increased. Here, we propose 4.8 micron-emitting, step-tapered active-region (STA) QCLs for complete suppression of carrier leakage. Due to the stepwise tapering of barrier heights in the active region, the STA-QCLs not only possess a significantly large E54 (or E43) value, but the reduction in E54 (or E43) due to Stark shift is also minimized. By comparison with state-of-the-art shallow-well TA-QCLs, the STA-QCLs have higher gain cross-section when the linewidth broadening due to interface roughness is considered. Furthermore, by reducing the total number of interfaces, and the number of high-strained layers in the laser core, the thermal resistance of STA-QCLs is only about half that for shallow-well TA-QCLs. Due to the combination of suppression of carrier leakage and less self-heating, the projected single-facet, CW maximum walllplug efficiency of 4.8 micron–emitting STA-QCLs is 25% at room temperature, close to published predicted limits for 4.8 micron–emitting QCLs, which makes the STA-QCLs more suitable for long-term, reliable operation at high (more than 0.5 W) CW powers.

Novel fabrication processes for buried-heterostructure (BH) quantum cascade devices have been developed. These processes mainly involve a deep-trench formation step by etching, followed by a regrowth step to achieve electrical insulation or the designed refractive-index step. A chemical polishing (CP) step can be incorporated in these processes after the regrowth to improve device planarity. Specifically, we have demonstrated a fabrication process of BH-QCLs by using non-selective regrowth of iron-doped InP and planarization via CP. This method provides a more flexible route to realizing BH-QCLs than the conventional process. Moreover, new processes for achieving on-chip, large-emitting aperture QCL phase-locked arrays based on etching and regrowth are also reported in this work.

Step-Tapered Active-Region Mid-Infrared Quantum Cascade Lasers and Novel Fabrication Processes for Buried Heterostructures

by

Chun-Chieh Chang

A dissertation submitted in partial fulfillment of
the requirements for the degree of

Doctor of Philosophy
(Electrical and Computer Engineering)

at the
University of Wisconsin-Madison
2015

Date of final oral examination: June 10 2015
Month and year degree to be awarded: August 2015

The dissertation is approved by the following members of the Final Oral Committee:

Dan Botez, Professor, Electrical and Computer Engineering
Irena Knezevic, Professor, Electrical and Computer Engineering
Thomas F. Kuech, Professor, Chemical and Biological Engineering
Zhenqiang Ma, Professor, Electrical and Computer Engineering
Luke J. Mawst, Professor, Electrical and Computer Engineering

Step-Tapered Active-Region Mid-Infrared Quantum Cascade Lasers and Novel Fabrication Processes for Buried Heterostructures

Chun-Chieh Chang

Under the supervision of Professor Dan Botez

At the University of Wisconsin-Madison

Abstract

The active region of conventional $4.5 - 5.0$ μm-emitting QCLs is composed of quantum wells and barriers of fixed alloy composition. They suffer severe carrier leakage from the upper laser level, evidenced by low characteristic temperatures for both threshold current density and slope efficiency over a wide range of heatsink temperatures above room temperature. To suppress carrier leakage, the energy separation between the upper laser level and the next-higher energy state, E_{54} (or E_{43}) needs to be increased. Here, we propose 4.8 μm-emitting, step-tapered active-region (STA) QCLs for complete suppression of carrier leakage. Due to the stepwise tapering of barrier heights in the active region, the STA-QCLs not only possess a significantly large E_{54} (or E_{43}) value, but the reduction in E_{54} (or E_{43}) due to Stark shift is also minimized. In comparison with the state-of-the-art shallow-well TA-QCLs, the STA-QCLs have higher gain cross-section

when the linewidth broadening due to interface roughness is considered. Furthermore, by reducing the total number of interfaces, and the number of high-strained layers in the laser core, the thermal resistance of STA-QCLs is only about half of that for shallow-well TA-QCLs. Due to the combination of suppression of carrier leakage and less self-heating, the projected single-facet, CW maximum walllplug efficiency of 4.8 μm–emitting STA-QCLs is ≥ 25% at room temperature, close to published predicted limits for 4.8 μm–emitting QCLs, which makes the STA-QCLs more suitable for long-term, reliable operation at high (≥ 0.5 W) CW powers.

Novel fabrication processes for buried-heterostructure (BH) quantum cascade devices have been developed. These processes mainly involve a deep-trench formation step by etching, followed by a regrowth step to achieve electrical insulation or designed refractive-index step. A chemical polishing (CP) step can be incorporated in these processes after the regrowth to improve device planarity. Specifically, we have demonstrated a fabrication process of BH-QCLs by using non-selective regrowth of iron-doped InP and planarization via CP. This method provides a more flexible route to realizing BH-QCLs than the conventional process. Moreover, new processes for making on-chip, large-emitting aperture QCL arrays based on etching and regrowth are also reported in this work.

Acknowledgement

First and foremost, the author sincerely thanks his research advisor, Prof. Dan Botez for the opportunity to perform research under his supervision, and for his rigorous training, support, and constant encouragement. The author would very much like to thank Prof. Luke J. Mawst, and Prof. Thomas F. Kuech, for the opportunities they have given over the years, and for their guidance, support, and valuable suggestions. The author also wishes to thank his dissertation committee members, Prof. Irena Knezevic, and Prof. Zhenqiang Ma, for their valuable comments and suggestions.

The author acknowledges his coworkers for their contributions to this dissertation. Jeremy Kirch performed the crystal growth of semiconductor materials. Toby Garrod and Yanbing Shi verified the updated k•p code. Dr. Lei Wan prepared the diblock copolymer templates. Brian Zutter and Phillip Buelow performed the chemical polishing. Colin Boyle and Honghyuk Kim helped with the device fabrication of many QCL-related projects. Tom Earles and Don Lindberg III performed the device characterization. Rebecca Bauer, Dan Christensen, Quinn Leonard, Hal Giles, Kurt Kupcho, Bryan Cord, Ning Cao, and Yaguang Lian offered technical support in the cleanroom. The author have also benefited from many of his colleagues, including Jae Cheol Shin, Sangho Kim, TaeWan Kim, Steven Ruder, Kevin Schulte, Monica Wiedmann, Chris Sigler, Ayushi Rajeev, Kevin Oresick, Yinggang Huang, Xiaodong Wang, Tsung-Hsing Hsu, Edwin Ramayya, and Tzu-Hsuan Chang.

Last but not least, the author would like to thank his families, including his parents and siblings, for their unconditional love and support. Finally, the author would like to dedicate this dissertation to his wife Dr. Mei-Ling Kuo.

Table of Contents

Chapter 1   Introduction

  1.1 Introduction

  1.2 Thesis overview

Chapter 2   Background for Mid-Infrared Quantum Cascade Lasers

  2.1 Introduction

  2.2 Rate equation

  2.3 Temperature dependence

  2.4 Longitudinal optical (LO) phonon scattering

Chapter 3   Step-Tapered Active-Region Mid-Infrared Quantum Cascade Lasers

  3.1 Introduction

  3.2 Background

      3.2.1 Conventional QCLs

      3.2.2 Deep-Well (DW) QCLs

      3.2.3 Tapered active-region (TA) QCLs

      3.2.4 Linear tapered active-region (Linear-TA) QCLs

  3.3 Step-tapered active-region (STA) QCLs

List of Figures

List of Tables

Table

CHAPTER ONE

INTRODUCTION

1.1 Introduction

Quantum cascade lasers (QCLs) [1] are electrically pumped semiconductor coherence light sources. Unlike conventional semiconductor diode lasers where light emission is generated from the electron-hole recombination across the band gap, the laser action in QCLs is based on the electronic transition between two quantized subbands in a multiple-quantum-well heterostructure. The emission wavelength of QCLs is therefore determined by quantum design based on band-gap engineering [2] rather than the band gap of constituent materials, and can be tailored at will by changing the layer thicknesses of quantum wells and barriers in the active region.

The light amplification in a semiconductor superlattice was first proposed by Kazarinov and Suris in 1971 [3]. In their theoretical model, a semiconductor superlattice composed of one-dimensional periodic quantum-well structure is used as the gain medium. At a certain bias, population inversion can be achieved between the excited state in one well and the ground state in the downstream adjacent well. Light amplification between these two states is then obtained due to photon-assisted tunneling through the barrier. In 1985, intersubband absorption was experimentally observed within the conduction band of a GaAs quantum well by West and Eglash [4]. A year later, Capasso et al. [5] reported the observation of sequential resonant tunneling in a multiple-quantum-well structure based on $Al_{0.48}In_{0.52}As/Ga_{0.47}In_{0.53}As$ material system grown by molecular beam epitaxy

(MBE). Two strong peaks observed in the measured photocurrent-voltage characteristics correspond to the sequential resonant tunneling between the ground state in one well and the first two excited states in the adjacent well. In 1989, Helm et al. [6] reported the first observation of intersubband emission in the infrared from sequential resonant-tunneling in a semiconductor superlattice structure. In 1994, intersubband electroluminescence in the mid-infrared region ($\lambda \sim 5$ μm) at room temperature was reported by Faist et al. [7]. In their design, electrons were first injected via resonant tunneling from a doped graded gap alloy into a three-quantum-well active region. Light emission then occurred via electron relaxation between the upper (n=3) and the lower subband (n=2) in the active region. The population inversion between these two states is ensured due to the much longer nonradiative relaxation time between n=3 and n=2 subbands than that between the lower two states. By using a similar design, the first mid-infrared semiconductor laser based on intersubband transitions was demonstrated by Faist et al. in 1994 [1]. This intersubband laser was coined quantum cascade laser, since it operates based on resonant tunneling of electrons between quantum confined states and the cascaded scheme of electron transport in the laser structure.

The first QCLs emitting at $\lambda = 4.26$ μm were based on a diagonal-transition design, and the measured peak pulsed power was only $\sim$ 8mW from a single facet at T = 10 K. Since then, the performance of mid-infrared QCLs has been significantly enhanced due to improved designs of their active region and waveguide structure, as well as technological advances in the crystal growth and device fabrication. Based on a vertical-transition design, Faist et al. [8] reported 4.6 μm-emitting QCLs operating in continuous-wave (CW) mode above liquid-nitrogen temperature ($T \sim 85$ K) in 1995. The first room-

temperature operation of QCLs in pulsed mode was demonstrated in 1996 [9] by utilizing a low-doped, funnel-injector and the vertical-transition design in three-quantum-well active-region. A peak pulsed power of 200 mW was measured at the wavelength of $\lambda =$ 5.2 µm. In 1998, to improve the heat dissipation in the lateral direction, Beck et al. [10] reported the first buried-heterostructure (BH) QCLs by regrowing undoped InP around the laser core. These BH-QCL devices showed much lower thresholds and higher slope efficiency compared to lasers without the regrown InP. In 2002, Beck et al. [11] demonstrated the first CW operation of QCLs at room temperature based on the BH device geometry and epi-down chip-mounting. In recent years, high-performance mid-infrared QCLs emitting watt-level CW output power at room temperature have been reported by several research groups [12-14].

The emission wavelengths of QCLs cover a wide range of electromagnetic spectrum. To date, high performance QCLs have been demonstrated in the mid-infrared region (~ 3 -20 µm) using both InGaAs/AlInAs/InP [15] and GaAs/AlGaAs/GaAs [16] material systems. The emission wavelength of QCLs can be further extended to the terahertz (THz) region. THz QCLs are typically based on GaAs/AlGaAs/GaAs material system, and their detailed accounts can be found in the review paper published by Williams [17] in 2007. On the other hand, for short-wavelength (3- 4 µm) QCLs, besides InGaAs/AlInAs/InP other novel material systems are employed, such as InGaAs/AlAs(Sb)/InP [18] and InAs/AlSb/GaSb (or InAs/AlSb/InAs) [19], since large conduction-band discontinuity is required to prevent electrons in the upper lasing state from being thermally excited to the continuum.

Over the past years, QCLs have evolved from a laboratory proof-of concept to real-world devices. They have attracted a great deal of interests from both research and industrial communities for a wide range of applications. In particular, QCLs are ideal candidates for trace-gas sensing and environmental monitoring, since the fundamental rotational-vibrational frequencies of many molecules lie in the mid-infrared region. Narrow-linewidth, tunable mid-infrared QCLs are therefore suitable to detect and map out these molecules in this fingerprint region [20]. Other important applications for QCLs include spectroscopy, infrared countermeasure, medical diagnostics, and free-space communication.

1.2 Thesis Overview

This thesis focuses on developing high-performance mid-infrared quantum cascade lasers and arrays. In chapter 2, the fundamentals for mid-infrared quantum cascade lasers are provided. Based on a simplified three-level rate-equation analysis, the quantitative description of population inversion between the upper and lower lasing level, gain cross-section, threshold current density, as well as slope efficiency are derived. The electro-optical characteristics of mid-infrared quantum cascade lasers depend strongly on the heatsink temperature. To describe this temperature dependence, the definition of characteristic temperatures for both threshold current density and differential quantum efficiency are given. The intersubband scattering of electrons by longitudinal optical (LO) phonons is also introduced in this chapter.

In chapter 3, 4.8 μm-emitting, step-tapered active-region (STA) QCLs for complete suppression of carrier leakage are designed using eight-band k·p simulation [21]. The

design parameters for STA-QCLs based on both double-phonon-resonance (DPR) and single-phonon-resonance (SPR) depopulation, including their global "effective" upper-state lifetime, dipole matrix element, and the broadening of instersubband linewidth due to interface roughness scattering, are described. In the STA-QCLs, the large energy separation between the upper laser level and the next-higher energy state (E_{54} in STA-DPR or E_{43} in STA-SPR QCLs) leads to complete suppression of carrier leakage. A comparison between STA-QCLs and the state-of-the-art shallow-well TA-QCLs is also presented. In particular, by reducing the total number of interfaces, and the number of high-strained layers such as AlAs in the laser core, the thermal resistance of proposed STA-QCLs is much lower than that for shallow-well TA-QCLs, which therefore makes the STA-QCLs much more suitable for long-term, reliable operation at high ($\geq$ 0.5 W) CW powers.

In chapter 4, a novel fabrication method of buried-heterostructure mid-infrared quantum cascade lasers is described by using non-selective regrowth of iron-doped InP, around deeply-etched laser ridges, via metal-organic chemical vapor deposition (MOCVD) and planarization via chemical polishing [22]. The demonstrated fabrication method provides a more flexible route to realizing buried-heterostructure quantum cascade lasers by removing strict requirements on the etched-ridge sidewall profile, and on the physical dimensions of the dielectric mask for the regrowth via MOCVD. This method can be further employed for making large-emitting-aperture, closely-packed arrays of quantum cascade lasers, with planarized geometry, for coherent-power scaling.

In chapter 5, a novel fabrication process for the realization of on-chip, large-emitting-aperture, resonant-leaky-wave coupled QCL arrays is described [23]. This fabrication

method mainly involves a deep-trench formation step by hybrid dry and wet etch, followed by a regrowth step by MOCVD to form array element and interelement regions. A refined fabrication process [24] was also developed in order to produce QCL arrays with a planar geometry. This new process results in planar interelement regions, which allows for significantly improved control over the array geometry and the dimensions of element and interelement regions. Such a planar process is highly desirable to realize QCL arrays emitting at $\lambda = 4.5 - 5.0$ μm, where fabrication tolerances for single-mode operation are tighter compared to devices emitting at longer wavelengths in the mid-infrared.

Finally, in chapter 6, a nanopattering process for making sub-30 nm structures using diblock copolymer templates and Ni electrodeposition is described [25]. A large-area, high-density Ni nanopillar arrays are fabricated on GaAs substrates. The fabricated Ni nanopillar arrays, have an average diameter of 24 nm, a density of about $10^{11}/cm^2$, and are formed over an area of 1 cm ×1 cm. These results are among the largest, highly dense metal-nanopillar arrays with a feature size of sub-30 nm fabricated on III-V semiconductor substrates. These arrays could be used in other pattern-transfer processes, such as in the process for making quantum boxes in the active region of intersubband quantum box (IQB) lasers [26]. They could also serve as nanostructures in their own right. This process presented here provides a generalized method of forming such arrays of metal nanopillar.

Reference

[1] J. Faist, F. Capasso, D. Sivco, C. Sirtori, A. Hutchinson, and A. Cho. "Quantum cascade laser", *Science*, **264**, 553-556 (1994).

[2] F. Capasso. "Band-gap engineering: From physics and materials to new semiconductor devices", *Science*, **235**, 172-176 (1987).

[3] R. Kazarinov and R. Suris. "Possibility of the amplification of electromagnetic waves in a semiconductor with a superlattice", *Sov. Phys. Semicond.*, **1**, 120-131 (1971).

[4] L. C. West and S. J. Eglash. "First observation of an extremely large-dipole infrared transition within the conduction band of a GaAs quantum well", *Appl. Phys. Lett.*, **46**, 1156-1158 (1985).

[5] F. Capasso, K. Mohammed, and A. Y. Cho. "Sequential resonant tunneling through a multiquantum well superlattice", *Appl. Phys. Lett.*, **48**, 478-480 (1986).

[6] M. Helm, P. England, E. Colas, F. DeRosa, and S. J. Allen, Jr.. "Intersubband emission from semiconductor superlattices excited by sequential resonant tunneling", *Phys. Rev. Lett.*, **63**, 74-77 (1989).

[7] J. Faist, F. Capasso, C. Sirtori, D. Sivco, A. L. Hutchinson, S.-N. G. Chu, and A. Y. Cho. "Mid-infrared field-tunable electroluminescence at room temperature by photon-assisted tunneling in coupled-quantum wells", *Appl. Phys. Lett.*, **64**, 1144-1146 (1994).

[8] J. Faist, F. Capasso, C. Sirtori, D. L. Sivco, A. L. Hutchinson, and A. Y. Cho. "Continuous wave operation of a vertical transition quantum cascade laser above T= 80 K", *Appl. Phys. Lett.*, **67**, 3057-3059 (1995).

[9] J. Faist, F. Capasso, C. Sirtori, D. L. Sivco, J. N. Baillargeon, A. L. Hutchinson, S.-N. G. Chu, and A. Y. Cho. "High power mid-infrared ($\lambda \sim 5$ μm) quantum cascade lasers operating above room temperature", *Appl. Phys. Lett.*, **68**, 3680-3682 (1996).

[10] M. Beck, J. Faist, C. F. Gmachl, F. Capasso, D. L. Sivco, J. N. Baillargeon, and A. Y. Cho. "Buried heterostructure quantum cascade lasers", *Proc. SPIE*, **3284**, 231-236 (1998).

[11] M. Beck, D. Hofstetter, T. Aellen, J. Faist, U. Oesterle, M. Ilegems, E. Gini, and H. Melchior. "Continuous wave operation of a mid-infrared semiconductor laser at room temperature", *Science*, **295**, 301-305 (2002).

[12] A. Lyakh, C. Pflügl, L. Diehl, Q. J. Wang, F. Capasso, X. J. Wang, J. Y. Fan, T. Tanbun-Ek, R. Maulini, A. Tsekoun, R. Go, and C. Kumar N. Patel. "1.6 W high wall plug efficiency, continuous-wave room temperature quantum cascade laser emitting at 4.6 μm", *Appl. Phys. Lett.*, **92**, 111110 (2008).

[13] A. Lyakh, R. Maulini, A. Tsekoun, R. Go, C. Pflügl, L. Diehl, Q. J. Wang, F. Capasso, and C. Kumar N. Patel. " 3 W continuous-wave room temperature single-facet emission from quantum cascade lasers based on nonresonant extraction design approach", *Appl. Phys. Lett.*, **95**, 141113 (2009).

[14] Y. Bai, N. Bandyopadhyay, S. Tsao, S. Slivken, and M. Razeghi. "Room temperature quantum cascade lasers with 27% wall plug efficiency", *Appl. Phys. Lett.*, **98**, 181102 (2011).

[15] M. Razeghi. "High-performance InP-based mid-IR quantum cascade lasers", *IEEE J. Sel. Top. Quantum Electron.* **15(3)**, 941-951 (2009).

[16] H. Page, S. Dhillon, M. Calligaro, C. Becker, V. Ortiz, and C. Sirtori. "Improved CW operation of GaAs-based QC lasers: T_{max} = 150 K", *IEEE J. Quantum Electron.* **40**, 665-672 (2004).

[17] B. S. Williams. "Terahertz quantum-cascade lasers", *Nat. Photon.*, **1**, 517-525 (2007).

[18] J. P. Commin, D. G. Revin, S. Y. Zhang, A. B. Krysa, K. Kennedy, and J. W. Cockburn. "High peak power $\lambda \sim 3.3$ and 3.5 μm InGaAs/AlAs(Sb) quantum cascade lasers operating up to 400 K", *Appl. Phys. Lett.*, **97**, 031108 (2010).

[19] A. N. Baranov and R. Teissier. "Quantum cascade lasers in the InAs/AlSb material system", *IEEE J. Sel. Top. Quantum Electron.* **99**, 1-12 (2015).

[20] R. F. Curl, F. Capasso, C. Gmachl, A. A. Kosterev, B. McManus, R. Lewicki, M. Pusharsky, G. Wysocki, and F. K. Tittel. "Quantum cascade lasers in chemical physics", *Chem. Phys. Letters,* **487**, 1-18 (2010).

[21] D. Botez, J. C. Shin, J. D. Kirch, C.-C. Chang, L. J. Mawst, and T. Earles. "Multidimensional conduction-band engineering for maximizing the continuous-wave (CW) wallplug efficiencies of mid-infrared quantum cascade lasers", *IEEE J. Sel. Top. Quantum Electron.* **19(4)**, 1200312 (2013).

[22] C.-C. Chang, J. D. Kirch, P. Buelow, C. Boyle, T. F. Kuech, D. Lindberg III, T. Earles, D. Botez, and L. J. Mawst. "Buried-heterostructure mid-infrared quantum cascade lasers fabricated by non-selective regrowth and chemical polishing", *Electron. Lett.*, accepted (2015).

[23] J. D. Kirch, C.-C. Chang, C. Boyle, L. J. Mawst, D. Lindberg III, T. Earles, and D. Botez. "5.5 W near-diffraction-limited power from resonant leaky-wave coupled phase-locked arrays of quantum cascade lasers", *Appl*. *Phys*. *Lett*., **106**, 061113 (2015).

[24] C.-C. Chang, J. D. Kirch, C. Boyle, C. Sigler, L. J. Mawst, D. Botez, B. Zutter, P. Buelow, K. Schulte, T. F. Kuech, and T. Earles. "Planarized process for resonant leaky-wave coupled phase-locked arrays of mid-IR quantum cascade lasers", *Proc*. *SPIE*, **9382**, 938213 (2015).

[25] C.-C. Chang, D. Botez, L. Wan, P. F. Nealey, S. Ruder, and T. F. Kuech. "Fabrication of large-area, high-density Ni nanopillar arrays on GaAs substrates using diblock copolymer lithography and electrodeposition", *J*. *Vac*. *Sci*. *Technol*. *B*, **31(3)**, 031801 (2013).

[26] C.-F. Hsu, O Jeong-Seok, P. Zory, and D. Botez. "Intersubband quantum-box semiconductor lasers", *IEEE J*. *Sel*. *Top*. *Quantum Electron*. **6(3)**, 491-503 (2000).

CHAPTER TWO

BACKGROUND FOR MID-INFRARED QUANTUM CASCADE LASERS

2.1 Introduction

Quantum cascade lasers (QCLs) are unipolar semiconductor lasers based on transitions between subbands resulting from quantum confinement in multi-quantum-well structures. The first mid-infrared (mid-IR) QCLs were first demonstrated by Faist et al. [1] in 1994 in Bell Labs. The corresponding conduction-band diagram and the schematic representation of in-plane energy-momentum dispersion for subband 1, 2, and 3 are shown in Fig. 2.1. The laser core is composed of twenty-five repetitive stages, and each stage contains a three-quantum-well active region and a digitally graded electron injection/relaxation region. In the active region, subband 3 is the upper laser level, and subband 2 is the lower laser level. Upon applying an electric field, electrons are injected from the injector region into the upper laser level via resonant tunneling through the injection barrier. Photons are then emitted as a result of the electronic transitions between upper and lower laser level. It is clear that in contrast to the conventional semiconductor diode lasers where emission wavelength is determined by the energy gap of the active-region material, the lasing wavelength of QCLs can be tailored at will by simply changing the layer thicknesses of quantum wells and barriers in the active region. Once electrons reach the lower laser level, they are rapidly scattered into the lower lying subband (subband 1) due to inelastic LO phonon scattering, and then extracted into the injector region of next stage. Therefore, due to this cascaded scheme, one electron can

emit multiple photons (twenty-five photons in this case) as it tumbles down the energy staircase in the laser core. The electron lifetimes in these subbands are very short, typically on the order of picosecond due to the LO phonon scattering. The population inversion between upper and lower laser level in mid-IR QCLs thus needs to be carefully engineered.
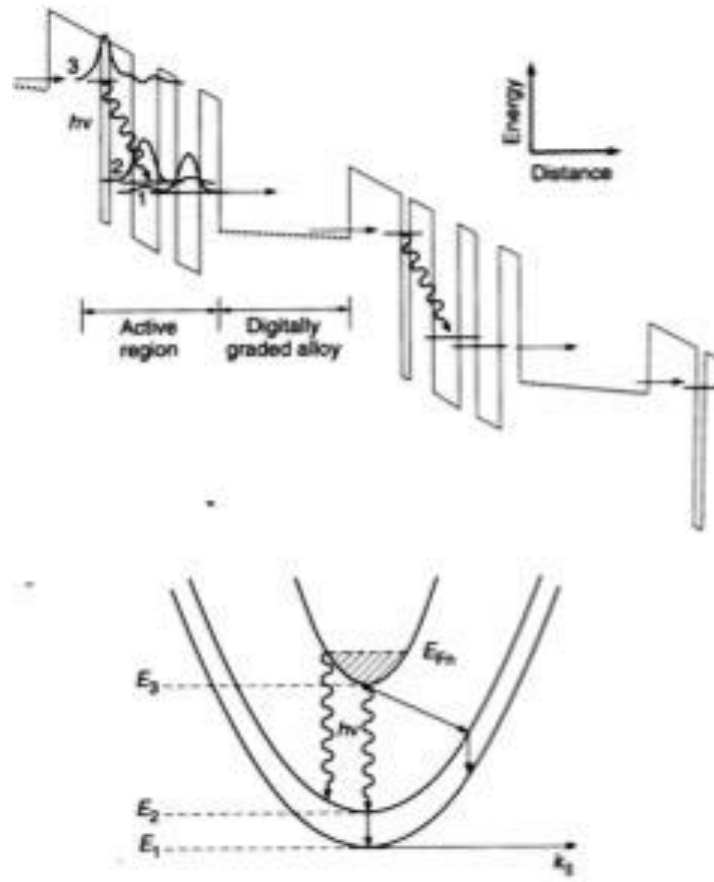
Fig. 2.1. Conduction-band diagram for the first demonstrated QCLs and the schematic representation of in-plane energy-momentum dispersion for subband 1, 2, and 3.

In the mid-IR QCLs based on three-quantum-well active-region designs, the population inversion between upper and lower laser level is established by placing an additional subband (subband 1 in Fig. 2.1) about an LO phonon energy (34 meV in InGaAs) below the lower laser level. Since the electron lifetime due to the inelastic LO phonon scattering increases with the in-plane momentum exchange between initial and final subbands in the scattering process, for the mid-IR QCLs (photon energy = $h\nu \gg$ 34 meV) the electron lifetime in the upper laser level ($\sim$ a few picoseconds) is much longer than that ($\sim$ sub-picosecond) in the lower laser level, and the population inversion between them can therefore be achieved. In this case, since only one additional subband is utilized to depopulate the lower laser level, the carrier depopulation scheme is typically referred to as single-phonon-resonance (SPR) depopulation. On the other hand, in the QCLs based on four-quantum-well active regions, the carrier extraction is facilitated by a ladder of three subbands, and the energy separation between each of these subbands is about an LO phonon energy. This carrier depopulation scheme is then referred to as the double-phonon-resonance (DPR) depopulation scheme [2]. The schematic representations of conduction-band diagrams for both SPR and DPR carrier-depopulation schemes are shown in Fig. 2.2.

In the SPR depopulation scheme, upon the lasing transition carriers are rapidly depopulated from the lower laser level (level 2) to level 1 via LO phonon scattering. From level 1, carriers are then extracted into the injector of next stage via resonant tunneling through the exit barrier. This tunneling process, however, proceeds typically on a timescale much longer than the lifetime for carriers scattered from level 2 to level 1 due to LO phonon scattering. As a result, carriers are accumulated in level 1 and can easily be

scattered back to level 2 by absorbing an LO phonon energy. This carrier extraction bottleneck reduces the population inversion between upper and lower laser level, and hence increases the lasing threshold and degrades the high-temperature performance. On the contrary, in the DPR depopulation scheme, since the energy difference between the lower laser level (level 3) and the lowest active region level (level 1), E_{31}, is increased by a factor of two compared to that (E_{21}) in the SPR depopulation scheme, carrier thermal backfilling from the lowest active region level into the lower laser level is suppressed. Moreover, due to the addition of an extra level, the carrier lifetime in the lower laser level τ_3 ($1/\tau_3 = 1/\tau_{32} + 1/\tau_{31}$) in the DPR scheme is further decreased compared to that ($\tau2$; $1/\tau_2 = 1/\tau_{21}$) in the SPR scheme. Clearly, compared to the SPR scheme, the DPR depopulation scheme not only enables more efficient carrier extraction to the injector region, but a high population inversion between the upper and lower laser levels is also maintained.

It is worth noting that, besides conventional SPR and DPR designs, other carrier depopulation schemes have also been employed in the QCL active-region design. In the 4.9 μm-emitting QCLs reported by Bai et al. [3], its laser core is based on a three-quantum-well active-region design. However, the carrier depopulation in this structure is not a typical SPR scheme where carriers are first depopulated from the lower laser level (level 2) to a lower level (level 1) and then extracted from that level. Rather, due to the strong coupling between both of these levels and the penetrating states from the injector region, there is resonant extraction from both level 2 and level 1. This carrier extraction scheme is similar to the so-called bound-to-continuum (BC) active-region design [4] where carriers are extracted from a miniband upon the lasing transition. This miniband-type extraction scheme was also employed in the 4.3 μm-emitting QCLs reported by Yu

et al. [5], in which carriers are resonantly extracted from all the lower levels (level 3, 2, and 1) in the four-quantum-well active-region. More recently, the miniband-type extraction was employed in 8.7-8.8 μm-emitting QCLs and high T_0 and T_1 values were obtained [11].

In the QCL designs, the moderately doped injector/relaxation regions mainly serve as electron reservoirs providing electrons to be injected into the gain region, and also enable electrons to regain their energy by the acceleration of the applied electric field before re-injected to the next stage. The doping in the injector/extractor regions is absolutely necessary in order to prevent the formation of electrical domains due to the build-up of space charges after electron injection found in the undoped superlattices. In addition, the layer thicknesses of quantum wells and barriers in the injector/extractor regions have to be properly designed based on the Bragg reflection condition, so that a minigap can be formed facing the upper lasing level to prevent electrons in the upper laser level from escaping into the continuum.
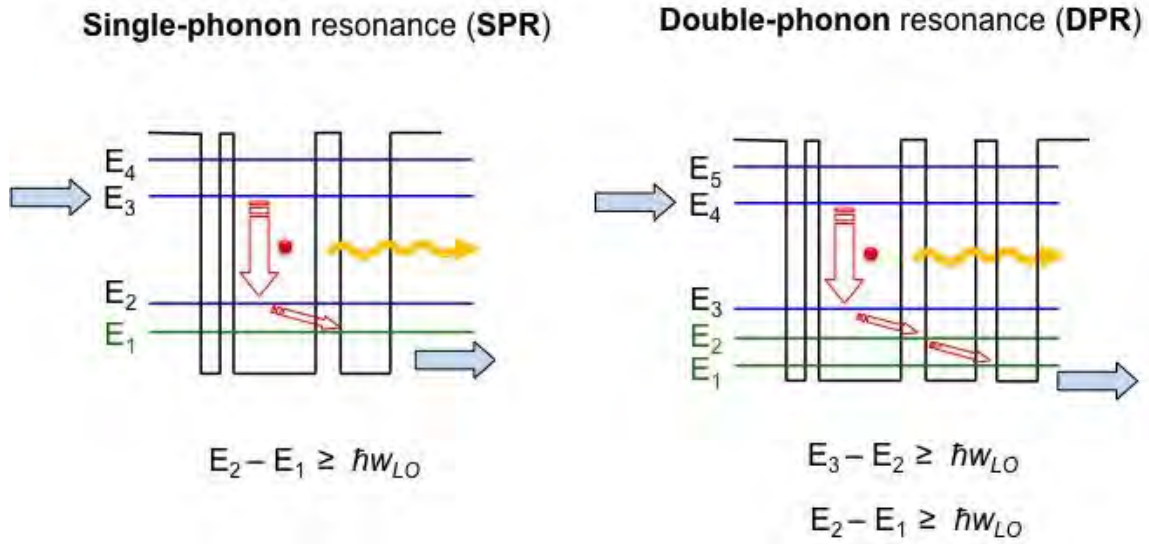
Fig. 2.2. Schematic representations of conduction-band diagrams for mid-IR QCLs based on single-phonon-resonance (SPR) depopulation scheme (left), and double-phonon-resonance (DPR) depopulation scheme (right).

2.2 Rate Equation

In this section, by analyzing the rate equations based on a simplified three-level model, the population inversion, gain coefficient, the threshold current density, as well as the slope efficiency of mid-IR QCLs are derived without taking into account carrier leakage [6].
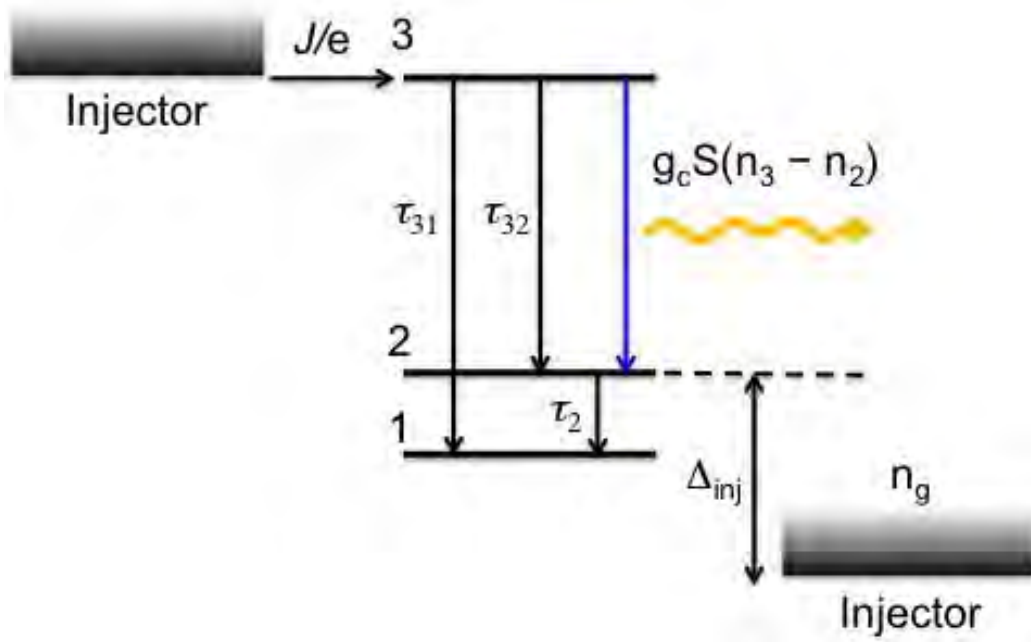
Fig. 2.3. Schematic representations of a simplified three-level model used in the rate equation analysis to describe the characteristics of mid-IR QCLs.

Fig. 2.3 shows the schematic representation of a simplified three-level model for describing mid-IR QCLs based on three-quantum-well active-region designs. The sheet carrier density of the injectors is assumed to be a constant n_g determined by the injector doping level. The electrons are injected from the injector of the previous stage into upper laser level (level 3) (100 % tunneling-injection efficiency is assumed) in the gain region at a rate of J/e, where J is the current density and e is the electronic charge. The lasing transition then occurs between level 3 and level 2. From level 3, electrons can also relax nonradiatively via inelastic LO phonon scattering to level 2 and level 1, and the corresponding electron lifetimes due to LO phonon scattering are denoted as τ_{32} and τ_{31}, respectively. The electron lifetime in level 3 thus can be estimated by the relation $1/\tau_3 =$

$1/\tau_{32} + 1/\tau_{31}$. Electrons in the lower laser level (level 2) are rapidly scattered to level 1 at a scattering rate of $1/\tau_2$ ($\tau_2 = \tau_{21}$), and then extracted into the injector of the next stage. Besides, due to thermal excitation, electrons in the ground state in the injector of the next state can backfill the lower lasing level via the absorption of LO phonons. The amount of carriers that thermally backfill the lower lasing level can be approximated by $n_2^{thermal} \sim n_g \exp(-\Delta_{inj}/k_B T_e)$, where Δ_{inj} is the energy difference between the lower laser level and the ground state in the injector of next stage, k_B is Boltzmann constant, and T_e is the electronic temperature.

The rate of change of the sheet carrier density of each level can be written as follows:

$$\frac{dn_3}{dt} = \frac{J}{e} - \frac{n_3}{\tau_3} - Sg_c(n_3 - n_2) \tag{2.1}$$

$$\frac{dn_2}{dt} = \frac{n_3}{\tau_{32}} + Sg_c(n_3 - n_2) - \frac{n_2}{\tau_2} + \frac{n_2^{thermal}}{\tau_2} \tag{2.2}$$

$$\frac{dS}{dt} = \frac{c}{n_{eff}}\left[(g_c(n_3 - n_2) - \alpha_{total})S + \beta\frac{n_3}{\tau_{sp}}\right] \tag{2.3}$$

where S is the photon flux density (in the unit of 1/sec·cm²), g_c is the gain cross-section, n_{eff} is the effective refractive index of the optical mode, α_{total} is the total loss, β is the spontaneous emission factor, and τ_{sp} is the electron lifetime due to spontaneous emission from level 3. From the two-dimensional absorption coefficient α_{2D} derived based on Fermi's Golden rule, and using a Lorentzian lineshape function, the gain cross-section g_c can be written as follows:

$$g_c = \Gamma\frac{4\pi e^2}{\epsilon_0 n_{eff}\lambda}\frac{z_{32}^2}{2\gamma_{32}L_p} \tag{2.4}$$

where Γ is the transverse optical-mode confinement factor, ϵ_0 is the electric permittivity in vacuum, z_{32} is the dipole matrix element between level 3 and level 2, λ is the emission wavelength, L_p is the length of one stage, and $2\gamma_{32}$ is the full width at half maximum (FWHM) of the transition.

Below the lasing threshold, the photon flux in the laser cavity is negligible, so S in the above rate equations can be set to be zero. Also, by setting the time derivative to be zero at steady state, the carrier density in the upper lasing level n_3 can be derived from eq. (2.1):

$$n_3 = \frac{J\tau_3}{e} \tag{2.5}$$

Similarly, the population in the lower lasing level n_2 can also be written as follows:

$$
\begin{aligned}
n_2 &= \tau_2 \left(\frac{n_3}{\tau_{32}} + \frac{n_2^{thermal}}{\tau_2} \right) \\
&= \tau_2 \left[\frac{1}{\tau_{32}} \left(\frac{J\tau_3}{e} \right) + \frac{n_2^{thermal}}{\tau_2} \right]
\end{aligned} \tag{2.6}
$$

From eq. (2.5) and (2.6), the population inversion between level 3 and level 2, $\Delta n = n_3 - n_2$, can therefore be written as follows:

$$
\begin{aligned}
\Delta n &= \frac{J\tau_3}{e} - \tau_2 \left[\frac{1}{\tau_{32}} \left(\frac{J\tau_3}{e} \right) + \frac{n_2^{thermal}}{\tau_2} \right] \\
&= \frac{J\tau_3}{e} \left(1 - \frac{\tau_2}{\tau_{32}} \right) - n_2^{thermal} \\
&= \frac{J}{e} \tau_{eff} - n_2^{thermal}
\end{aligned} \tag{2.7}
$$

where $\tau_{eff} = \tau_3(1 - \frac{\tau_2}{\tau_{32}})$ is the "effective" upper-state lifetime. It is clear that in order to ensure a large population, τ_2 has to be much smaller than τ_{32}.

At the lasing threshold, the modal gain $g_c\Delta n$ compensates for the total loss α_{total}:

$$g_c\Delta n = g_c\left(\frac{J_{th}}{e}\,\tau_{eff} - n_2^{thermal}\right) = \alpha_{total} \tag{2.8}$$

Therefore, the threshold current density J_{th} can be written as follows:

$$J_{th} = e\,\frac{\alpha_{total}/g_c + n_2^{thermal}}{\tau_{eff}}$$

$$= \frac{1}{\tau_{eff}}\left[\frac{\epsilon_0 n_{eff} L_p \lambda (2\gamma_{32})}{4\pi\Gamma z_{32}^2}\alpha_{total} + e n_2^{thermal}\right] \tag{2.9}$$

In writing above equations, it was assumed that there is no electron escape from the upper laser level, after electrons are injected from the injector. However, in typical QCL devices, especially for the short-wavelength mid-IR QCLs, the electrons in the upper laser level can be further excited to higher energy states in the active region and eventually lead to leakage currents [7]. Specifically, for $4.5 - 5.0$ μm-emitting QCLs of DPR depopulation scheme, after injection, some of the electrons in the upper laser level can be thermally excited to next higher energy level, level 5 (Fig. 2.4). From there, some of the electrons relax to lower active-region levels (level 3, 2, and 1), and some are further excited to level 6. From level 6, most of the electrons relax to lower active-region levels with a negligible part excited even further to the continuum [7, 8]. Thus, carrier leakage for these QCLs mainly consists of thermal excitation of injected carriers from upper laser level, level 4 to level 5 and 6, followed by relaxation to lower active-region

levels and thus constitutes shunt current within the active region. The primary leakage paths for these QCLs are illustrated in Fig. 2.4.
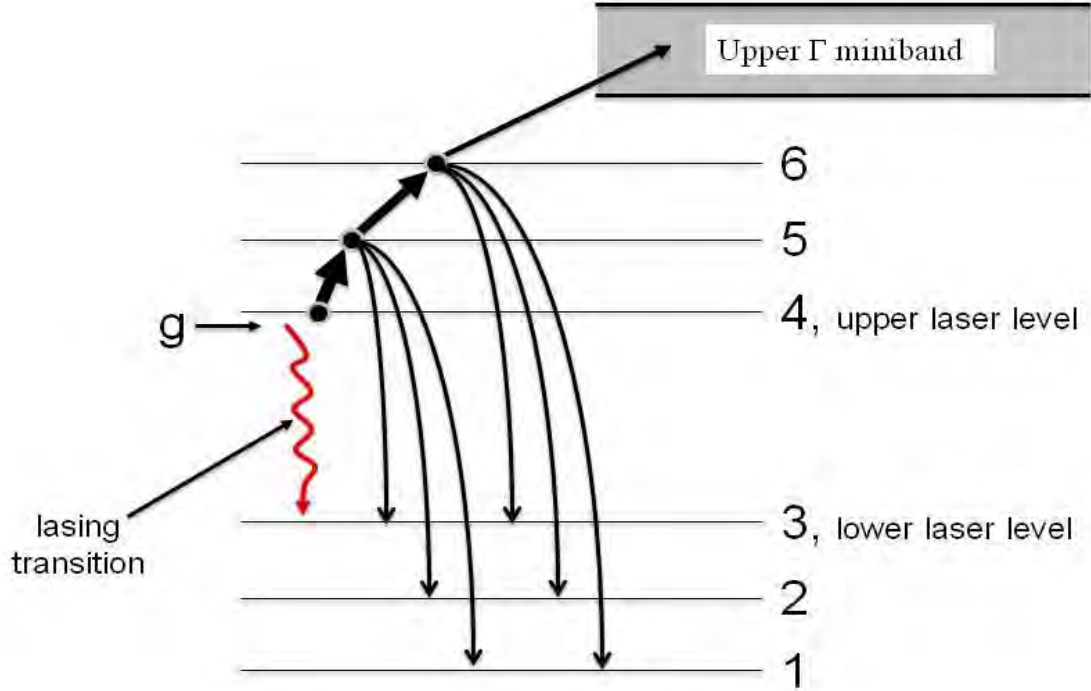
Fig. 2.4. Schematic representations of primary carrier-leakage paths for $4.5 - 5.0$ μm-emitting QCLs of DPR depopulation scheme.

The leakage-current density at threshold for a four-quantum-well active-region QCLs can therefore be written as follows [7,9]:

$$J_{leak,th} = \frac{e}{\tau_{5,leak}} n_5 + \frac{e}{\tau_{6,leak}} n_6 \qquad (2.10)$$

where n_5 and n_6 are sheet carrier densities in level 5 and 6, $\tau_{5,leak}$ and $\tau_{6,leak}$ are electron-leakage lifetimes corresponding to level 5 and 6, respectively. More specifically, $\tau_{5,leak}$,$\tau_{6,leak}$, n_5, and n_6 can be given as follows:

$$\tau_{5,leak} = (1/\tau_{53} + 1/\tau_{52} + 1/\tau_{51})^{-1} \tag{2.11}$$

$$\tau_{6,leak} = (1/\tau_{63} + 1/\tau_{62} + 1/\tau_{61} + 1/\tau_{6um})^{-1} \tag{2.12}$$

$$n_5 = n_4 \frac{\tau_{5,total}}{\tau_{45}} + n_6 \frac{\tau_{5,total}}{\tau_{65}} \tag{2.13}$$

$$n_6 = n_5 \frac{\tau_{6,total}}{\tau_{65}} \tag{2.14}$$

where τ_{6um} is the lifetime corresponding to thermal excitation from level 6 to all the levels in the upper Γ miniband, $\tau_{5,total}$ and $\tau_{6,total}$ are the net carrier lifetimes in level 5 and 6:

$$\tau_{5,total} = (1/\tau_{56} + 1/\tau_{54} + 1/\tau_{53} + 1/\tau_{52} + 1/\tau_{51})^{-1} \tag{2.15}$$

$$\tau_{6,total} = (1/\tau_{65} + 1/\tau_{64} + 1/\tau_{63} + 1/\tau_{62} + 1/\tau_{61} + 1/\tau_{6um})^{-1} \tag{2.16}$$

It has been shown [8] that for $E_{54} \geq 50$ meV, the primary leakage path is through level 5. By using eq. (2.13) and ignoring the leakage through level 6, the leakage current density at threshold in eq. (2.9) can be rewritten as follows:

$$J_{leak,th} = \frac{e}{\tau_{5,leak}} n_5 = \frac{en_4 \tau_{5,total}}{\tau_{45} \tau_{5,leak}} \tag{2.17}$$

Therefore, a pumping efficiency term [11] η_p can be given as follows:

$$\eta_p = 1 - \frac{J_{leak,th}}{J_{th}}$$

$$= 1 - \frac{J_{leak,th}}{J_4 + J_{leak,th}}$$

$$= \frac{1}{1 + \frac{J_{leak,th}}{J_4}}$$

$$= \frac{1}{1 + \frac{\left(\frac{en_4\tau_{5,total}}{\tau_{45}\tau_{5,leak}}\right)}{\left(\frac{en_4}{\tau_{4g}}\right)}}$$

$$= \frac{1}{1 + \frac{\tau_{4g}}{\tau_{45}}\frac{\tau_{5,total}}{\tau_{5,leak}}} \tag{2.18}$$

Where τ_{4g} is global lifetime in level 4. From eq. (2.18), it is apparent that the key to keep η_p high is to increase τ_{45}, the scattering time from the upper laser level, level 4 to level 5, which can be approximated as follows:

$$\frac{1}{\tau_{45}} \sim \frac{1}{\tau_{54}}\exp\left(\frac{-E_{54}}{kT_{e4}}\right) \tag{2.19}$$

where k is Boltzmann constant, T_{e4} is the electronic temperature in level 4. Clearly, in order to suppress carrier leakage for 4.5 – 5.0 μm-emitting QCLs, it is imperative to increase both E_{54} and τ_{54} as large as possible, and, if possible, minimize T_{e4}.

By taking into account both backfilling and carrier leakage, the threshold current density J_{th} can be written as follows:

$$J_{th} = J_{0,th} + J_{bf,th} + J_{leak,th} \tag{2.20}$$

where $J_{0,th}$ is the threshold current density in the absence of electron backfilling and carrier leakage, $J_{bf,th}$ and $J_{leak,th}$ are the current densities required to compensate for the backfilling and carrier leakage, respectively. $J_{0,th}$ is defined as follows:

$$J_{0,th} = \frac{e\alpha_{total}}{\tau_{up,g}g_c} \tag{2.21}$$

Eq. (2.20) can be rewritten if the effect of carrier leakage on the threshold current density is through the pumping efficiency term η_p:

$$J_{th} = \frac{J_{0,th} + J_{bf,th}}{\eta_p} \tag{2.22}$$

where $J_{bf,th}$ is the current density required at threshold to compensate for backfilling:

$$J_{bf,th} \approx \frac{en_s}{\tau_{up,g}} \exp\left(\frac{-\Delta_{inj}}{kT_{eg}}\right) \tag{2.23}$$

where $\tau_{up,g}$ is the effective global upper-state lifetime, and T_{eg} is the electronic temperature in the injector miniband. By using eq. (2.21) and eq. (2.23), eq. (2.22) can be written as follows:

$$J_{th} = \left(\frac{1}{\eta_p}\right)\left(\frac{e}{\tau_{up,g}}\right)[\left(\frac{\alpha_m + \alpha_w}{g_c}\right) + n_s \exp\left(\frac{-\Delta_{inj}}{kT_{eg}}\right)]$$

$$= \left(\frac{e}{\tau_{up,g}'}\right)\left[\left(\frac{\alpha_m + \alpha_w}{g_c}\right) + n_s \exp\left(\frac{-\Delta_{inj}}{kT_{eg}}\right)\right] \tag{2.24}$$

where α_m is the mirror loss, α_w is actual waveguide loss, and $\tau_{up,g}'$ is the modified global effective upper-state lifetime, and is defined as follows:

$$\tau_{up,g}' = (\eta_p)\tau_{up,g} \tag{2.25}$$

By comparing eq. (2.24) with eq. (2.9), it is clear that carrier leakage can be taken into account in the threshold-current density equation by simply replacing $\tau_{up,g}$ with $\tau_{up,g}'$. The difference is significant, especially for conventional QCLs in which case carrier leakage increases [8] the J_{th} value by ~ 18 % at 300 K and ~ 30 % at 360 K.

The external differential quantum efficiency η_d for a QCL having N_p periods can be written as follows [8,10,11]:

$$\eta_d = \eta_p \eta_{tr} (\frac{\alpha_m}{\alpha_m + \alpha_w}) N_p$$

$$= \eta_i^d \left(\frac{\alpha_m}{\alpha_m + \alpha_w}\right) N_p \qquad (2.26)$$

where η_{tr} is the laser-transition differential efficiency, η_p is the differential pumping efficiency and is given by:

$$\eta_p = 1 - \frac{J_{leak,th}}{J_{th}} \qquad (2.27)$$

The product of η_p and η_{tr} can be thought of as the internal differential efficiency η_i^d. Finally, the slope efficiency dP/dI (W/A) is obtained by sing eq. (2.26):

$$\frac{dP}{dI} = \eta_d \left(\frac{h\nu}{e}\right) = \eta_p \eta_{tr} \left(\frac{\alpha_m}{\alpha_m + \alpha_w}\right) N_p \left(\frac{h\nu}{e}\right) \qquad (2.28)$$

where h is Planck's constant, and ν is frequency of the laser emission.

2.3 Temperature Dependence

As the heatsink temperature increases, the threshold-current density J_{th} increases, while the external differential quantum efficiency η_d decreases. The temperature dependence of J_{th} and η_d is described by following expressions:

$$J_{th}(T_{ref} + \Delta T) = J_{th}(T_{ref}) \exp\left(\frac{\Delta T}{T_0}\right) \qquad (2.29)$$

$$\eta_d(T_{ref} + \Delta T) = \eta_d(T_{ref}) \exp\left(\frac{-\Delta T}{T_1}\right) \qquad (2.30)$$

where $T_{ref} + \Delta T$ is the heatsink temperature and T_{ref} is the reference temperature, and T_0 and T_1 [12] are characteristic temperatures for threshold current density and external differential quantum efficiency, respectively.

From eq. (2.20), it is clear that the temperature dependence of J_{th} is through both carrier leakage $J_{leak,th}$ and backfilling $J_{bf,th}$ terms. Since backfilling (eq. (2.23)) is an exponential function of temperature, J_{th} is strongly affected by backfilling as the heatsink temperature increases. As a result, the T_0 value is also a strong function of temperature due to both carrier leakage and backfilling. It has been shown [8] that, by including both carrier leakage and backfilling terms in the threshold-current density equation, T_0 values can be successfully predicted theoretically for both 4.6 μm-emitting conventional QCLs and conduction-band-engineered 4.6- 4.8 μm-emitting QCL structures. On the contrary, by only taking into account carrier leakage, the calculated T_1 values are significantly higher than the experimental results for both 4.6 μm-emitting conventional and 4.8 μm-emitting deep-well (DW) QCLs. This discrepancy can be explained by first rewriting eq. (2.26):

$$\eta_d(T) = \eta_p(T)\eta_{trans}\left(\frac{\alpha_m}{\alpha_m + \alpha_w(T)}\right) N_p$$

$$= \left(1 - \frac{J_{leak,th}}{J_{th}}(T)\right) \eta_{trans}\left(\frac{\alpha_m}{\alpha_m + \alpha_w(T)}\right) N_p \qquad (2.31)$$

As can be seen in eq. (2.31), η_d is a function of temperature not only due to the carrier-leakage current $J_{leak,th}$, but also due to the waveguide loss α_w. The waveguide loss results from both free carrier absorption loss and intersubband (ISB) absorption loss,

α_{ISB}. Moreover, it has been reported [13] that for 4.6- 4.8 μm-emitting QCLs, the waveguide loss is primarily (~ 90%) attributed to ISB absorption. Thus, as α_{ISB} increases with temperature, α_w also increases with temperature. Although there are no experimental data as far as the temperature dependence of α_w for 4.5-5.0 μm-emitting QCLs, such data have been published in Wittmann's dissertation [14] for 8.4 μm-emitting QCLs. By extracting α_w values from [14] at various temperatures, it has been shown in [9] that the increase of α_w with temperature is indeed due primarily to the increased ISB absorption loss with increasing temperature, for both QCLs of DPR and BC depopulation schemes.

As mentioned earlier, since backfilling depends exponentially on the temperature, the threshold current density, and in turn, the T_0 values, are strongly affected by backfilling. Consequently, as the heatsink temperature increases, both T_0 and T_1 values decrease. However, the T_1 value is a much better indicator of carrier leakage than the T_0 value [8,9].

2.4 Longitudinal Optical (LO) Phonon scattering

Electrons in an initial subband can be scattered into a final subband through various intersubband scattering processes, such as electron-electron interaction, ionized-impurity scattering, interface-roughness scattering, alloy scattering, acoustic-phonon scattering, and longitudinal optical (LO) phonon scattering. Among these scattering mechanisms, inelastic LO phonon scattering is the dominant carrier scattering mechanism for mid-IR QCLs. In polar semiconductors, LO phonon involves uniform displacements of charged atoms within the primitive unit cells. LO phonon scattering results from the interaction between electrons and the macroscopic polarization field due to the relative displacement of charged atoms. This electron-longitudinal-optical-phonon interaction is known as Fröhlich interaction. Due to this interaction, an electron in an initial subband can be scattered into a final subband by emitting or absorbing an LO phonon. As can be seen in Fig. 2.4, by following the approach developed by Price et al. [15], the transition rate for electrons of wavevector k in an initial subband |m> scattered to a final subband |n> can be given by:

$$w_{LO} = \frac{m^* e^2 \omega_{LO}}{2\hbar^2 \epsilon_P} \int d\theta \left(\frac{I^{mn}(Q)}{Q} \right) \tag{2.17}$$

$$I^{mn}(Q) = \int dz \int dz' \, \chi_m(z)\chi_n(z)e^{-Q|z-z'|}\chi_m(z')\chi_n(z') \tag{2.18}$$

where m^* is the effective mass, ω_{LO} is the LO phonon angular frequency, $\epsilon_P^{-1} = \epsilon_\infty^{-1} - \epsilon_s^{-1}$, Q is the in-plane momentum exchange, and χ_m and χ_n are wavefunctions for initial and final state. From eq. (2.17), it is clear that the LO phonon scattering rate is inversely proportional to the in-plane momentum exchange Q. The magnitude of Q can be evaluated by:

$$Q = (k^2 + k'^2 - 2kk'cos\theta)^{1/2} \qquad (2.19)$$

where θ is the scattering angle between initial and final wavevectors of the electron k and k'.
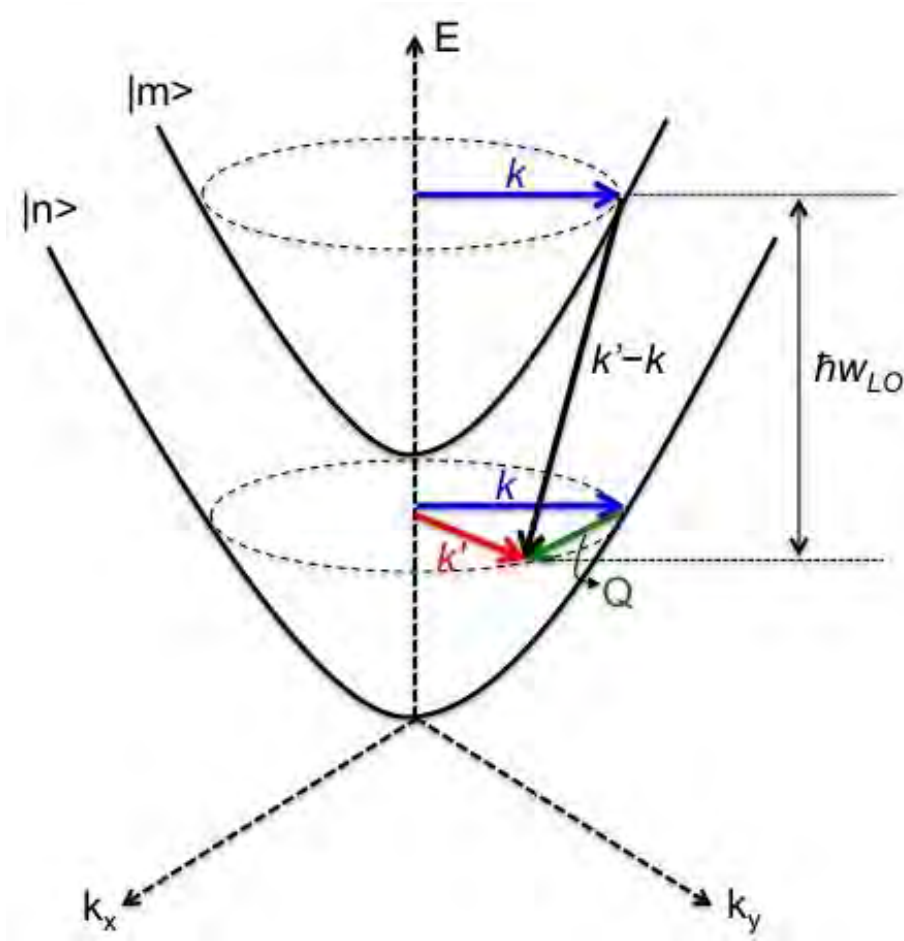
Fig. 2.5. Schematic representations of an electron of wavevector k in the initial subband |m> scattered into lower lying subband |n> by emitting an LO phonon of energy $\hbar\omega_{LO}$. The wavevector of electron in the final subband is k', and Q is the in-plane momentum exchange.

Reference

[1] J. Faist, F. Capasso, D. Sivco, C. Sirtori, A. Hutchinson, and A. Cho. "Quantum cascade laser", *Science*, **264**, 553-556 (1994).

[2] D. Hofstetter, M. Beck, T. Aellen, and J. Faist. "High-temperature operation of distributed feedback quantum-cascade lasers at 5.3 μm", *Appl. Phys. Lett.*, **78**, 396 (2001).

[3] Y. Bai, N. Bandyopadhyay, S. Tsao, E. Selcuk, S. Slivken, and M. Razeghi. "Highly temperature insensitive quantum cascade lasers", *Appl. Phys. Lett.*, **97**, 251104 (2010).

[4] J. Faist, M. Beck, T. Aellen, and E. Gini. "Quantum-cascade lasers based on a bound-to-continuum transition", *Appl. Phys. Lett.*, **78**, 147 (2001).

[5] J. S. Yu, A. Evans, S. Slivken, S. R. Darvish, and M. Razeghi. "Short wavelength ($\lambda \sim 4.3$ μm) high-performance continuous-wave quantum-cascade lasers", *IEEE Photon. Technol. Lett.*, **17**, 1154-1156 (2005).

[6] J. Faist. "*Quantun Cascade Lasers*", Oxford University Press (2013).

[7] D. Botez, J. C. Shin, S. Kumar, L. J. Mawst, I. Vurgaftman, and J. R. Meyer. "Electron leakage and its suppression via deep-well structures in 4.5-to-5.0-μm-emitting quantum cascade lasers", *Opt. Eng.*, **49**, 111108 (2010).

[8] D. Botez, S. Kumar, J.-C. Shin, L. J. Mawst, I. Vurgaftman, and J. R. Meyer. "Temperature dependence of the key electro-optical characteristics for midinfrared emitting quantum cascade lasers", *Appl. Phys. Lett.*, **97**, 071101 (2010).

[9] D. Botez, C.-C. Chang, and L. J. Mawst. "Temperature sensitivity of the electro-optical characteristics for mid-infrared ($\lambda = 3- 16$ μm) –emitting quantum cascade lasers", *J. Phys. D: Appl. Phys.*, submitted (2015).

[10] D. Botez, J. C. Shin, J. D. Kirch, C.-C. Chang, L. J. Mawst, and T. Earles. "Multidimensional conduction-band engineering for maximizing the continuous-wave (CW) wallplug efficiencies of mid-infrared quantum cascade lasers", *IEEE J. Sel. Top. Quantum Electron*. **19(4)**, 1200312 (2013).

[11] J. D. Kirch, C.-C. Chang, C. Boyle, L. J. Mawst, D. Lindberg III, T. Earles, and D. Botez. "Highly temperature insensitive, low threshold-current density ($\lambda \sim 8.7$- 8.8 μm) quantum cascade lasers", *Appl. Phys. Lett*., **106**, 151106 (2015).

[12] L. J. Mawst, A. Bhattacharya, M. Nesnidal, J. Lopez, D. Botez, J. A. Morris, and P. Zory. "High CW output power and 'wallplug' efficiency Al-free InGaAs/InGaAsP/InGaP double quantum well diode lasers", *Electron. Lett*., **31**, 1153-1154 (1995).

[13] A. Lyakh, C. Pflugl, L. Diehl, Q. J. Wang, F. Capasso, X. J. Wang, J. Y. Fan, T. Tanbuk-Ek, R. Maulini, A. Tsekoun, R. Go, and C. K. N. Patel. "1.6 W high wallplug efficiency, continuous-wave, room temperature quantum cascade laser emitting at 4.6 μm", *Appl. Phys. Lett*., **92**, 111110 (2008).

[14] A. Wittmann. "High-performance quantum cascade laser sources for spectroscopic applications", *Dissertation ETH Nr. 18363*, 112-113 (2009).

[15] P. Price. "Two-dimensional electron transport in semiconductor layers i: phonon scattering", *Ann. Phys.* (*San Diego*), **133**, 217-239 (1981).

CHAPTER THREE

STEP-TAPERED ACTIVE-REGION MID-INFRARED QUANTUM CASCADE LASERS

3.1 Introduction

The active region of conventional $4.5 - 5.0$ μm-emitting quantum cascade lasers (QCLs) is composed of quantum wells and barriers of fixed alloy composition [1]. They suffer severe carrier leakage from the upper laser level to the higher energy levels in the active region. The carrier leakage is evidenced by low characteristic temperatures for both the threshold-current density ($T_0 \sim 140$ K) and the slope efficiency ($T_1 \sim 140$ K) over a wide range of heatsink temperatures above room temperature [2]. As the temperature rise in the active region, ΔT_{act}, is a strong function of both T_0 and T_1, the self-heating of QCL devices is severe under continuous-wave (CW) operation. This, in turn, limits the maximum wallplug efficiency of conventional QCLs under CW mode at room temperature to only $\sim 13\%$ [3].

It has been shown that for $4.5 - 5.0$ μm-emitting QCLs of the double phonon resonance (DPR) depopulation scheme, the primary carrier leakage path for electrons injected into the upper laser level (level 4) is the shunt current through the next-higher energy level, level 5 [4]. As a result, the carrier leakage current is proportional to the scattering rate from level 4 to level 5, which can be approximated by the following equation:

$$\frac{1}{\tau_{45}} \sim \frac{1}{\tau_{54}} \exp(\frac{-E_{54}}{kT_{e4}}), \qquad (3.1)$$

where τ_{45} is the longitudinal optical (LO) phonon scattering time from level 4 to level 5, τ_{54} is the scattering time from level 5 to level 4, E_{54} is the energy difference between level 4 and level 5, T_{e4} is the electronic temperature in level 4. Clearly, in order to significantly suppress carrier leakage, both E_{54} and τ_{54} have to be maximized, while T_{e4} needs to be minimized.

Due to the flexibility offered by the MOCVD growth technique [5], several conduction-band engineered structures in which quantum wells and barriers have varying compositions throughout the laser core have been demonstrated. By using taller barriers and deeper wells in and around the active region, the so-called "Deep-Well" (DW)-QCLs [6] have shown higher characteristic temperatures ($T_0 \sim 243$ K; $T_1 \sim 285$ K) over the heatsink temperatures of $20 - 60°C$, as compared to those for conventional QCLs, due to the larger E_{54} and accordingly suppressed carrier leakage. By tapering the barrier height from the injection barrier to the exit barrier of DW-QCLs, the characteristic temperature for slope-efficiency (T_1) of so-called tapered active-region (TA) QCLs [7] is greatly improved to 797 K over the same heatsink temperature range. In addition to higher T_1, for a 30-stage, 3 mm-long, 19 μm-wide, uncoated TA-QCL device, the measured pulsed threshold current is as low as 0.85A at $T = 20°C$, corresponding to a J_{th} value of ~1.55 kA/cm^2. This J_{th} value is lower by ~ 14% than that for conventional QCLs of same geometry and similar injector doping level (~10^{17} cm^{-3}). Finally, the so-called "shallow-well" TA-QCLs reported by Bai et al. [8] have also demonstrated improved characteristic temperatures ($T_0 \sim 244$ K; $T_1 \sim 343$ K). These QCLs, essentially being TA-type structures without using deep wells [4], have achieved the record-high, single-facet CW wallplug efficiency of 21% at room temperature [9].

Here, we propose 4.8 μm-emitting, step-tapered active-region (STA) QCL structures for complete suppression of carrier leakage. Due to the stepwise tapering of barrier heights in the active region, the STA-QCLs not only possess a significantly large E_{54} (or E_{43}) value, but also minimizes the reduction in E_{54} (or E_{43}) due to Stark shift. The significantly large E_{54} (or E_{43}) in STA-QCL structures results in the complete suppression of carrier leakage. In particular, by comparison with the state-of-the-art shallow-well TA-QCLs, the lasing transition in STA-QCL structures is more vertical, owing to the better spatial wavefunction-overlap between the upper and lower laser levels. The proposed STA-QCLs thus have larger dipole matrix element, and a narrower transition linewidth, when the effect of elastic interface roughness scattering on the intersubband linewidth broadening [10] is considered. These, in turn, result in an overall slightly higher gain cross-section in STA-QCLs than that in shallow-well TA-QCLs. Furthermore, the carrier extraction in the proposed STA-QCLs, similar to shallow-well TA-QCLs, is based on miniband-type extraction. Specifically, for both STA-DPR and STA-SPR QCLs, carriers are resonantly extracted from all the lower active-region levels. On the other hand, by reducing the total number of interfaces, and the number of high-strained layers such as AlAs in the laser core, the thermal resistance of proposed STA-QCLs is only about half of that for shallow-well TA-QCLs. Thus, the projected temperature rise in the active region, ΔT_{act}, is much lower in STA-QCLs compared to shallow-well TA-QCLs, when operated at the maximum wallplug efficiency point in CW operation. Due to the combination of virtual suppression of carrier leakage and much lower core temperature, the projected single-facet, CW maximum walllplug efficiency of STA-QCLs is $\geq 25\%$ at room temperature, close to published predicted limits for mid-infrared 4.8 μm–emitting

QCLs, which therefore makes the proposed STA-QCLs more suitable for long-term, reliable operation at high (≥ 0.5 W) CW powers.

3.2 Background

In this section, both conventional QCLs and other reported conduction-band engineered structures, including DW-QCLs, TA-QCLs, and linear TA-QCLs, are analyzed and compared, by using eight-band $k{\cdot}p$ calculation. For each structure, the conduction band diagram and the squared modulus of relevant wavefunctions of energy levels are first determined. Then, the dipole matrix element of lasing transition, z_{43}, and the lifetimes due to longitudinal optical (LO) phonon scattering between energy levels are calculated. Finally, the global upper-state lifetime τ_{4g}, the global lower-state lifetime τ_{3g}, and the global "effective" upper-state lifetime, $\tau_{up, g}$, an important indicator of threshold current density $J_{th,}$ are estimated respectively, and are compared to those for other structures.

3.2.1 Conventional QCLs

Fig. 3.1 illustrates the calculated conduction band diagram and squared modulus of key wavefuctions for conventional QCLs emitting at $\lambda = 4.7$ μm [11]. The active region of conventional QCLs is based on a strain-compensated $In_{0.669}Ga_{0.331}As/Al_{0.638}In_{0.362}As$ heterostructure, pseudomorphically grown on InP substrates, where the compressive strain in $In_{0.669}Ga_{0.331}As$ quantum wells is balanced by the tensile train in $Al_{0.638}In_{0.362}As$ barriers. The resulting conduction band offset (CBO) is ~ 800 meV, about 50 % larger than that for the lattice-matched $In_{0.53}Ga_{0.47}As/Al_{0.48}In_{0.52}As$ (CBO $= 520$ meV) structure. The lasing transition occurs between level 4 (upper laser level) and level 3 (lower laser

level). At the operating field of 81.5 kV/cm, the dipole matrix element z_{43} is 15. 6 Å. The

global upper state lifetime, τ_{4g}, is calculated by the following equation:

$$\frac{1}{\tau_{4g}} = \frac{1}{\tau_{4\_AR}} + \frac{1}{\tau_{4\_EXTRACTOR}}, \tag{3.2}$$

where τ_{4_AR} are lifetimes corresponding to transitions from level 4 to lower active region

(AR) states (e.g., level 3, 2, and 1), and $\tau_{4\_EXTRACTOR}$ are lifetimes corresponding to

transitions from level 4 to extractor states penetrating into the lower AR region (denoted

as "prime" states, e.g., level 3', level 2', etc.). As $\tau_{43} = 3.57$ ps, $\tau_{42} = 4.28$ ps, and $\tau_{41} =$

12.52 ps, τ_{4_AR} is equal to 1/ (1/3.57 + 1/4.28 +1/12.52) = 1.68 ps. Besides, given $\tau_{42'} =$

16.85 ps, $\tau_{42''} = 35.96$ ps, $\tau_{41'} = 14.32$ ps, $\tau_{4\_EXTRACTOR}$ is 1/(1/16.85 +1/35.96+1/14.32) =

6.37 ps. Hence, $\tau_{4g} = 1/(1/1.68 + 1/6.37) = 1.33$ ps. Similarly, the global lower-state

lifetime, τ_{3g}, is calculated by

$$\frac{1}{\tau_{3g}} = \frac{1}{\tau_{3\_AR}} + \frac{1}{\tau_{3\_EXTRACTOR}}. \tag{3.3}$$

Since $\tau_{32} = 0.31$ ps, $\tau_{31} = 1.85$ ps, $\tau_{32''} = 2.75$ ps, and $\tau_{31'} = 1.03$ ps, τ_{3g} is equal to 1/(1/0.31

+1/1.85 +1/2.75 +1/1.03) = 0.196 ps. Therefore, the global "effective" upper-state

lifetime [12] calculated by the following equation,

$$\tau_{up,g} = \tau_{4g}\left(1 - \frac{\tau_{3g}}{\tau_{43}}\right), \tag{3.4}$$

is 1.25 ps. Finally, due to a small E_{54} value of 43 meV, the corresponding lifetime τ_{54} is

only 0.22 ps in the conventional QCLs.

Fig. 3.1. Conduction-band diagram and squared modulus of key wavefunctions for conventional QCLs emitting at $\lambda = 4.7$ μm.

3.2.2 Deep-Well (DW) QCLs

As illustrated in Fig. 3.2, the active core of DW-QCLs [13] is composed of quantum wells and barriers with varying composition of Ga and Al, respectively. By using both taller barriers ($Al_{0.75}In_{0.25}As$) and deeper wells ($In_{0.68}Ga_{0.32}As$) in the active region than in the injector/extractor region, E_{54} is significantly increased from 43 meV in conventional QCLs to 57 meV in DW-QCLs. Owing to larger E_{54}, the carrier leakage is significantly

suppressed in DW-QCLs, which is evidenced by much higher measured characteristic temperatures T_0 and T_1, 243 K and 285 K, respectively. Despite higher T_0 and T_1, the measured threshold current density J_{th} for DW-QCLs is basically the same as that for conventional QCLs. For an uncoated, 3mm-long DW-QCL device, the measured J_{th} is ~ 1.8 kA/cm^2 at 20°C.

The reason why the DW-QCLs have similar J_{th} to that for conventional QCLs can be understood by further examining their wavefunctions and corresponding lifetimes. At the field of 71.5 kV/cm, the lower laser level (level 3) and level 2 in DW-QCLs are similar to those in conventional QCLs, resulting in comparable lifetimes τ_{43_total},

$$\tau_{43\_total} = \cfrac{1}{\cfrac{1}{\tau_{43}} + \cfrac{1}{\tau_{43'}}} = \cfrac{1}{\cfrac{1}{3.35} + \cfrac{1}{25.8}} = 3.35 \ ps, \quad (3.5)$$

and τ_{42_total},

$$\tau_{42\_total} = \cfrac{1}{\cfrac{1}{\tau_{42}} + \cfrac{1}{\tau_{42'}}} = \cfrac{1}{\cfrac{1}{8.34} + \cfrac{1}{8.00}} = 4.08 \ ps, \quad (3.6)$$

where τ_{43_total} and τ_{42_total} are overall lifetimes corresponding to respective transitions from level 4 to level 3 and 2, after taking into account the coupling between level 3 and 3', and level 2 and 2', respectively.

On the contrary, due to the strong quantum confinement, level 1 in DW-QCLs, instead of peaking up in the last quantum well of the active region, is drawn towards its up stream, having the maximum field in the third quantum well. As a result, due to the better spatial overlap between wavefunctions of level 4 and level 1, the corresponding lifetime τ_{41} is only 4.11 ps in the DW-QCLs, much lower compared to that (τ_{41} = 12.52 ps) in conventional QCLs. This in turn, leads to a lower τ_{4g} value of 1.21 ps in the DW-QCLs.

Given similar τ_{3g}, the global "effective" upper-state lifetime $\tau_{up, g}$ in DW-QCLs ($\tau_{up, g}$ = 1.11 ps) is therefore ~ 10% lower than that for conventional QCLs.

However, based on the calculation, the ratio of leakage current density to threshold current density, J_{leak} / J_{th}, is reduced from ~ 15% in conventional QCLs to ~ 8.8% in DW-QCLs [2]. Thus, in DW-QCLs, the effect of having lower global "effective" upper-state lifetime $\tau_{up, g}$ is offset by the effect of reduced threshold current density J_{th} due to the suppression of carrier leakage, resulting in basically the same J_{th} as conventional QCLs.
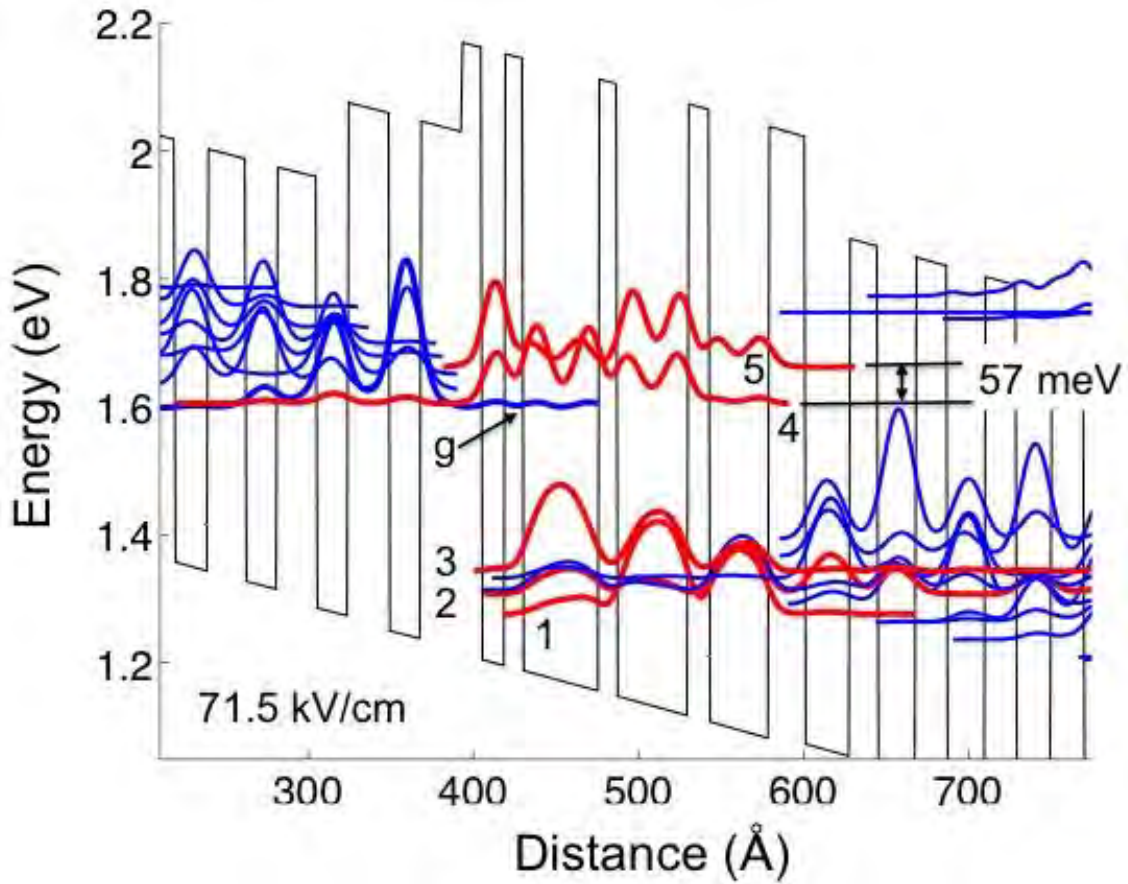
Fig. 3.2. Conduction-band diagram and squared modulus of key wavefunctions for DW-QCLs emitting at $\lambda = 4.8$ μm.

3.2.3 Tapered Active-Region (TA) QCLs

The conduction band diagram and squared modulus of relevant wavefunctions for the moderate tapered active-region (TA) QCLs [7] are shown in Fig. 3.3. The main difference that distinguishes moderate TA-QCLs from DW-QCLs is the reduced Al composition (65%) of the first two barriers in the active region. Due to this asymmetry, E_{54} in moderate TA-QCLs is increased from 57 meV in DW-QCLs to 73 meV at 74 kV/cm, which results in further suppression of carrier leakages from level 4. In addition to larger E_{54}, the increased asymmetry in TA-QCL structure draws the antisymmetric state level 5 towards the down stream of the active region, and reduce its wavefuncion-overlap with the level 4's wavefucntion. The reduced overlap between level 4 and 5 allows for τ_{54} to increase from 0.32 ps in DW-QCLs, to 0.44 ps in TA-QCLs. Moreover, for the ground states in the active region, level 2 is also an antisymmetric state, whereas level 1 and level 3 are symmetric states (Fig. 3.4). Similar to level 5, level 2 is drawn more towards the down stream of the active region, and therefore, τ_{42_total} is larger (τ_{42_total} = 1/(1/τ_{42} + 1/$\tau_{42'}$) = 1/(1/5.29 +1/35.68) =4.61 ps) in TA-QCLs compared to DW-QCLs. Given τ_{43} = 3.17 ps, τ_{4g} = 1.29 ps, and τ_{3g} = 0.21 ps, the global "effective" upper-state lifetime, $\tau_{up, g}$ in TA-QCLs is

$$\tau_{up,g} = \tau_{4g}\left(1 - \frac{\tau_{3g}}{\tau_{43}}\right) = 1.29\left(1 - \frac{0.21}{3.17}\right) = 1.21\ ps. \qquad (3.7)$$

Consequently, by moderate tapering the barrier height from the injection barrier to the exit barrier, not only is the carrier leakage further suppressed in the moderate TA-QCLs due to larger E_{54}, but the upper-level lifetime is also recovered to basically the same as that in the conventional QCLs. Given the same dipole matrix element (z_{43} =15.6 Å), the

threshold current density J_{th} in TA-QCLs is thus lowered compared to both DW- as well as conventional QCLs by ~ 10 % due to carrier-leakage suppression.

Another important parameter in mid-IR QCL active-region design is Δ_{inj}, the energy difference between the lower laser level (level 3 in DPR case) and the quasi-Fermi level in the next injector. Having a large Δ_{inj} would prevent hot electrons from significantly backfilling the lower laser level via the absorption of LO phonons. However, if Δ_{inj} is too large at the operating field, the resulting large voltage drop across each stage would add up and lead to an overall high operating voltage of QCL devices, and in turn reduce their wallplug efficiency. To achieve a tradeoff, the typical value of ~ 150 meV for Δ_{inj} is used in the conventional, DW-, and moderate TA-QCL structures.
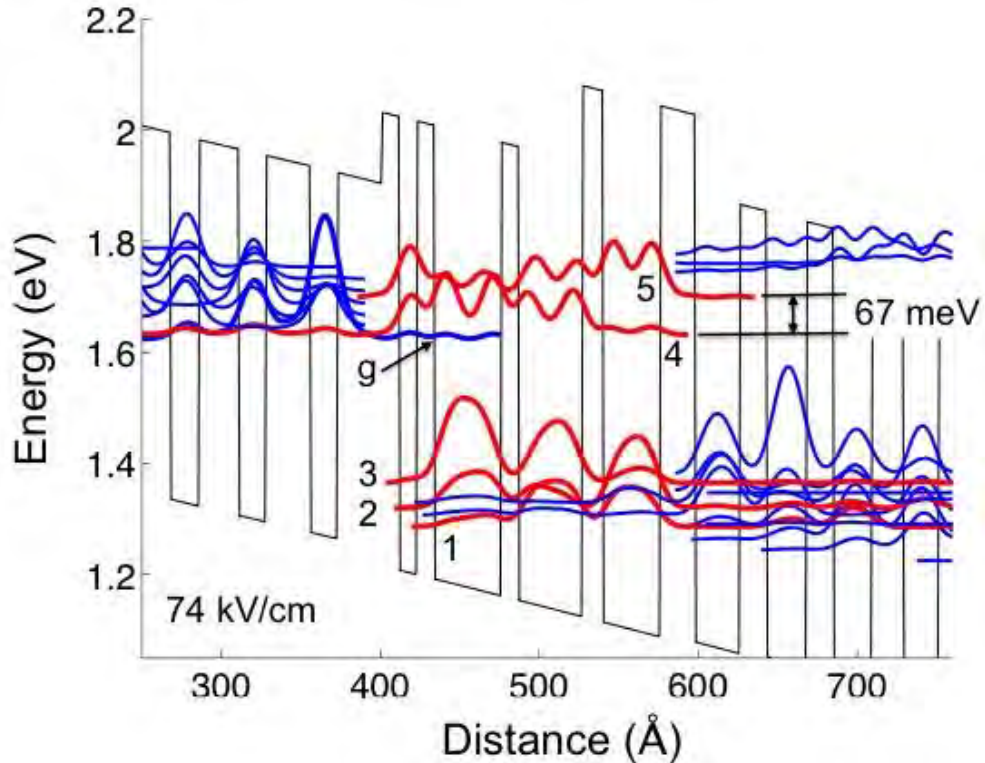
Fig. 3.3. Conduction-band diagram and squared modulus of key wavefunctions for moderate TA-QCLs emitting at $\lambda = 4.8$ μm.
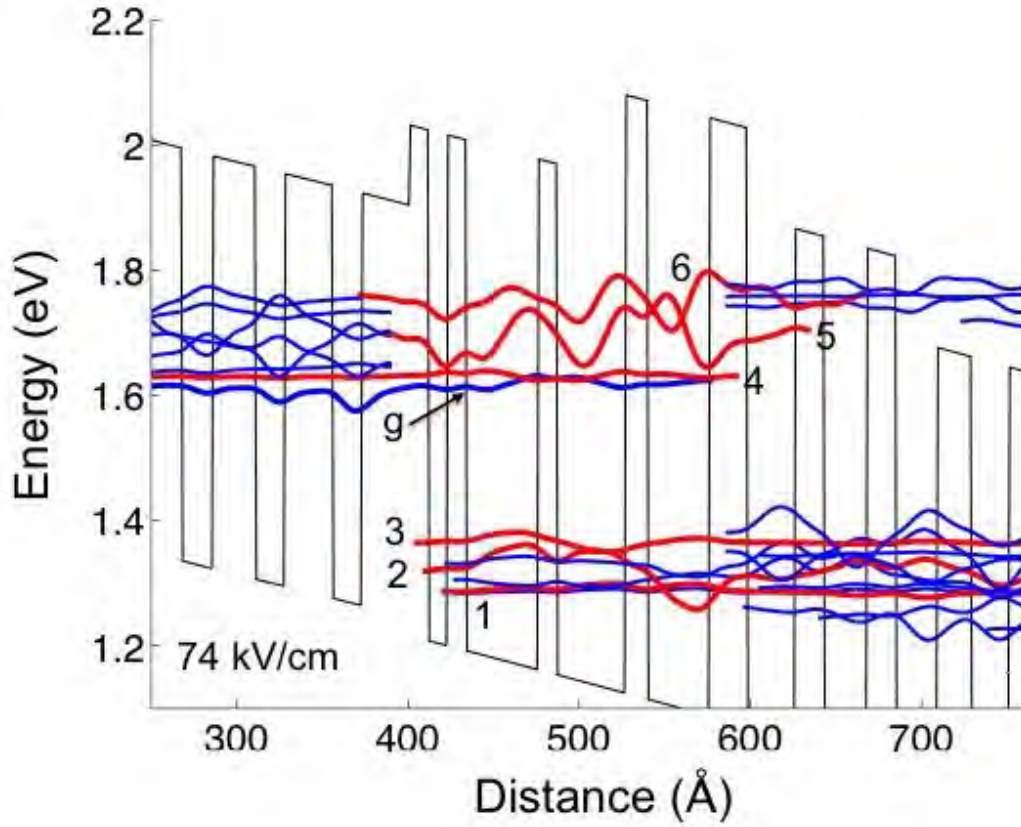
Fig. 3.4. Conduction-band diagram and the amplitude of key wavefunctions for moderate TA-QCLs emitting at $\lambda = 4.8$ μm.

3.2.4 Linear Tapered Active-Region (Linear-TA) QCLs

The conduction band diagram and squared modulus of relevant wavefunctions for the linear tapered active-region (Linear-TA) QCLs are shown in Fig. 3.5. The Al compositions of AlInAs barriers in the active region are 59%, 64%, 69%, and 74%, respectively. Therefore, by linearly tapering the barrier height in the active region, the asymmetry in the Linear-TA-QCL structures is further increased compared to that in moderate TA-QCLs, which in turn results in larger E_{54} and τ_{54} values. At 73.5 kV/cm, both E_{54} and τ_{54} in Linear-TA-QCLs are increased from 67 meV to 77 meV and from 0.44 ps to 0.49 ps, respectively, allowing for further suppression of carrier leakage compared

to moderate TA-QCLs. Moreover, as can be seen in Fig. 3.5, the lower laser level (level 3) in Linear-TA-QCLs has similar field distribution in the second and third quantum wells in the active region. This results in a slightly reduced dipole matrix element (z_{43} = 15.3 Å), in comparison with moderate TA-QCLs (z_{43} = 15.6 Å). It is also worth noting that, the carrier extraction in the lower active region of Linear-TA-QCLs is different than that in moderate TA-QCLs. For moderate TA-QCLs, similar to QCLs of DPR-type active-region design, resonant extraction only occurs from level 2. On the contrary, the carrier extraction scheme in Linear-TA-QCL structures is essentially similar to the mininband extraction in QCLs based on the bound-to-continuum (BC) active-region design, where both level 3 and level 2 are strongly coupled to the extractor states level 3' and 2' penetrating into the lower active region [18]. That is, there is resonant extraction from both level 3 and level 2. The corresponding coupling strengths $|\Omega_{33'}|$ and $|\Omega_{22'}|$ for 3/3' and 2/2' are 7.5 and 6.3 meV, respectively. The resonance fields for 3/3' and 2/2' are 71 kV/cm and 74 kV/cm, very close to the operating field (73.5 kV/cm) of Linear-TA-QCLs. Thus, at and above threshold, the strong coupling between level 3 and 3' in Linear-TA-QCLs provides direct carrier extraction via level 3' upon the lasing transition, and therefore ensures the fast depopulation of level 3, which is of particularly importance for achieving high-power performance under CW operation at high temperatures. Due to this miniband-type extraction, the global lower-state lifetime τ_{3g} for Linear-TA-QCLs is only 0.18 ps, the lowest when compared to conventional and other conduction-band-engineered QCLs. Despite a slightly smaller τ_{4g} (1.25 ps) is found when compared to moderate TA-QCLs, $\tau_{up,g}$ for Linear-TA-QCLs is 1.19 ps, basically the same as that (1.21 ps) for moderate TA-QCLs. As a result, the gain cross-section in Linear-TA-QCLs,

which scales linearly with the product of z_{43}^2 and $\tau_{up,\,g}$, is similar ($\sim$ 95 %) to that in moderate TA-QCLs, when only the inelastic LO phonon scattering is considered.

The calculated z_{43}, τ_{3g}, τ_{4g}, $\tau_{up,\,g}$, τ_{54}, and E_{54} values for conventional, DW- moderate TA-, and Linear-TA-QCLs are summarized in Table 3.1.

	z_{43} (Å)	τ_{3g} (ps)	τ_{4g} (ps)	$\tau_{up, g}$ (ps)	τ_{54} (ps)	E_{54} (meV)
Conventional	15.6	0.20	1.33	1.25	0.22	43
DW	15.7	0.25	1.21	1.11	0.32	57
Moderate-TA	15.6	0.21	1.29	1.21	0.44	67
Linear-TA	15.3	0.18	1.25	1.19	0.49	77

Table 3.1 Comparison of z_{43}, τ_{3g}, τ_{4g}, $\tau_{up, g}$, τ_{54}, and E_{54} values in Conventional, DW-, moderate TA, and Linear-TA QCL structures.
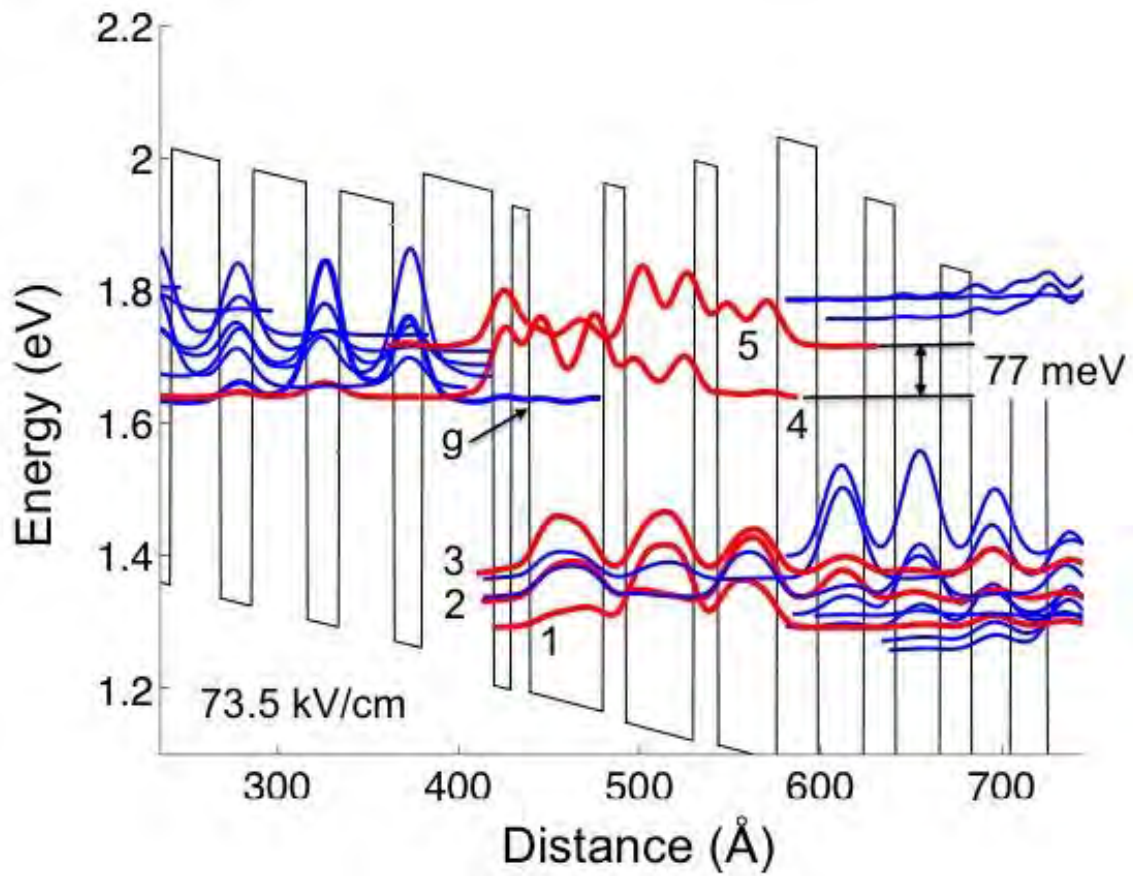
Fig. 3.5. Conduction-band diagram and squared modulus of key wavefunctions for linear TA-QCLs emitting at $\lambda = 4.8$ μm.

## 3.3 Step-Tapered Active-Region (STA) QCLs

Fig. 3.6 shows the calculated conduction band diagram and squared modulus of relevant wavefunctions, at the threshold field of 74 kV/cm, for 4.7 μm-emitting step-tapered active-region (STA) QCLs of DPR depopulation scheme. The upper and lower lasing levels are level 4 and level 3, respectively. As can be seen, the active-region barrier heights are stepwise tapered, in that the first two barriers are $Al_{0.60}In_{0.40}As$ and $Al_{0.67}In_{0.33}As$, and the third and the exit barriers are much taller: $Al_{0.93}In_{0.07}As$ and $Al_{0.80}In_{0.20}As$. The advantages of stepwise tapering of barrier heights in the active region are two-folds. First, similar to the moderate TA-QCLs and Linear-TA-QCLs, the strong asymmetry in STA-QCLs due to the stepwise tapering leads to a significantly large E_{54} value, increased from 77 meV for Linear-TA-QCLs to 91 meV for STA-QCL structures. Moreover, τ_{54} is also increased to a high value of 0.86 ps in STA-QCLs. Thus, from Eq. (3.1), carrier leakages from level 4 in STA-QCLs is further suppressed compared to Linear-TA-QCLs. Second, since the anti-crossing between level 4 and level 5 occurs at a field much higher than the threshold field, as the applied field increases above the threshold, E_{54} gradually decreases due to Stark effect [14]. The decrease in E_{54}, δE_{54}, can be described by

$$\delta E_{54} = -(z_5 - z_4)eE, \tag{3.8}$$

where z_4 and z_5 are the coordinates of the centroids of the squared modulus of wavefunctions for level 4 and level 5, e is the electric charge, and E is the strength of applied electric field. As compared to Linear-TA-QCLs, the effect of stepwise tapering in STA-QCLs reduces $z_5 - z_4$ by increasing the coupling between level 4 and level 5, and hence minimizes the reduction in E_{54} value due to Stark effect.

In addition to stepwise tapering of barrier heights, the quantum wells (QWs) in the active regions of STA-QCLs are $In_{0.68}Ga_{0.32}As$ layers, which are deeper than the QWs in the injector/extractor regions. The injector/extractor regions are mainly composed of $In_{0.64}Ga_{0.36}As$ QWs and $Al_{0.56}In_{0.44}As$ barriers. The entire structure of STA-QCLs is therefore strain-compensated with a net strain value of 0.01% tensile. Other design parameters at 74 kV/cm for STA-QCLs are: 13.8 Å for the dipole matrix element z_{43}, 1.38 ps for the global upper-state lifetime τ_{4g}, 0.23 ps for global lower-state lifetime τ_{3g}, and 1.28 ps for the global "effective" upper-state lifetime, $\tau_{up, g}$. The wavefunctions in the lower active region of STA-QCLs are similar to those in the typical DPR-based structures, in which carrier extractions are mainly from level 2 and level 1 upon the LO phonon emission. Level 2 is strongly coupled to the extractor state level 2' (green-colored state) with a coupling strength of 9.2 meV, and level 1 and level 1' (pink-colored state) are only weakly coupled with a coupling strength of 5.2 meV. To prevent carriers from backfilling the lower laser level, Δ_{inj} is designed to be 149 meV.

The STA-QCL structure described above was grown on a $(1-2) \times 10^{17}$ cm^{-3}-doped InP substrate via MOCVD. A 0.5 μm-thick InP buffer layer was first grown on the substrate, followed by a 0.35 μm-thick $In_{0.53}Ga_{0.47}As$ confinement layer. The core-layer thickness (in Å) for one period, starting right after the exit barrier, are: *28*, 17, [23], 17, [26], 20, (23), 22, <u>(20), 23, (18), 25</u>, (17), 29, (17), 18, [**24**], **11**, [*11*], **42**, [*11*], **38**, *13*, **35**, (*20*), where bold italic scripts are: $In_{0.66}Ga_{0.34}As$ quantum wells (QWs), bold normal scripts are $In_{0.68}Ga_{0.32}As$ QWs, bracketed normal scripts are $In_{0.64}Ga_{0.36}As$ QWs, normal scripts are $Al_{0.56}In_{0.44}As$ barriers, bracketed bold normal scripts are $Al_{0.65}In_{0.35}As$ barriers, bracketed bold italic scripts are $Al_{0.60}In_{0.40}As$ barriers, bracketed italic scripts are $Al_{0.67}In_{0.33}As$

barriers, italic scripts are $Al_{0.93}In_{0.07}As$ barriers. The normal and italic scripts in parentheses are $In_{0.64}Ga_{0.36}As$ QWs and $Al_{0.80}In_{0.20}As$ barriers, respectively. The underlining indicates a nominal doping of $10^{17}cm^{-3}$. Atop the 30-period active core, following layers were grown: 0.35 μm-thick $In_{0.53}Ga_{0.47}As$ confinement layer, 2 μm-thick 2×10^{16} cm^{-3}–doped InP layer, 1.5 μm-thick 1×10^{17} cm^{-3}–doped InP layer, 0.5 μm-thick 5×10^{18} cm^{-3}–doped plasmon InP layer, and 0.15 μm-thick 2×10^{19} cm^{-3}–doped InP cap layer.
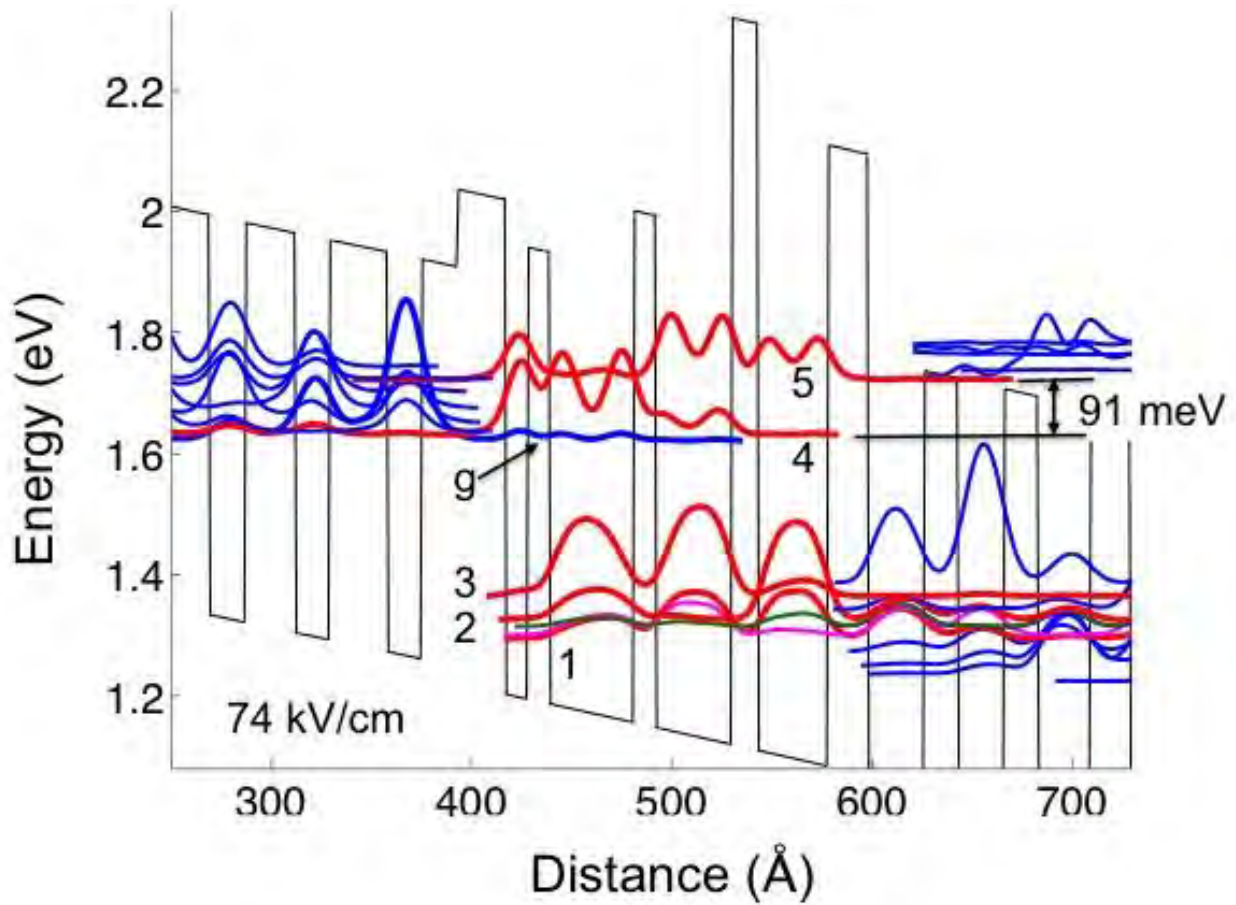
Fig. 3.6. Conduction-band diagram and squared modulus of key wavefunctions for STA-QCLs emitting at λ ~ 4.7 μm.

After the crystal growth, devices were fabricated into 21 μm-wide ridges using standard contact lithography and wet etching using HBr: HNO₃: H₂O = 1: 1: 14 solutions. A 350 nm-thick Si₃N₄ layer was then deposited via plasma-enhanced chemical vapor deposition (PECVD) to provide current confinement. Atop ridges 8 μm-wide contact windows were lithographically defined and opened via reactive-ion etching (RIE), followed by the e-beam evaporation of Ti/Au (90 nm/300 nm) on the epi-side. After substrate thinning and backside metallization using Ge/Au/Ag/Au (15 nm/27 nm/50 nm/150 nm), 3mm-long bars were first cleaved, and laser chips were then separated and mounted epi-side up for testing on Cu submounts. Fig. 3.7 shows cross-sectional scanning electron microscopy (SEM) images of fabricated STA devices.
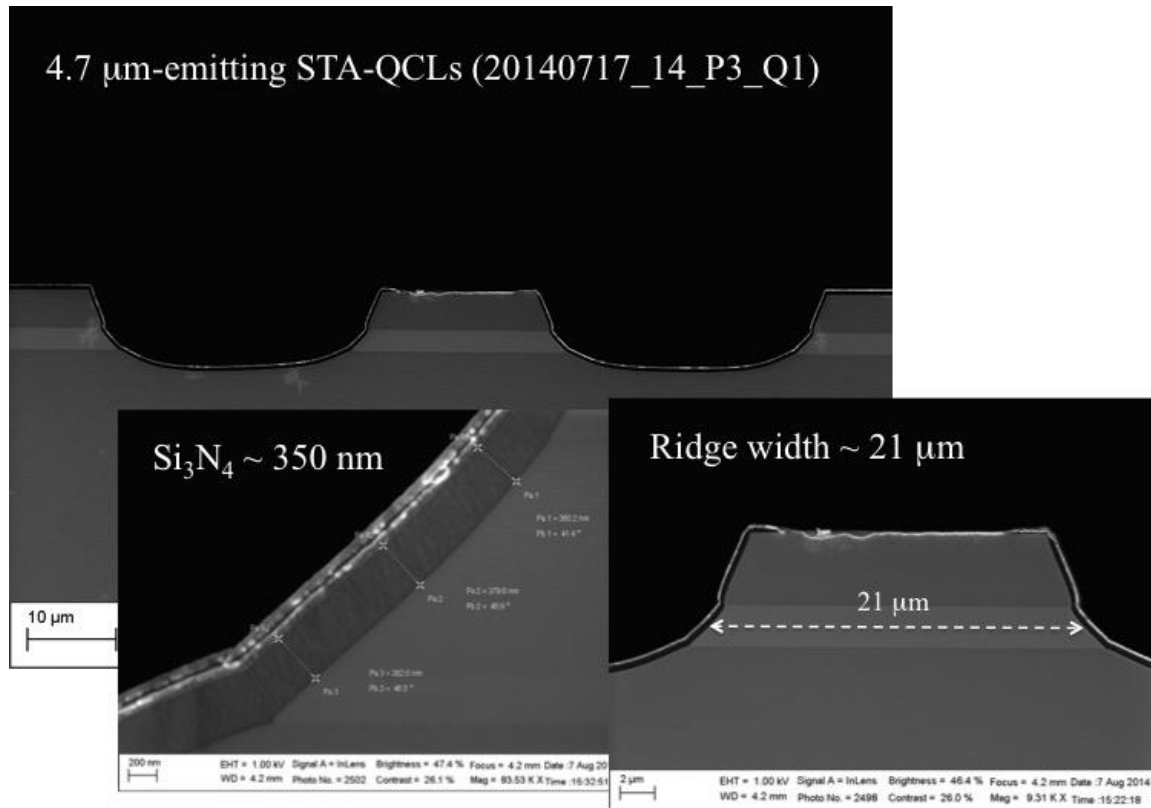
Fig. 3.7. Cross-sectional SEMs of fabricated STA-QCL devices

The fabricated STA-QCL devices were tested in pulsed mode (200ns, 100Hz) over the heatsink temperature range of 20 – 60 °C. Fig. 3.8 shows the typical light-current-voltage (*L-I-V*) characteristics for 3mm-long, 21 μm-wide, uncoated STA devices at 20 °C. Unfortunately, we found out in our experiment that the injector doping level for these STA devices is inadvertently higher (1.8×10^{17} cm^{-3}) than the designed value (10^{17} cm^{-3}). As can be seen in chapter 2, the high injector doping results in larger waveguide loss due to increased free carrier absorption and intersubband (ISB) absorption, as well as more severe electron backfilling. These, in turn, lead to an increased threshold current density J_{th} and reduced slope efficiency. For these STA devices, the measured threshold current density is 1.98 kA/cm^2. The two-facet slope efficiency measured using f/1 optics is only 1.05 W/A, which is lower than that (1.56 W/A) for moderate TA-QCLs at 20°C. The measured emission wavelength, as shown in the inset of Fig. 3.8, is 4.95 μm.

Fig. 3.9 and 3.10 show the temperature dependence of J_{th} and the slope efficiency over the 20 – 60 °C range in heatsink temperature, respectively. The characteristic temperature for threshold current density, T_0, defined from $J_{th}(T_{ref} + \Delta T) = J_{th}(T_{ref}) \exp (\Delta T/T_0)$, where $T_{ref} + \Delta T$ is the heatsink temperature and T_{ref} is the reference temperature, is found to have a value of 225 K. In contrast, T_0 for high-performance 4.5-5.0 μm-emitting conventional QCLs is only ~ 140 K. Clearly, despite the large waveguide loss and backfilling resulting from the inadvertently high injector doping, the carrier leakage is indeed substantially suppressed in these STA-QCL devices. On the other hand, the characteristic temperature for differential quantum efficiency, T_1, defined from $\eta_d(T_{ref} + \Delta T) = \eta_d(T_{ref}) \exp (-\Delta T/T_1)$, is 235 K (Fig. 3.10). Although higher than typical T_1 values (~ 140 K) for conventional QCLs, this T_1 value is only comparable to that (285 K) for

DW-QCLs, and is far lower compared to that (797 K) for moderate TA-QCLs. The low T_1 value found in STA-QCL devices suggests that the slope efficiency decreases very rapidly as the heatsink temperature increases. This strong temperature dependence of slope efficiency results from the large waveguide loss due to free carrier absorption and ISB absorption in the heavily doped injectors. Therefore, as can be seen in Chapter 2, despite suppressed carrier leakages, the effect of high injector doping dominates and causes low T_1 value in these STA devices. Nonetheless, these preliminary experimental data have proven the successful suppression of carrier leakage in the proposed STA-DPR QCL structure, and both high T_0 and T_1 values are expected once the injector doping in the crystal growth is optimized.
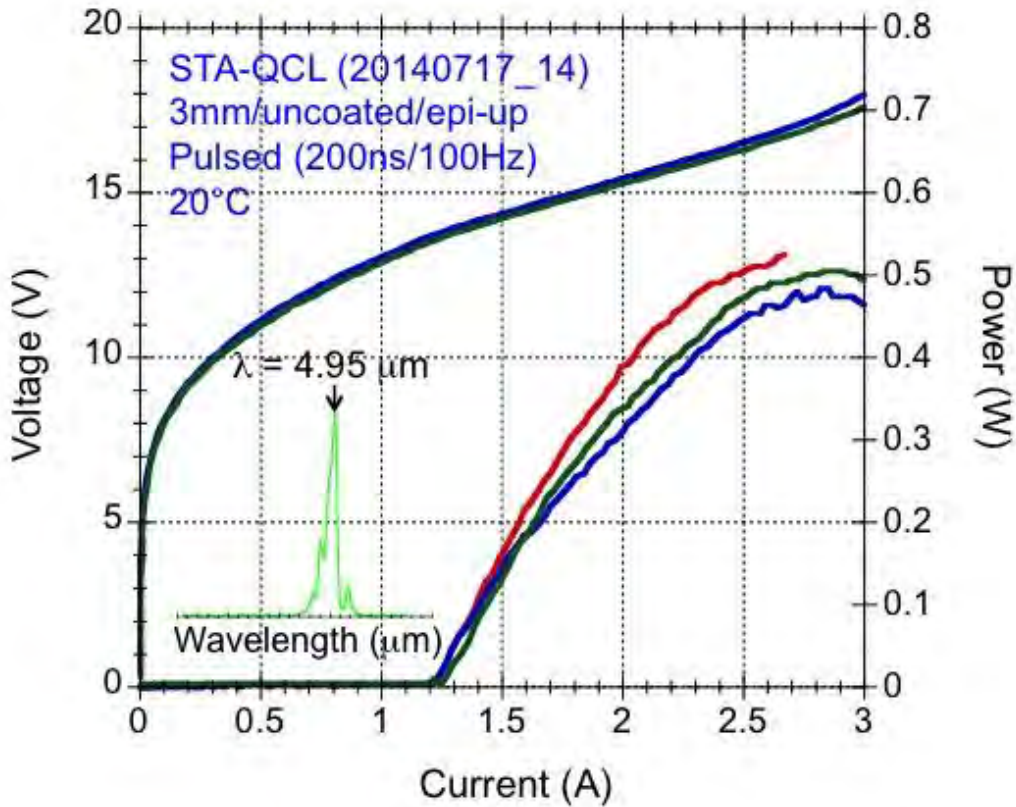
Fig. 3.8. *L-I-V* characteristics for fabricated STA-QCL devices in pulsed mode at 20°C.
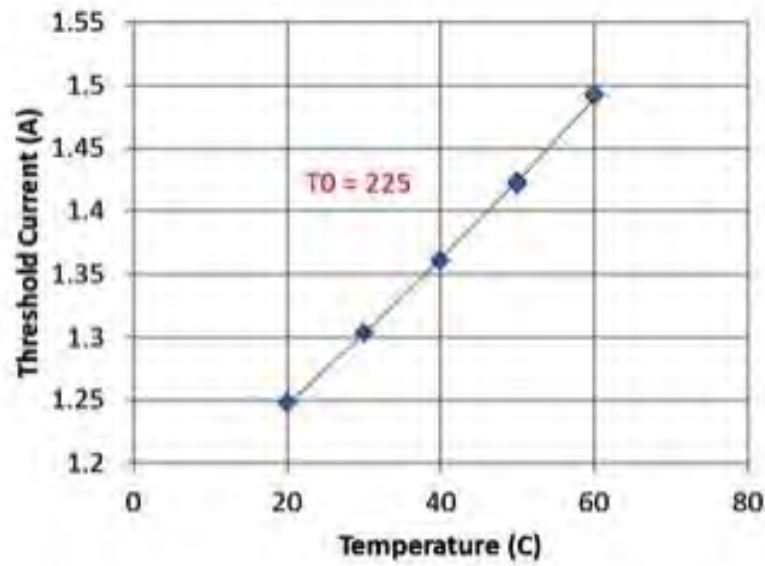
Fig. 3.9. Temperature dependence of threshold current over heatsink temperature of 20 −

60°C. T_0 is the characteristic temperature for threshold current density.
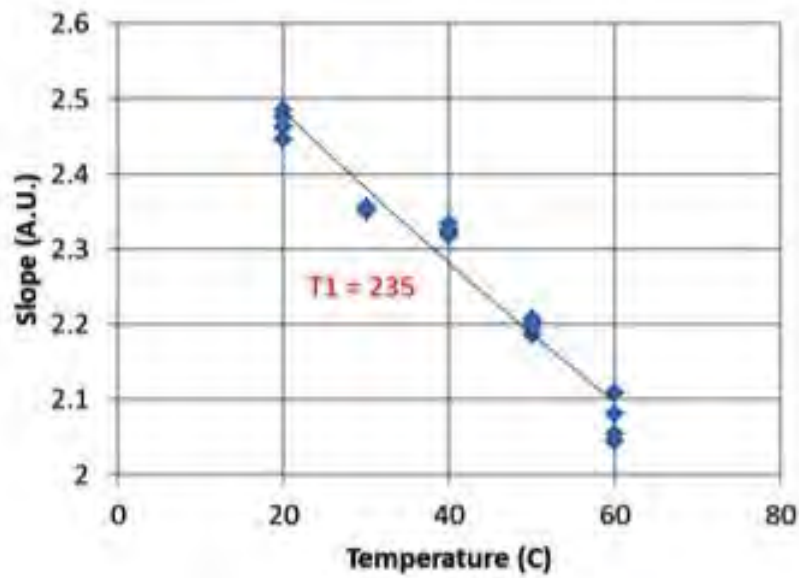
Fig. 3.10. Temperature dependence of slope efficiency over heatsink temperature of 20 −

60°C. T_1 is the characteristic temperature for slope efficiency.

It is also noted that the lasing transition in the proposed STA-QCL structures is slightly diagonal, in that the level 4 and level 3 have their field peaking up in the adjacent quantum wells, resulting a smaller z_{43} than that for conventional QCLs. Moreover, if the elastic intersubband scattering due to the interface-roughness is taken into account, the diagonal transition would lead to a broader electroluminescence linewidth [10] and in turn reduce the gain cross-section, since the transition experiences more interface imperfection from the variation during the crystal growth. It has been shown by Lykah et al. [15] that, the linewidth of electroluminescence from MOCVD grown materials is larger than that from MBE grown materials by $\sim$ 25%. As the conduction band engineered structures in general need to be grown by MOCVD, it is critical to reduce the diagonality of lasing transitions in STA-QCLs to minimize the effect of interfaces.

The lasing transition can be made more vertical by further adjusting the width and depth of quantum wells in the active region of STA-QCLs, so that both upper and lower lasing levels are peaking up in the same well. Specifically, in order to maximize the field of level 4 in the second quantum well in the active region, the width of first quantum well has to be reduced. By thinning the first well width, the "bare" state provided by this quantum well is well above level 4 in energy. Thus, level 4 is less coupled to this state, and its field in the first thin well is therefore minimized and mainly concentrated in the second well. On the other hand, level 3 in STA-QCLs, as can be seen in Fig. 3.6, has its highest field in the third quantum well. To pull its field further toward the second well for better spatial overlap with level 4, one can either reduce the width of the second well, or make this well shallower, i.e., increase the Ga composition of InGaAs well, to enhance the field confinement. In addition to making the lasing transition vertical, the carrier

extraction in the lower active region can also be significantly improved by employing miniband-type extraction, where carriers are resonantly extracted from all the lower levels [18].

Based on the aforementioned design rules, an improved 4.7 μm-emitting STA-QCL structure is also designed, and its conduction band diagram as well as relevant wavefunctions are illustrated in Fig. 3.11. In this improved STA structure, the width of the first thin well in the active region is reduced from 11 A to 10 A. As can be seen, in comparison with the original STA-QCLs described above, this significantly increases the field confinement of level 4 in the second quantum well. Besides, to compensate for the increase in energy of level 4 by thinning the first well, the first barrier in the active region is replaced by shorter $Al_{0.59}In_{0.41}As$ barrier, and the Al composition of second barrier is also reduced from 67 % to 65 %. On the other hand, the second well is made shallower by using $In_{0.60}Ga_{0.40}As$ layers so that level 3 has more field distributed in the second well than in the third well. With these adjustments, the spatial overlap between level 4 and level 3 in the improved STA-QCLs is significantly increased, resulting in a more vertical lasing transition, and in turn, a much larger dipole matrix element z_{43} of 15.3 A. Although the global effective upper-state lifetime $\tau_{up, g}$ is reduced from 1.28 ps to 1.15 ps, the product of z_{43}^2 and $\tau_{up, g}$, the figure of merit for gain cross-section, is larger in the improved STA-QCL structures than in the original STA-QCLs by ~10%.

The intersubband linewidth broadening, $2\gamma_{ul}$, due to the interface-roughness scattering can be estimated by [10]

$$2\gamma_{ul} = \frac{\pi m^*}{\hbar^2}\Delta^2\Lambda^2 \sum_i \delta U^2(z_i)[\varphi_u^2(z_i) - \varphi_l^2(z_i)]^2, \qquad (3.9)$$

where the sum is calculated for all the interfaces, Δ is the average rms height of roughness, Λ is the correlation length characterizing the lateral size of the roughness in the plane of interfaces, $\delta U(z_i)$ is the magnitude of conduction band offset at the interface i, $\varphi_{u,l}(z_i)$ are the amplitude of electron wavefunctions for the upper (u) and lower (l) lasing levels evaluated at the interface i. Given the same active region design, in reality the magnitudes of both Δ and Λ are primarily determined by the growth conditions, such as growth temperature. For mid-IR QCLs grown via MBE, the typical values of interface roughness parameters are ~ 0.15 nm for the step height of roughness, and ~ 6 nm for the correlation length [16].

To quantitatively compare the intersubband linewidth broadening due to interface roughness scattering in two STA-QCL designs, we first assume that the interface parameters Δ and Λ are the same for both structures for a given set of epitaxial growth conditions. According to Eq. (3.9), the linewidth broadening can therefore be estimated by calculating the term $\sum_i \delta U^2(z_i)[\varphi_u^2(z_i) - \varphi_l^2(z_i)]^2$. Furthermore, in order to take into account the oscillator strength for each transition, we sum over this term for all the transitions from upper laser level (level 4) to the lower states in the active region weighted by a factor of $z_{4l}^2 / \sum_l z_{4l}^2$ [17], where l corresponds to level 1 to 3 as well as other penetrating extractor states. This weighted average of $\sum_i \delta U^2(z_i)[\varphi_u^2(z_i) - \varphi_l^2(z_i)]^2$ is then used as the measure of intersubband linewidth broadening in each QCL structure [10].

The calculated $\delta U^2[\varphi_4^2(z_i) - \varphi_3^2(z_i)]^2$ values for transition from level 4 to level 3 at individual interfaces in the active region are denoted by black triangles in Fig. 3.12 for both the original and the improved STA-QCL structures. As can be seen, the magnitude

of this roughness term at each interface is basically the same for both STA structures, except for the one between the third well and the third barrier, at which the calculated roughness term is much smaller in the improved STA-QCL structure than that in the original STA-QCLs. The weighted average values of $\sum_i \delta U^2(z_i)[\varphi_u^2(z_i) - \varphi_l^2(z_i)]^2$ are 0.0158 eV^2/nm^2 and 0.0137 eV^2/nm^2 for the original and improved STA-QCLs, respectively. Apparently, by making the lasing transition more vertical, the intersubband linewidth broadening due to interface roughness is reduced by a factor of ~13.3 % in the improved STA-QCLs. Therefore, when only taking into account the intersubband linewidth broadening due to interface roughness, the overall gain cross-section is larger in the improved STA-QCLs than in the original STA-QCLs by ~27 %.
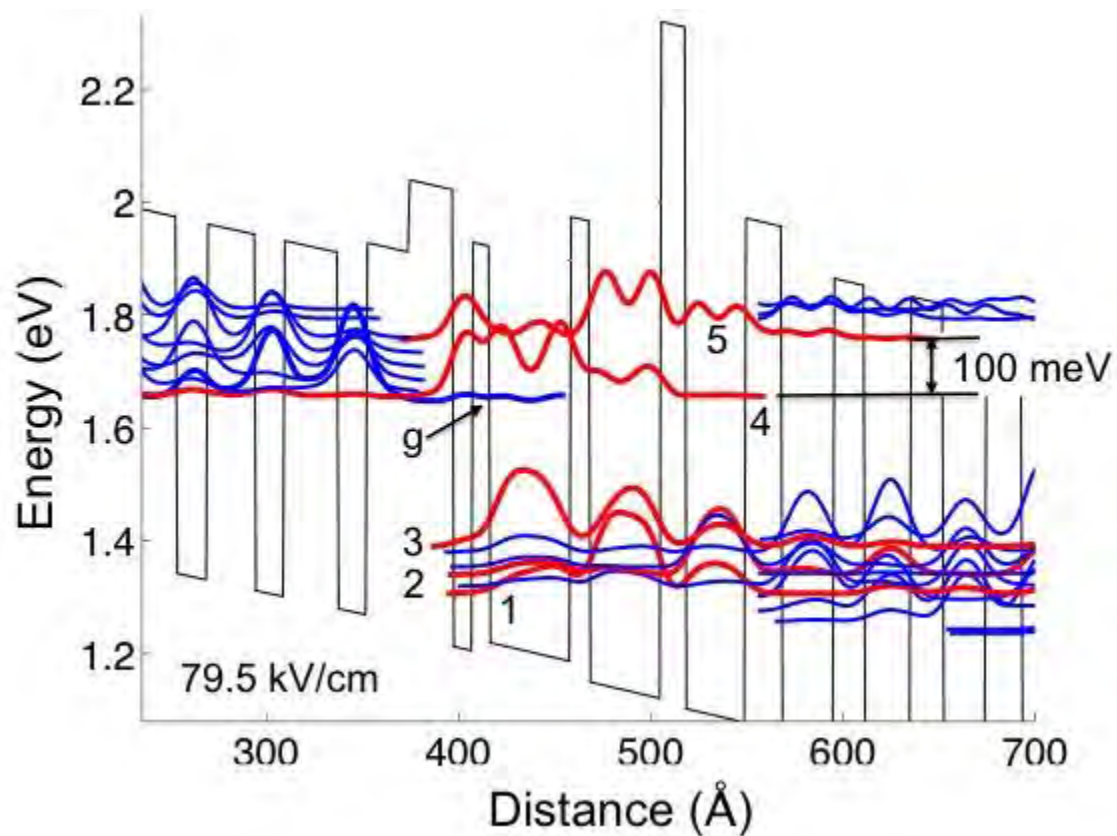
Fig. 3.11. Conduction-band diagram and squared modulus of key wavefunctions for improved STA-QCLs emitting at $\lambda \sim 4.7$ μm.
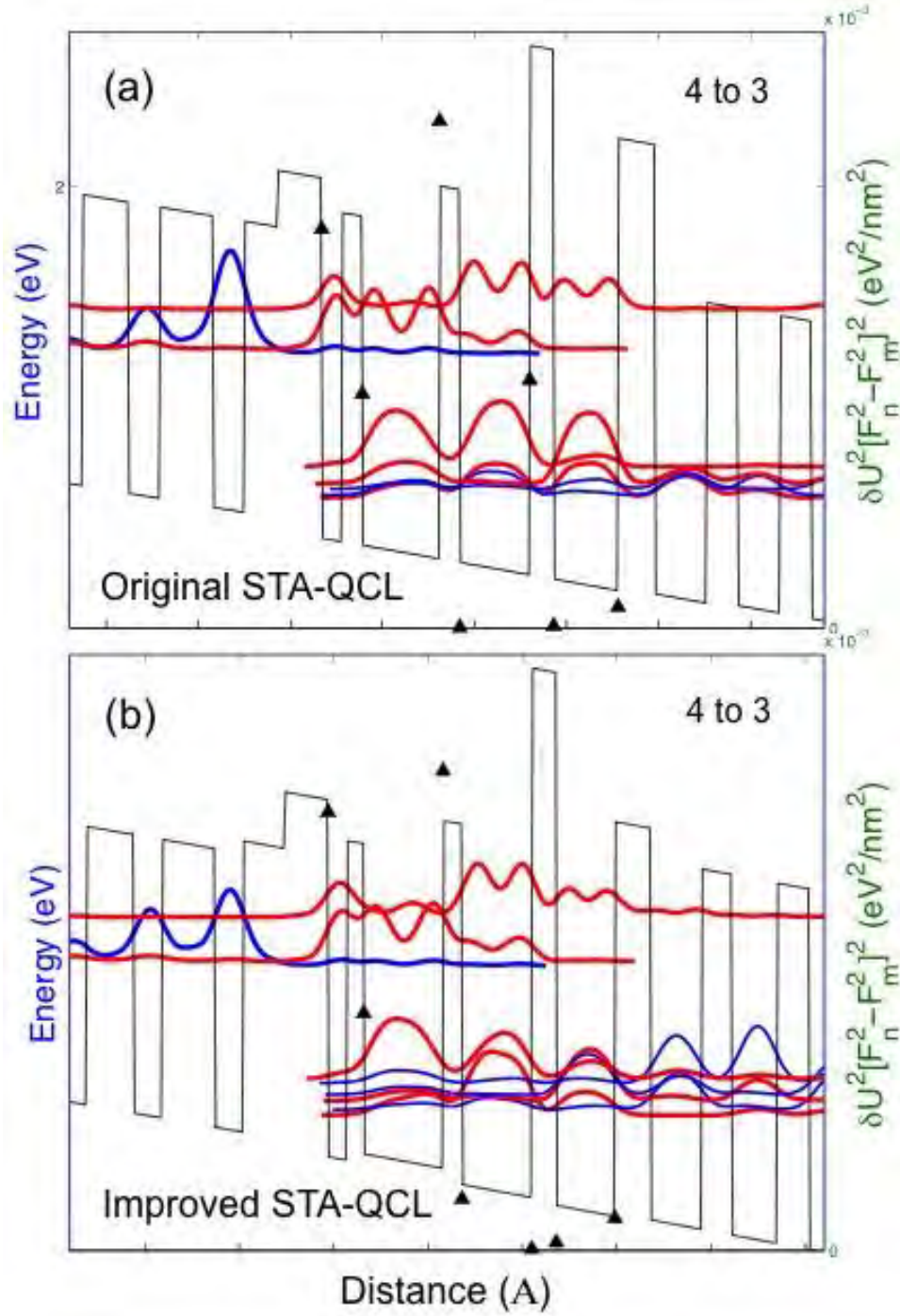
Fig. 3.12. Calculated $\delta U^2[\varphi_4^2(z_i) - \varphi_3^2(z_i)]^2$ for transition from level 4 to level 3 at individual interfaces in the active region for (a) the original STA-QCL; and (b) the improved STA-QCL structure. The value of $\delta U^2[\varphi_4^2(z_i) - \varphi_3^2(z_i)]^2$ at each interface is denoted by the black triangle.

Besides a more vertical lasing transition, the barrier height of the exit barrier in the improved STA-QCL structure is reduced by replacing $Al_{0.80}In_{0.20}As$ with $Al_{0.70}In_{0.30}As$ layers. Due to a shorter exit barrier, the extractor states penetrate more into the active region, which in turn couples much more strongly to the lower levels in the active region. Specifically, as shown in Fig. 3.11, at threshold (79.5 kV/cm) the lower laser level (level 3) is strongly coupled to the extractor state 3' with an energy separation of 10.7 meV. Their splitting at resonance is 6.7 meV at 75 kV/cm, which is ~ 95 % of the threshold. The resonance field for level 3 and 3' can be moved slightly closer to the operating field by further adjusting the well thicknesses of the wells in the extractor. Similarly, level 2 and state 2' are strongly coupled at threshold ($E_{2'} - E_2 = 14$ meV), with a splitting of 13.6 meV at resonance right above the threshold (81 kV/cm). Level 1 and state 1' are 12.6 meV apart at threshold, with a splitting of 7.8 meV at resonance at 85 kV/cm. Clearly, by lowering the exit barrier, there is resonant extraction from all the lower levels in the active region, that is, upon the relaxation from the upper lasing level, electrons are extracted from essentially a miniband. Recently [18], this miniband-type extraction was employed in 8.7-8.8 μm-emitting STA-DPR QCLs and high T_0 and T_1 values were obtained. This resonant extraction scheme has also been utilized in several QCL active-region designs, including Linear TA-QCL structures described previously, QCLs based on bound-to-continuum active-region design [19], and the so-called shallow-well 4.9 μm-emitting TA-QCLs [8], which will be discussed in the later section.

Other important parameters for the improved STA-QCLs at threshold include E_{54} of 100 meV, τ_{54} of 0.835 ps, τ_{4g} of 1.22 ps, τ_{3g} of 0.149 ps, and Δ_{inj} of 152.5 meV.

In the improved STA-DPR QCLs, the transition is basically vertical, given a z_{43} value of 15.3 Å, basically the same as in conventional and moderate TA-QCLs (15.6 Å); thus, much higher than for shallow-well TA-QCLs (10.6 Å). The figure of merit; that is, $z_{tr}^2 \cdot \tau_{up,g}$, where z_{tr} is the lasing-transition dipole matrix element, considering only inelastic scattering, is somewhat higher than for shallow-well TA-QCLs (*i.e.*, 268 Å^2 ps vs. 239 Å^2 ps). When considering interface roughness, the $\tau_{up,g}$ value of shallow-well TA-QCL devices will decrease much less than for STA-DPR devices, due to much lower CB offsets in the part of the active region where the lasing transition occurs (*i.e.*, ~ 500 meV vs. ~ 700 meV). However, the EL linewidth will be significantly narrower in STA-DPR devices, due to much less transition diagonality than in shallow-well TA-QCL devices. To that effect, when calculating the IFR factor, summed over all transition energies, affecting the EL linewidth [i.e., Eqn. (1) in [17]], we find it to be 59 % that for shallow-well TA-QCLs. In any event, while J_{th} (300K) for STA-DPR devices is expected to be ~ 7 % less than in conventional QCLs, we have found that for shallow-well TA-QCL devices J_{th} (300K) is ~ 25 % higher than conventional QCLs; thus, STA-DPR devices are expected to have J_{th} (300K) values ~ 26 % less than for shallow-well TA-QCL devices. The significantly lower J_{th} (300K) value is likely to compensate for lower V_{wpm} values in shallow-well TA-QCL devices that in DPR devices, due to lower Δ_{inj} values (i.e., ~124 meV vs. ~ 150 meV). Thus, the difference may well come down to the much lower thermal resistance R_{th} values, due to fewer interfaces per period and less strain, for STA-DPR devices compared to shallow-well TA-QCL devices. Then, the STA-DPR devices are projected to reach CW $\eta_{wp,max}$ values of at least 25 %, while the core-temperature rise will be less than half that of shallow-well TA-QCL devices (*i.e.*, ΔT_{act} ~ 20 K) at the

$\eta_{wp,max}$ point. Such devices are expected to be reliable at high (3- 4 W) CW powers, since, to date, the only lifetest data showing long-term QCL reliability [20] have been obtained from (low-power) QCLs with $\Delta T_{act} \sim 15$ K.

3.4 STA-SPR QCLs with Miniband Extraction

In addition to STA-DPR QCLs, we have also designed a step-tapered active-region (STA) QCL structure based on three-quantum-well active region of single-phonon-resonance (SPR) depopulation scheme. In this STA-SPR QCL structure, three distinct features are noted. First, by removing a quantum well in the active region, the energy difference between the lower laser level and the ground state of next injector, Δ_{inj}, is reduced from ~ 150 meV in DPR-based structures to ~ 125 meV at the operating field. Given a smaller Δ_{inj} in each stage, the required operating voltage is consequently lower compared to DPR-based devices. Second, the lasing transition is slightly diagonal, as the field of upper laser level peaks up in the first thin well, whereas the wavefunction of lower laser level is confined in the second wide well. Finally, unlike DPR-based structures where their operating fields are typically ~4 -5 meV away from the resonance between upper laser level and the ground state in the injector, the upper laser level and the ground state in STA-SPR QCLs are fairly strongly coupled (splitting > 10 meV), and the operating field is ~25 meV away from their splitting, providing a larger operating range than the DPR-based QCLs

The calculated conduction band diagram and squared modulus of relevant wavefunctions of STA-SPR QCLs, at the threshold field of 88 kV/cm, are shown in Fig. 3.13. The lasing transition occurs between the upper laser level, level 3, and the lower laser level, level 2. Similar to STA-DPR QCL structures, the barrier heights in the active region of STA-SPR QCLs are stepwise tapered, resulting in a large E_{43} value of 87 meV. Due to the large E_{43} as well as poor wavefunction coupling between two levels, the corresponding relaxation time from level 4 to level 3 due to LO phonon scattering, τ_{43}, is

as long as ~ 1 ps, which ensures the suppression of carrier leakages via level 4 into continuum. Due to the slightly diagonal lasing transition in STA-SPR QCLs, the dipole matrix element, z_{32}, is 11 A, somewhat smaller than the typical values (~ 15 A) in DPR-based devices. The carrier lifetime, on the other hand, is relatively longer in STA-SPR QCLs, as the calculated global "effective" upper-state lifetime $\tau_{up, g}$ is 1.81 ps. At threshold, the upper laser level and the ground state in the injector (denoted as "g" in the conduction-band diagram) are ~ 40 meV apart, much further away from their splitting of ~ 15 meV at resonance than in DPR-based QCLs. Moreover, similar to the optimized QCL structures based on a pocket-injector design reported by Bismuto et al. [21], where the maximum current corresponds to the alignment between the upper laser level and the first excited state in the injector, here the upper laser level is strongly coupled to the first excited state in the injector, which is expected to result in more efficient carrier injection into the upper laser level.

In addition, in contrast to classical SPR-QCL structures where the carriers are extracted only from level 1 via resonant tunneling upon the LO phonon scattering from level 2, in STA-SPR QCLs both level 2 and level 1 in the active region are very strongly coupled to extractor states 2' and 1' respectively, similar to the bound-to-continuum (BC) active-region design. This miniband-type depopulation scheme provides fast resonant carrier extraction from both lower levels after carriers relax from the upper laser level [18]. The splitting energies at resonance for levels 2 and 2', as well as 1 and 1', are ~ 10.5 meV and 7.5 meV, respectively. Both of their resonance fields are at 87.5 kV/cm, which basically coincide with the threshold field. This ensures that the carriers in the lower states of the active region can be rapidly extracted to the next stage throughout the entire dynamic

current range after the lasing threshold is achieved. It is clear that, by employing the resonant carrier extraction scheme, the issue of carrier bottleneck found in the typical three-quantum-well active region SPR-QCLs can be addressed.

In summary, due to large E_{43} and τ_{43}, the carrier leakage from upper laser level in the STA-SPR QCLs described in this section is virtually suppressed. They are expected to have more efficient carrier injection, and can be operated over a wider operating current range than typical DPR-QCL structures. With a reduced "defect voltage" Δ_{inj}, the STA-SPR QCLs operate at a relatively lower voltage than the DPR-QCLs, which reduces the required electrical input power at and above threshold and in turn enhances the maximum wallplug efficiency. The fast carrier extraction can also be achieved in this BC-like three-quantum-well active-region of STA-SPR QCLs via resonant carrier extraction from all the lower levels.
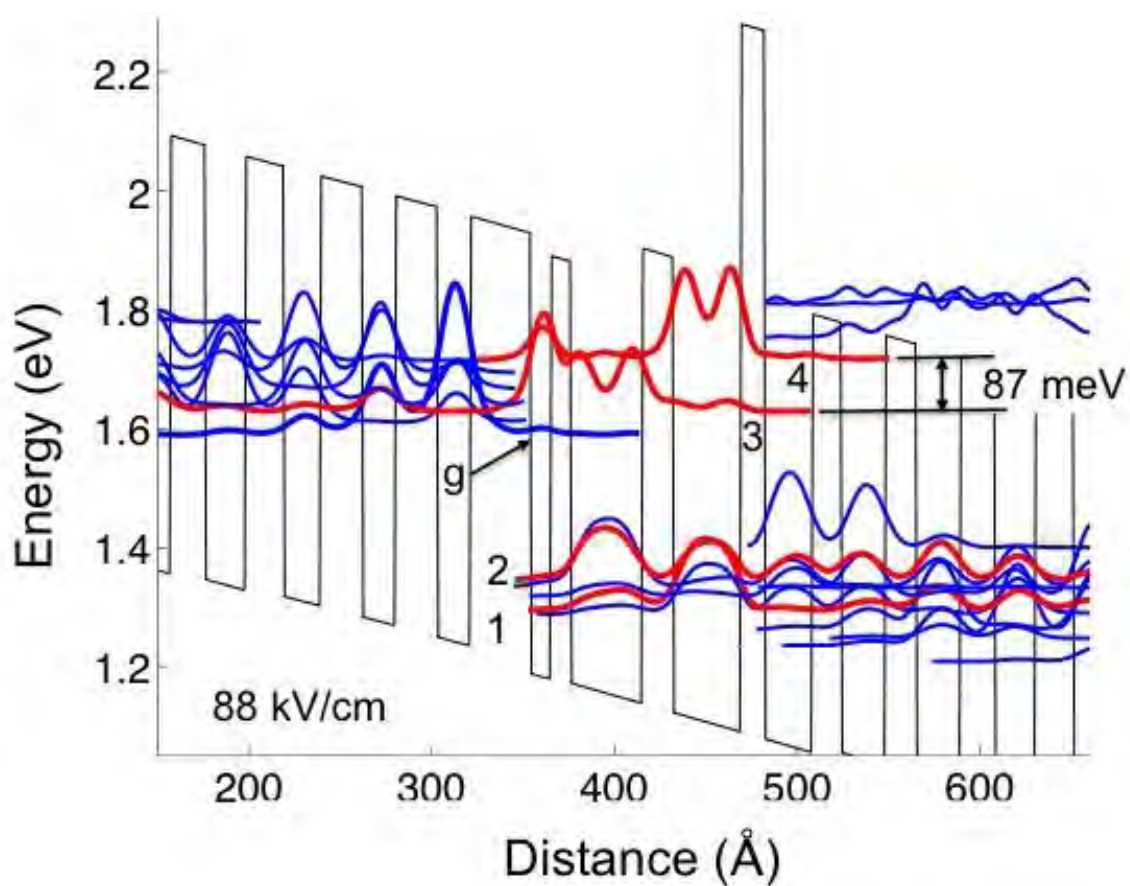
Fig. 3.13. Conduction-band diagram and squared modulus of key wavefunctions for STA-SPR QCLs emitting at $\lambda \sim 4.7$ µm.

For STA-SPR QCLs, the transition is diagonal ($z_{32} = 11$ Å) with a correspondingly long, inelastic-scattering upper-state lifetime: 1.82 ps. The figure of merit, only for inelastic scattering, is somewhat smaller than that for shallow-well TA-QCLs (i.e., 219 Å^2 ps vs. 239 Å^2 ps). However, when calculating the IFR factor, summed over all transition energies, affecting the EL linewidth [i.e., Eqn. (1) in [17]] we find it to be 76 % of that for the shallow-well TA-QCL devices. Thus, a smaller EL linewidth is likely to compensate for less $\tau_{up,g}$ reduction due to higher CB offset(s), where the transition occurs in the active region (*i.e..* ~ 700 meV vs ~ 500 meV). All in all, given similar Δ_{inj} values, the J_{th} (300K) value should basically be the same as for the moderately-doped shallow-well TA-QCL device (~ 1.3 kA/cm^2)[9]. Then, given that the V_{wpm} value will be similar to that for the shallow-well TA-QCLs and the thermal conductance G_{th} is likely to be about twice that of the shallow-well TA-QCLs, the devices are expected to reach RT CW $\eta_{wp,max}$ values of at least 25 %, with relatively low core-temperature rise (~ 20 K).

3.5 Shallow-Well Tapered-Active-Region (TA) QCLs

The-state-of-the-art mid-IR QCL devices are based on the so-called "shallow-well" tapered-active-region design emitting at $\sim$ 4.9 μm reported by Bai et al. [8]. The calculated conduction-band diagram and squared modulus of relevant wavefunctions of shallow-well TA-QCLs, at the threshold field of 87 kV/cm, are shown in Fig. 3.14. This shallow-well TA-QCL design is based on a three-quantum-well active region, where lattice-matched-to-InP materials $In_{0.53}Ga_{0.47}As$ and $Al_{0.48}In_{0.52}As$ are used to form the first shallower quantum well and shorter barrier, while the second and third quantum wells are deeper by using $In_{0.69}Ga_{0.31}As$ with taller barriers of $Al_{0.64}In_{0.36}As$. Furthermore, seven composite barriers, based on the combination of $Al_{0.64}In_{0.36}As$ with the large-conduction-band-offset material AlAs, are utilized from the exit barrier throughout the entire injector/extractor regions. Clearly, this shallow-well active-region design is essentially a TA-type QCL structure, where the barrier height is tapered from the first shorter barrier to the composite exit barrier. As a result, due to this asymmetry the shallow-well TA-QCLs share the same characteristics of other TA-type structures, having a large energy difference between the upper laser level and the higher-lying level right above it. At threshold field of 87 kV/cm, E_{43} is as large as 85 meV, similar to that in the STA-SPR QCLs, and the corresponding lifetime τ_{43} is calculated to be 0.72 ps. With a moderate injector doping level of $\sim$ 1.6 $\times$ 10^{10} cm^{-2}, the electro-optical characteristics of the fabricated shallow-well TA-QCL devices are less temperature dependent than conventional 4.5 – 5.0 μm-emitting QCLs, achieving high characteristic temperatures T_0 and T_1 of 244 K and 343 K, respectively, over the temperature rage of 80 to 380 K in pulsed mode, resulting from both suppression of carrier leakage and low waveguide loss

α_w. Furthermore, for 5 mm-long, 8 μm-wide devices in the buried-heterostructure (BH) geometry with high-reflectivity (HR) coating on the back facets, the maximum CW output power from a single facet reaches 5.1 W at room temperature, with a maximum CW wallplug efficiency of 21% [9], much higher than the typical value (~ 13%) for conventional QCLs.

Fig. 3.14. Conduction band diagram and squared modulus of key wavefunctions for shallow-well TA-QCLs emitting at $\lambda \sim 4.9$ μm.
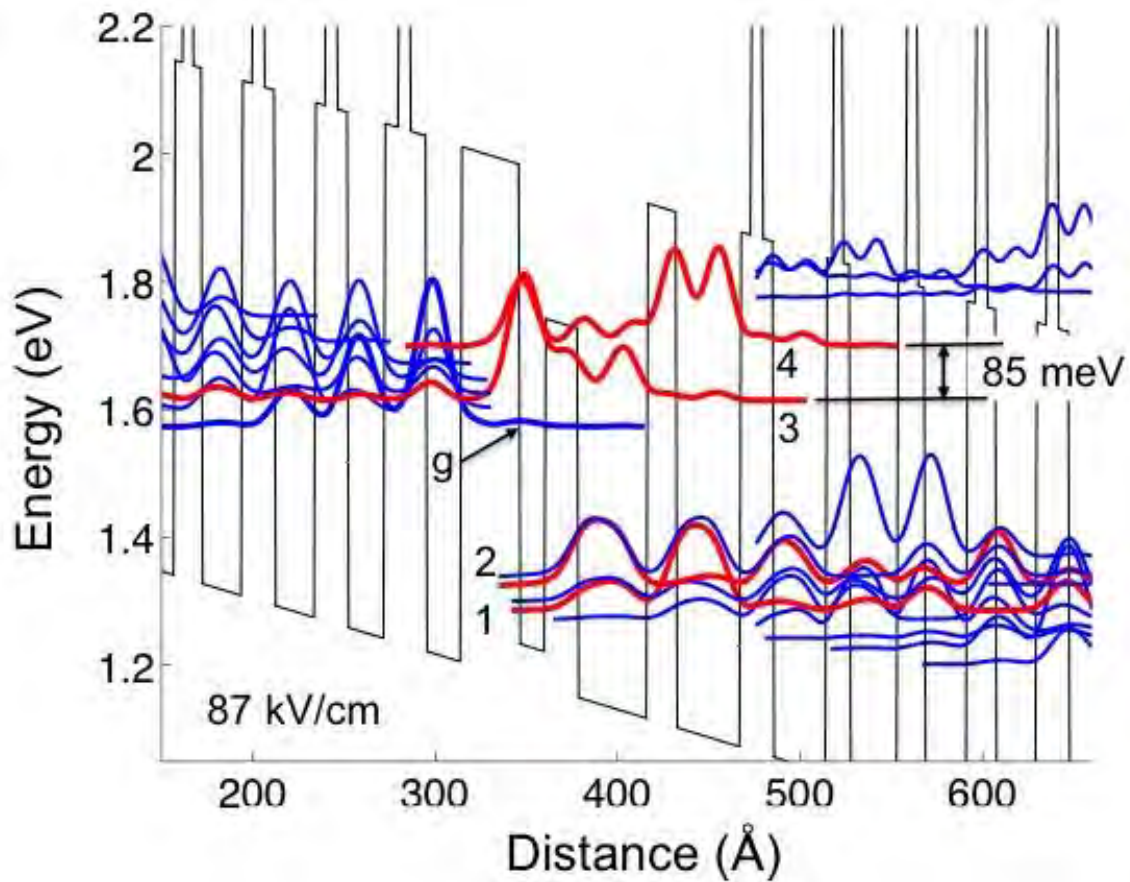
Despite these demonstrated record-high performances, the thermal resistance of shallow-well TA-QCL devices is much higher than that of conventional 5 mm-long BH QCLs with similar ridge width and submount material. It is shown [9] that, at 25 °C, the threshold current density in pulse mode $J_{th}^{pulse}(T_h)$ is

$$J_{th}^{pulse}(T_h) = \frac{I_{th}}{Area} = \frac{0.5 \times 10^{-3} kA}{(8 \times 10^{-4}) \times (0.5) cm^2}$$

$$= 1.25 \; {}^{kA}/_{cm^2}, \qquad (3.10)$$

where T_h is the heatsink temperature. Similarly, the threshold current in CW mode at 25 °C, $J_{th}^{CW}(T_l)$ is calculated to be

$$J_{th}^{CW}(T_l) = \frac{I_{th}}{Area} = \frac{0.54 \times 10^{-3} kA}{(8 \times 10^{-4}) \times (0.5) cm^2}$$

$$= 1.35 \; {}^{kA}/_{cm^2}, \qquad (3.11)$$

where T_l is the lattice temperature. Based on these values, the temperature rise in the active region of shallow-well QCLs T_h at threshold when operated in CW mode, $\Delta T_{act} = T_l - T_h$ can be evaluated as follows:

$$J_{th}^{CW}(T_l) = J_{th}^{pulse}(T_h) \times \exp\left(\frac{\Delta T_{act}}{T_0}\right), \qquad (3.12)$$

$$\Delta T_{act}$$

$$= (244 \; K) \times \ln\left(\frac{1.35}{1.25}\right) \sim 19 \; K. \qquad (3.13)$$

At threshold, the output optical power $P_{optical}$ is zero. The thermal resistance of the device, R_{th}, can therefore derived as follows:

$$R_{th}$$

$$= \frac{\Delta T_{act}}{(P_{electrical} - P_{optical})} \sim \frac{19 \; K}{P_{electrical}} \sim \frac{19K}{0.54 \times 12 \; W} \sim 3\frac{K}{W} \qquad (3.14)$$

This value is a rough estimate. By fitting to the CW *L-I* curve in [9] R_{th} = 3.3 K/W was obtained. Using the same procedure, the thermal resistance of conventional 5 mm-long BH QCLs with similar ridge width and submount material is ~ 1.5 K/W [22]. Therefore, the thermal resistance of shallow-well TA-QCLs is about twice higher than that for conventional BH QCLs. The high thermal resistance of shallow-well TA-QCLs is due primarily to more interfaces of dissimilar materials per stage [23]. By incorporating seven AlAs barriers throughout the injector/extractor regions, the total number of interfaces per stage for shallow-well TA-QCLs is 34, much greater than that (22) for conventional QCLs. In addition, Lee et al. [24] performed thermal analysis of short-wavelength InGaAs/AlInAs QCLs, and their results show that the thermal conductance along the growth direction depends highly on the material quality, which is strongly affected by the interfaces of strained layers used in the active region, and QCLs containing highly strained layers, such as AlAs, therefore are likely to have high thermal resistance due to poor interface quality. Due to device self-heating caused by high thermal resistance, the shallow-well TA-QCLs are by no means reliable for long-term operation in CW mode.

To lower the thermal resistance of shallow-well TA-QCLs, the number of AlAs barriers used in the injector regions have to be significantly reduced. We thus simulated the same shallow-well TA-QCL structure after removing six AlAs barriers in the injector/extractor region. The calculated conduction-band diagram and relevant wavefunctions are shown in Fig. 3.15. After removing six AlAs barriers, the energies of all the states in the injectors regions are lowered, resulting in a much higher electric field required to reach lasing threshold. At threshold field of 103.5 kV/cm, E_{43} is reduced from 85 meV to only 69 meV. As a result, without the aid of AlAs barriers in the injector/extractor regions,

both increased carrier leakage and lowered T_0 and T_1 values are expected in the shallow-well TA-QCLs. Moreover, level 4 in the active region becomes weakly coupled to states in the upper Γ miniband after the removal of AlAs. This coupling further facilitates the carrier escape from level 4 to the upper Γ miniband. Clearly, lower thermal resistance of shallow-well TA-QCLs can only be achieved at the expense of increased carrier leakage. The seven AlAs barriers are thus absolutely necessary in the shallow-well TA-QCLs in order to suppress carrier leakage.
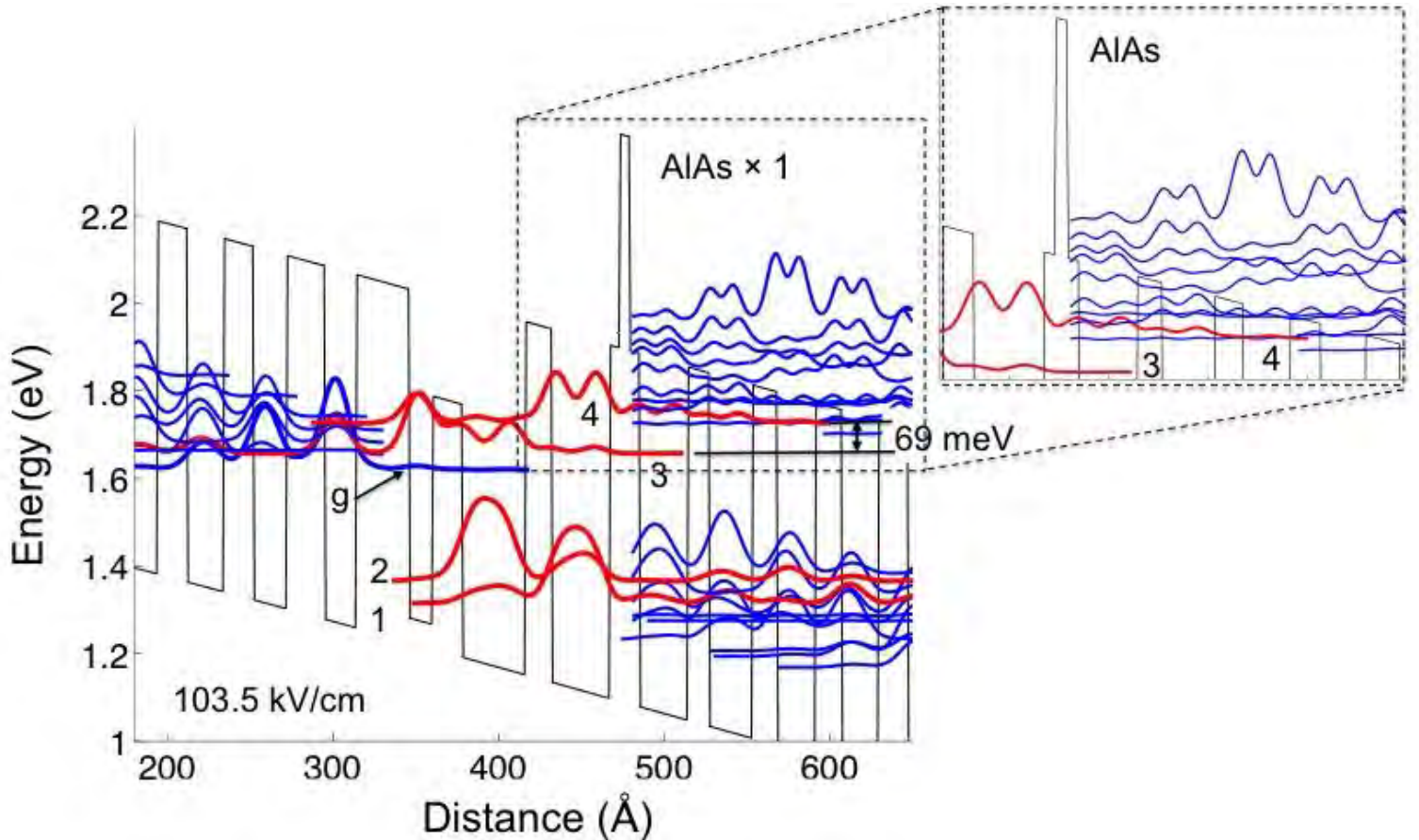
Fig. 3.15. Conduction band diagram and squared modulus of key wavefunctions for shallow-well QCLs with only one AlAs barrier.

Table 3.2 summarizes the operating field, $\tau_{up,\,g}$, z_{43} (or z_{32}), IFR, $z^2 \times \tau_{up,\,g}$, E_{54} (or E_{43}), and τ_{54} (or τ_{43}) for STA-DPR, STA-SPR, and shallow-well TA-QCLs. As can be seen, all the designs show comparably high E_{54} (or E_{43}) and τ_{54} (or τ_{43}), and hence suppression of carrier leakage, due to similar TA-type active region. The ratio of the product of z^2 and $\tau_{up,\,g}$ to the IFR value for the STA-SPR structure, representing the figure-of-merit for gain cross-section without considering the effect of IFR-mediated carrier leakage on lifetimes, is ~20% higher than that for the shallow-well TA-QCLs. The threshold current density J_{th} for STA-SPR is therefore expected to be slightly lower than that for the shallow-well TA-QCLs. The STA-DPR has the highest figure-of-merit for gain cross-section due to the nature of vertical lasing transition. Moreover, in both STA-DPR and STA-SPR QCL structures, only one high strained layer ($Al_{0.93}In_{0.07}As$) is used in the active region. The values of strain per stage for both STA structures are close to that for conventional QCLs. The effect of high strained layers on the thermal resistance is thus minimized. More importantly, the total number of interfaces in both STA structures is much less than that in the shallow-well TA-QCLs, which ensures much lower thermal resistance and in turn reduced temperature rise in the active region under CW mode. As a result, although similar J_{th} values are expected, both STA-DPR and STA-SPR structures are more reliable for long-term operation at high CW power (> 0.5 W) than the shallow-well TA-QCLs due to less device heating.

	$\tau_{up,g}$	z_{54} (or z_{43})	$z^2 \times \tau_{up,g}$	IFR	E_{54} (or E_{43})	τ_{54} (or τ_{43})
STA-DPR	1.15	15.3	269.2	0.0137	100	0.84
STA-SPR	1.81	10.99	218.6	0.0177	87	0.99
Shallow-well	2.14	10.58	239.5	0.0233	85	0.72

Table 3.2 Summary of $\tau_{up,\,g}$, z_{54} (or z_{43}), $z^2 \times \tau_{up,\,g}$, IFR, E_{54} (or E_{43}), and τ_{54} (or τ_{43}) in STA-DPR, STA-SPR, and shallow-well TA-QCL structures.

3.6 Projection of CW Maximum Wallplug Efficiency for STA-QCLs

The temperature rise in the active region, and the maximum wallplug efficiency of QCL devices, $\eta_{wp, max}$, under CW operation at room temperature can be estimated as follows:

$$\Delta T_{act} = T_{lattice} - T_{heatsink} = R_{th} P_{electrical}(1 - \eta_{wp,max}), \qquad (3.15)$$

$$\eta_{wp,max} \approx \eta_s \eta_{d,300K} \exp\left(-\frac{\Delta T_{act}}{T_1}\right)\left[1 - \frac{1}{3}\exp\left(\frac{\Delta T_{act}}{T_0}\right)\right]\left(\frac{h\nu}{qV_{wp,max}}\right), \qquad (3.16)$$

where η_s is the droop in pulsed L-I curve at the $\eta_{wp, max}$ point, $h\nu$ is the photon energy, q is the electronic charge, and $P_{electrical}$ and $V_{wp,max}$ are the electrical input power and operating voltage at the $\eta_{wp, max}$ point. To estimate the $\eta_{wp, max}$ values for STA-QCL in CW mode at room temperature, we first assume the thermal resistance R_{th} to be close to that of 8 μm-wide conventional QCLs ($\sim$ 1.5 K/W). The T_0 and T_1 values for STA-QCLs are taken from the experimental data for moderate TA-QCLs (T_0 = 231 K, T_1 is 797 K). With $\eta_s \sim$ 0.92 and $V_{wp, max}$ same as that for shallow-well QCLs, the estimated ΔT_{act} is $\sim$ 21 K for STA-QCLs. The ΔT_{act} value for shallow-well QCLs is also derived to be $\sim$ 50 K using R_{th} $\sim$ 3.3 K/W and the measured $\eta_{wp, max}$ of 21 %. Apparently, by using much less high strained layers in the active region, the device self-heating is significantly reduced as the temperature rise in the active region of STA-QCLs is much lower that that in shallow-well QCLs. Finally, the projected single-facet $\eta_{wp, max}$ for STA-QCLs in CW mode at room temperature is $\geq$ 25 %, close to the theoretically predicted limit for 4.8 μm-emitting QCLs.

Further increases in wallplug efficiency for 4.5- 5.0 μm-emitting QCLs can be achieved [25] by either increasing the internal differential efficiency η_i^d from its current best value of 70 % to theoretical limits in the 85- 90 % range, and/or by using designs [21] for

significantly lowering the V_{wpm} value. With a reduction in IFR-mediated carrier leakage from injector states may be the means for raising the η_i^d value to the 85- 90 % range, just as already achieved for 8.7- 8.8 μm-emitting QCLs [18]. Then, the maximum, single-facet pulsed wallplug efficiency would reach values of ~ 33 %, which, in turn, would result in CW $\eta_{wp,max}$ values in excess of 31 %. As for significantly reducing the V_{wpm} value, it has been theoretically and experimentally shown that can be done by using the "pocket injector" concept [21]. That is, carrier injection into the upper laser level occurring form the first excited state of the injector region, by taking advantage of the fact that, since electrons are hot in the injector miniband, that state is equally populated as the injector ground state. Then, again single-facet, CW wallplug efficiencies in excess of 30 % may be possible. Ultimately, by increasing both the η_i^d value to theoretical limits and decreasing the V_{wpm} value via pocket injector, one may be able to achieve room-temperature CW $\eta_{wp,max}$ values as high as 37 %.

3.7 Conclusion

Step-tapered active-region (STA) QCLs emitting at ~ 4.8 μm for complete suppression of carrier leakage are proposed based on both DPR and SPR-based structures. The stepwise tapering of barrier heights in the active region not only significantly increases the E_{54} (or E_{43}) value to ~ 100 meV and 85 meV for STA-DPR and STA-SPR QCLs, respectively, but the reduction in E_{54} value (or E_{43}) due to the Stark shift is also minimized. The significantly large E_{54} (or E_{43}) in STA-QCL structures results in the complete suppression of carrier leakage. In comparison with the state-of-the-art shallow-well TA-QCLs, the proposed STA-QCLs are expected to have similar threshold current densities. However, in STA-QCL structures, since only one high-strained layer is used in the active region, the effect of high-strained layers on the thermal resistance is minimized. More importantly, the total number of interfaces in the active region of STA-QCLs is much less than that in shallow-well TA-QCLs, which leads to a much lower thermal resistance. The projected temperature rise in the active region in STA-QCLs is calculated to be only about half of that for shallow-well TA-QCLs. Due to less device self-heating, the projected single-facet, CW maximum walllplug efficiency of STA-QCLs is ≥ 25% at room temperature, close to the predicted limit for mid-infrared 4.8 μm–emitting QCLs, which therefore makes the proposed STA-QCLs promising for long-term, reliable operation at high (≥ 0.5 W) CW powers.

Reference

[1] A. Evans, J. S. Yu, S. Slivken, and M. Razeghi. "Continuous-wave operation of $\lambda \sim$ 4.8 μm quantum-cascade lasers at room temperature", *Appl. Phys. Lett.*, **85**, 2166 (2004).

[2] D. Botez, S. Kumar, J. C. Shin, L. J. Mawst, I. Vurgaftman, and J. R. Meyer. "Temperature dependence of the key electro-optical characteristics for midinfrared emitting quantum cascade lasers", *Appl. Phys. Lett.*, **97**, 071101 (2010).

[3] Y. Bai, S. Slivken, S. R. Darvish, and M. Razeghi. "Room temperature continuous wave operation of quantum cascade lasers with 12.5% wall plug efficiency", *Appl. Phys. Lett.*, **93**, 021103 (2008).

[4] D. Botez, J. C. Shin, J. D. Kirch, C.-C. Chang, L. J. Mawst, and T. Earles. "Multidimensional conduction-band engineering for maximizing the continuous-wave (CW) wallplug efficiencies of mid-infrared quantum cascade lasers", *IEEE J. Sel. Top. Quantum Electron.* **19(4)**, 1200312 (2013).

[5] J. C. Shin, L. J. Mawst, and D. Botez. "Crystal growth via metal-organic vapor phase epitaxy of quantum-cascade-laser structures composed of multiple alloy compositions", *J. Cryst. Growth*, **357**, 15-19 (2012).

[6] J. C. Shin, M. D'Souza, Z. Liu, J. Kirch, L. J. Mawst, D. Botez, I. Vurgaftman, and J. R. Meyer. "Highly temperature insensitive, deep-well 4.8 μm emitting quantum cascade semiconductor lasers", *Appl. Phys. Lett.*, **94**, 201103 (2009).

[7] J. D. Kirch, J. C. Shin. C.-C. Chang, L. J. Mawst, D. Botez, and T. Earles. "Tapered active-region quantum cascade lasers ($\lambda = 4.8$ μm) for virtual suppression of carrier-leakage currents", *Electron. Lett.*, **48**, 234-235 (2012).

[8] Y. Bai, N. Bandyopadhyay, S. Tsao, E. Selcuk, S. Slivken, and M. Razeghi. "Highly temperature insensitive quantum cascade lasers", *Appl. Phys. Lett.*, **97**, 251104 (2010).

[9] Y. Bai, N. Bandyopadhyay, S. Tsao, S. Slivken, and M. Razeghi. "Room temperature quantum cascade lasers with 27% wall plug efficiency", *Appl. Phys. Lett.*, **98**, 181102 (2011).

[10] M. P. Semtsiv, Y. Flores, M. Chashnikova, G. Monastyrsky, and W. T. Masselink. "Low-threshold intersubband laser based on interface-scattering-rate engineering", *Appl. Phys. Lett.*, **100**, 163502 (2012).

[11] A. Evans, S. R. Darvish, S. Slivken, J. Nguyen, Y. Bai, and M. Razeghi. "Buried heterostructure quantum cascade lasers with high continuous-wave wall plug efficiency", *Appl. Phys. Lett.*, **91**, 071101 (2007).

[12] J. Faist. "Wallplug efficiency of quantum cascade lasers: Critical parameters and fundamental limits", *Appl. Phys. Lett.*, **90**, 253512 (2007).

[13] J. C. Shin, L. J. Mawst, D. Botez, I Vurgaftman, and J. R. Meyer. "Ultra-low temperature sensitive deep-well quantum cascade lasers ($\lambda = 4.8$ μm) via uptapering conduction band edge of injector regions", *Electron. Lett.*, **45**, 741-743 (2012).

[14] D. Botez, J. C. Shin, J. D. Kirch, C.-C. Chang, L. J. Mawst, and T. Earles. "Tapered active-region, mid-infrared quantum cascade lasers for complete suppression of carrier-leakage currents", *Proc. SPIE*, **8277**, 82770W-1-82770W-9 (2012).

[15] A. Lyakh, R. Maulini, A. Tsekoun, R. Go, C. Pflügl, L. Diehl, Q. J. Wang, F. Capasso, and C. Kumar N. Patel. " 3 W continuous-wave room temperature single-facet emission from quantum cascade lasers based on nonresonant extraction design approach", *Appl. Phys. Lett.*, **95**, 141113 (2009).

[16] P. Offermans, P. M. Koenraad, J. H. Wolter, M. Beck, T. Aellen, and J. Faist. "Digital allow interface grading of an InAlAs/InGaAs quantum cascade laser structure studied by cross-sectional scanning tunneling microscopy", *Appl. Phys. Lett.*, **83**, 4131 (2003).

[17] A. Wittmann, Y. Bonetti, J. Faist, E. Gini, and M. Giovannini. "Intersubband linewidths in quantum cascade laser design", *Appl. Phys. Lett.*, **93**, 141103 (2008).

[18] J. D. Kirch, C.-C. Chang, C. Boyle, L. J. Mawst, D. Lindberg III, T. Earles, and D. Botez. "Highly temperature insensitive, low threshold-current density (λ = 8.7- 8.8 μm) quantum cascade lasers", *Appl. Phys. Lett.*, **106**, 151106 (2015).

[19] J. Faist, M. Beck, T. Aellen, and E. Gini. "Quantum cascade lasers based on a bound-to-continuum transition", *Appl. Phys. Lett.*, **78**, 147 (2001).

[20] F. Xie, C. Caneau, H. P. LeBlanc, N. J. Visovsky, S. C. Chaparala, O. D. Deichmann, L. C. Hughes, C. Zah, D. P. Caffey, and T. Day. "Room temperature CW operation of short wavelength quantum cascade lasers made of strain balanced $Ga_xIn_{1-x}As/Al_yIn_{1-x}As$ material on InP substrates", *IEEE J. Sel. Top. Quantum Electron.*, **17**, 1445-1452 (2011).

[21] A. Bismuto, R. Terazzi, B. Hinkov, M. Beck, and J. Faist. "Fully automatized quantum cascade laser design by generic optimization", *Appl. Phys. Lett.*, **101**, 021103 (2012).

[22] Y. Bai, B. Gokden, S. Slivken, S. R. Darvish, S. A. Pour, and M. Razeghi. "Mid-infrared quantum cascade lasers with high wall plug efficiency", *Proc. SPIE*, **7222**, 72220O-1-72220O-10 (2009).

[23] M. S. Vitiello, T. Gresch, A. Lops, V. Spagnolo, G. Scamarcio, N. Hoyler, M. Giovannini, and J. Faist. "Influence of InAs, AlAs δ layers on the optical, electronic, and thermal characteristics of strain-compensated GaInAs/AlInAs quantum cascade lasers", *Appl. Phys. Lett.*, **91**, 161111 (2007).

[24] H. K. Lee and J. S. Yu. "Thermal analysis of short wavelength InGaAs/InAlAs quantum cascade lasers", *Solid-State Electron.*, **54**, 769-776 (2010).

[25] D. Botez, C.-C. Chang, and L. J. Mawst. "Temperature sensitivity of the electro-optical characteristics for mid-infrared ($\lambda = 3-16\,\mu m$) –emitting quantum cascade lasers", *J. Phys. D: Appl. Phys.*, submitted (2015).

CHAPTER FOUR

BURIED-HETEROSTRUCTURE QUANTUM CASCADE LASERS FABRICATED BY NON-SELECTIVE REGROWTH AND CHEMICAL POLISHING

4.1 Introduction

Mid-infrared (IR) quantum cascade lasers (QCLs), since their first demonstration in 1994, have drawn a great deal of interest for their various applications in trace-gas sensing and monitoring, infrared countermeasures, free-space communications, and spectroscopy. The first QCLs ($\lambda = 4.2$ μm) demonstrated by Faist et al. [1] were based on the so-called "diagonal transition" in three-quantum-well active region design, where the modulus squared of electron wavefunctions in the upper (level 3) and lower (level 2) laser levels have maximums in adjacent quantum wells. These QCL devices operated only in pulsed operation at cryogenic temperatures. The maximum output power of these early devices was ~ 9 mW at $T = 10$ K, and the highest operating temperature is 90 K. A year later, continuous-wave (CW) operation of QCLs was demonstrated for the first time at $\lambda = 4.6$ μm above liquid-nitrogen temperature [2]. These devices emitted output power of 15 mW at $T = 50$ K and 2 mW at $T = 80$ K in CW operation, and can be operated up to $T = 200$ K in the pulsed mode. The improvement in device performance of these QCLs resulted from better design of their active regions. First, the laser transition was more vertical, that is, the modulus squared of electron wavefunctions in the upper and lower laser levels peak up in the same quantum well. Due to better spatial overlap of electron wavefunctions, not only the oscillator strength were higher compared to devices based on

diagonal transition, but the laser transition was also less sensitive to the interface roughness from the imperfection of crystal growth. Furthermore, the backfilling energy Δ_{inj} in these devices, the energy difference between the lower laser level and the ground state of the injector in the next stage, was increased to ~ 100 meV. With larger Δ_{inj}, the electron backfilling was significantly suppressed, the threshold current was reduced, and hence the lasers could be operated at higher temperatures.

However, it was not until 2002 [3] that the first CW operation of QCLs at room temperature was demonstrated. The reason for that is, in addition to better active region designs [4], the thermal resistance of QCL devices needs to be minimized in order to achieve room-temperature CW operation. The active core of QCLs comprises multiple layers of ternary III-V semiconductor materials, for example, InGaAs and AlInAs in InP-based QCLs. These materials have ~ 15 times lower thermal conductance compared to that of binary semiconductor materials such as InP. Therefore, when operated at high duty cycles, the active-region temperature of QCLs is much higher the heatsink temperature. This self-heating of the laser core in turn leads to significant thermal stress to the QCL devices, and eventually catastrophic device failure before they reach CW operation at room temperature.

For better heat removal in the growth direction, Faist et al. [5] first replaced the top AlInAs cladding layer with InP by two-step molecular-beam epitaxy (MBE) growth method, and these InP cladded devices (λ = 5.2 μm) can operate up to T = 320 K in pulsed operation, and T = 140 K under CW mode. In 1999, first epilayer-side mounting of QCL devices ((λ = 8 μm) were reported by Gmachl et al. [6]. To reduce the amount of dissipated heat and also ensure uniform bonding over the entire device area, devices of

shorter cavity length (~ 1.5 mm) and narrower width (≤ 10 μm) were fabricated, and mounted epi-side down on the copper heatsink, with high reflectivity (HR) coatings (SiO_2/Au) deposited on their back facets to reduce the mirror loss. The temperature performance of these epi-side down mounted QCLs are superior to substrate-side bonded devices, due to more efficient heat dissipation through the heatsink. The maximum CW operating temperature is raised to 175 K. Other device performance, including threshold current, output power, and slope efficiency, are all greatly improved for epi-side down mounted devices. The calculated temperature profiles along the vertical direction in the center of the ridge indeed show much less temperature gradient for epi-side down mounted devices. In 2001, Hofstetter et al. [7] demonstrated room-temperature operation of 3mm-long, junction-up mounted QCLs at a longer wavelength (λ = 9.3 μm). Furthermore, by mounting the device junction-down on the copper heatsink, shorter devices (1.5 mm) with high HR coating on the back facets can operate up to T = 246 K in CW operation.

In these lasers, the sidewall of laser ridges are covered by dielectric layers such as Si_3N_4 or SiO_2 for current confinement. These dielectric layers, however, not only increase the waveguide loss due to scattering, but also prevent efficient heat extraction in the lateral direction. To improve lateral heat dissipation, Beck et al. [8] reported the first buried heterostructure (BH) QCLs. The fabrication of BH-QCL devices involves the regrowth of 3 μm-thick undoped InP over the entire laser structures by MBE, after the ridge formation by wet chemical etching and *in-situ* surface cleaning for removing native oxides. The regrown InP on top of cladding was then wet etched for current injection. These BH-QCL devices show much lower thresholds and higher slop efficiency

compared to lasers without the regrown InP. To prevent the InP regrowth on top of the cladding, In 2001, BH-QCLs were fabricated by the same group using selective regrowth of 3 μm-undoped InP on the laser ridge sidewalls by metal-organic chemical vapor deposition (MOCVD) using SiO_2 hardmask after wet etching [9]. Compared to reference lasers, the BH-QCL devices exhibit five-fold improvement in maximum average output power, and could operate at room temperature at a duty cycle of up to 17%. Finally, Beck et al. [10] demonstrated first CW operation of QCL devices at room temperature in 2002. These QCLs are based on four-quantum-well active region with double-phonon resonance (DPR) depopulation, for better carrier extraction from the lower laser level. After MBE growth of QC structures, the material was first processed into narrow-ridge waveguides (12 μm) in the BH geometry, and then cleaved into 750-μm long laser devices. The fabricated BH-QCLs were mounted epi-side down to diamond submounts with HR coating (ZnSe/PbTe) on both facets. These lasers emitted CW output power of 17 mW at $T = 292$ K, and 3 mW up to 312 K at $\lambda = 9.1$ μm.

Based on BH device geometry, the CW performance of QCLs at room temperature has been significantly improved over the past years. Evans et al. [11] in 2004 demonstrated CW output power of 446 mW at 293 K and highest CW operating temperature of 333 K, from 3mm-long, 9 μm-wide epi-side up mounted devices at $\lambda = 6$ μm, with 5 μm-thick electroplated Au heat-spreading layer on top and HR coating (Y_2O_3/Ti/Au) on the back facets. In 2007, Evans et al. [12] further reported 3 mm-long, 6 μm-wide, BH-QCLs emitting at 4.7 μm with maximum CW power of 675 mW at 298 K and wallplug efficiency of 9.3%, based on strain-compensated $In_{0.669}Ga_{0.331}As$/$Al_{0.638}In_{0.362}As$ active region. Based on the same active region but increasing the injector doping level by 35%

and using wider ridges (9.8 μm) aiming at high output power, Bai et al. [13] (2008) demonstrated watt-level CW output power (1.3 W) from 4.6 μm-emitting BH-QCLs at room temperature. In the same year, Lyakh et al. [14] reported 1.6 W CW output power at 300 K from uncoated BH-QCLs at $\lambda = 4.6$ μm by optimizing the active region and waveguide structure. In 2009, Lyakh et al. [15] reported 3W CW output power at room temperature from 4.6 μm-emitting 40-stage BH-QCLs using non-resonant-extraction (NRE) active region design. More recently, state-of-the-art QCLs were reported in 2011 by Bai et al. [16], where the maximum output power reaches 5.1 W at room temperature, with wallplug efficiency of 21% in CW operation, based on their shallow-well tapered active-region (TA) design.

4.2 BH-QCLs Fabricated by Selective Regrowth of Fe:InP

As seen in section 4.1, the fabrication of BH-QCLs usually involves the selective regrowth of semi-insulating, iron-doped (Fe:InP) InP. The fabrication process of BH-QCLs using selective regrowth of InP is illustrated in Fig. 4.1. After the ridge formation by either plasma dry etching or chemical wet etching (Fig. 4.1(a)), Fe:InP is selectively regrown on the sidewalls of etched ridges, as shown in Fig. 4.1(b). Once the regrowth is completed, the original dielectric hardmask is removed, and a new dielectric layer (either SiN_x or SiO_2) is deposited for current confinement (Fig. 4.1(c)). A contact window stripe is then opened in the dielectric layer (Fig. 4.1(d)) for current injection by reactive-ion etching, followed metal evaporation (Fig. 4.1(e)) to finish the front-side processing.
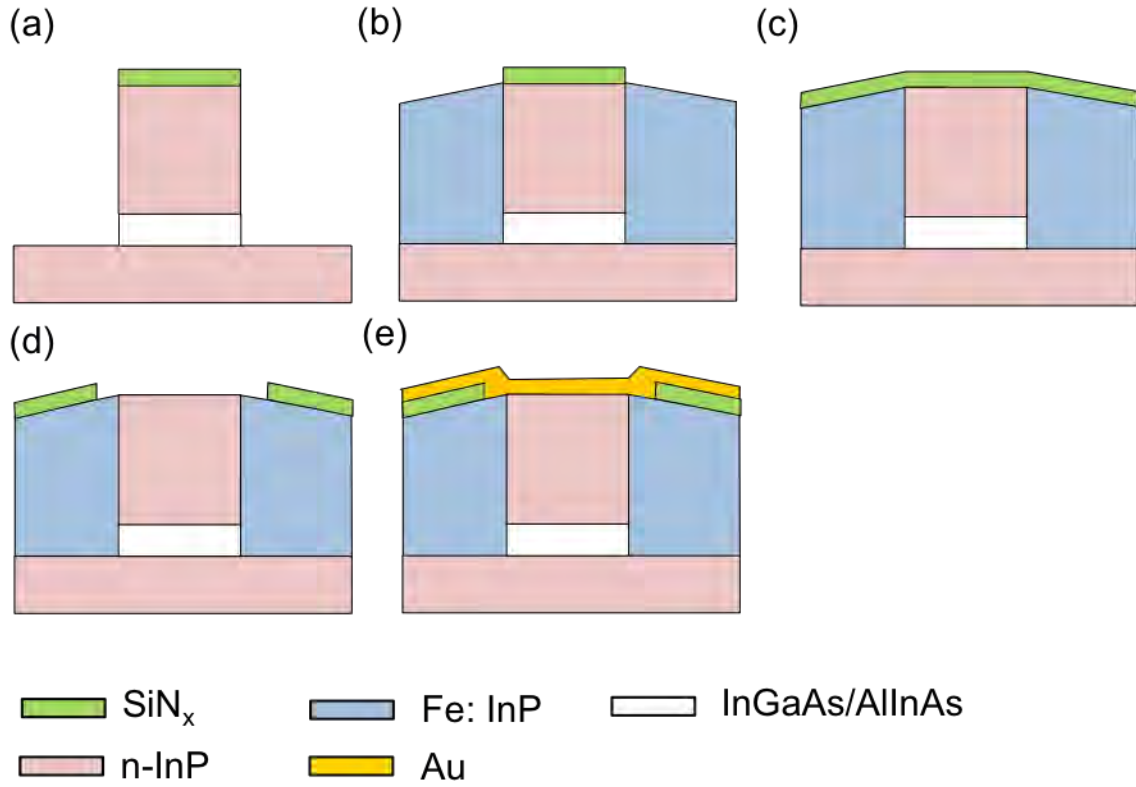
Fig. 4.1. Schematic of the main fabrication steps for BH-QCLs based on selective regrowth of Fe:InP: (a) laser ridge formation by plasma dry etching or chemical wet etching; (b) selective regrowth of Fe:InP without removing the dielectric hardmask (SiN$_x$); (c) deposition of insulating dielectric layers (SiN$_x$) for current confinement; (d) reactive-ion etching (RIE) of SiN$_x$ for current injection; and (e) metal evaporation.

Unfortunately, the selective regrowth of Fe:InP described in this process, however, is not a trivial step. The lateral regrowth step using MOCVD was previously studied by Cheng et al. [17]. Their results showed that, in addition to typical growth conditions, the characteristics of the regrown InP strongly depend on the sidewall profile of the etched ridges, as well as on the physical dimensions of the dielectric mask, including its thickness and overhang width (Fig. 4.2). All of these parameters need to be optimized to ensure smooth regrowth morphology around the etched ridges, and planar, uniform regrown layers away from the ridges.
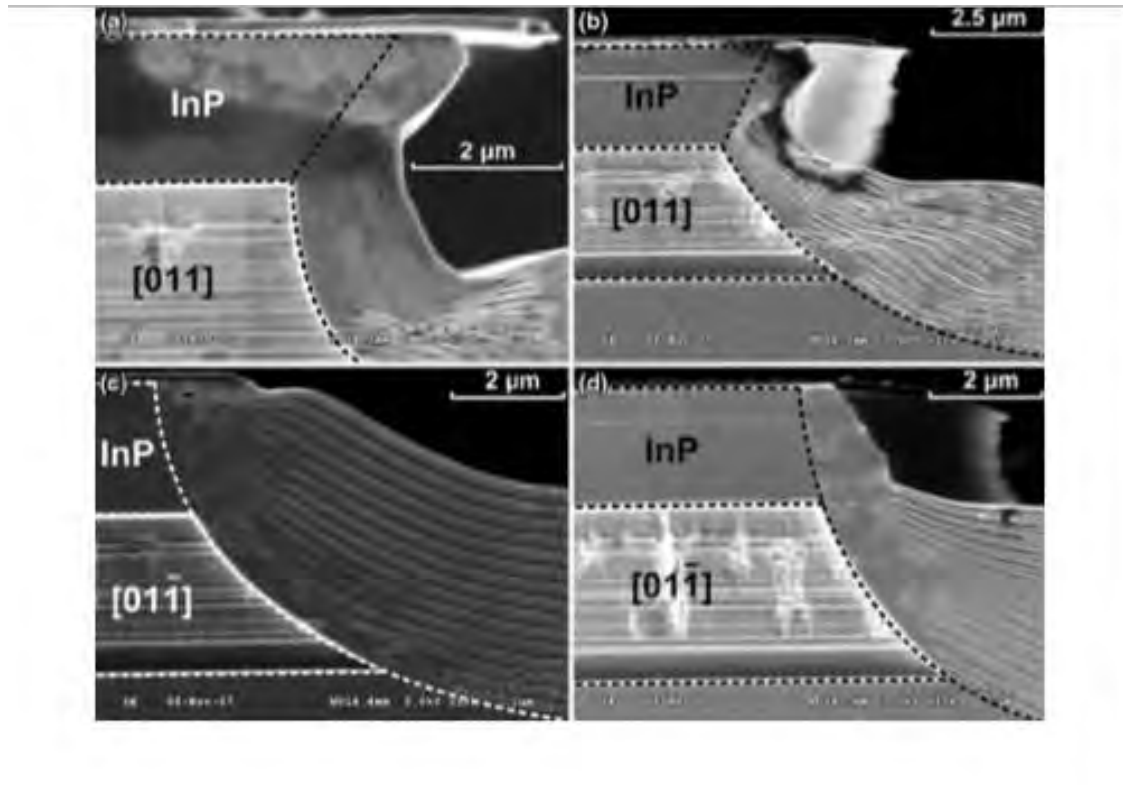
Fig. 4.2. Scanning electron microscopy (SEM) images of selective regrowth of Fe:InP (a) along [011] direction with 2 μm SiO_2 overhang; (b) along [011] direction with 4 μm SiO_2 overhang; (c) along [01$\bar{1}$] direction with 2 μm SiO_2 overhang; and (d) along [01$\bar{1}$] direction with 4 μm SiO_2 overhang.

Here, we present a novel fabrication method for the realization of BH-QCLs using non-selective regrowth of Fe:InP via MOCVD, followed by planarization using chemical polishing (CP) [18]. Through the use of this non-selective regrowth approach, the effect of the dielectric mask on the regrown-InP morphology (observed for selective regrowth) can be completely removed. It is also found that InP can be uniformly regrown both on the smooth sidewalls of laser ridges, formed by wet-chemical etching, and in narrow trenches of nearly vertical sidewalls, formed by plasma etching. Furthermore, after the regrowth, the CP step uniformly polishes down the excess regrown InP material, and hence the entire device surface area is planarized, which is particularly crucial for epi-side down laser-chip mounting.

4.3 Fabrication Process

The details of the fabrication process for our BH-QCLs are summarized in Fig. 4.3. A 30-stage, 4.6 μm-emitting QCL structure was grown using MOCVD based on the active-region design published by Evans et al.. Atop, a 100 nm-thick InGaAs layer was grown to serve as the etch-stop layer in the CP step. Then, a 500 nm-thick SiN_x film was deposited by plasma-enhanced chemical vapor deposition (PECVD), and 8 □m-wide stripes were defined by photolithography along the [011] orientation and transferred into SiN_x using CF_4-based reactive-ion etching (RIE). Using SiN_x as a hardmask, the grown InGaAs layer was first selectively wet etched using a H_3PO_4/H_2O_2 solution, followed by inductively-coupled-plasma (ICP) etching of both the InP upper cladding layer and InGaAs/AlInAs laser-core material. To alleviate the plasma damage to the etched sidewalls and also create a smoother sidewall profile favorable for InP regrowth, the sample was dipped in a

hydrogen bromide (HBr) solution after ICP etching. The etched ridges were ~ 8-9 μm high, with an ~ 7 μm width at the core region (Fig. 4.3(a)). Once the ridge etch was completed, Fe:InP was non-selectively regrown by MOCVD for current blocking in the lateral direction and better heat removal (Fig. 4.3(b)). Next, a CP step using acetic acid/HCl solution was employed to polish down the excess Fe:InP grown atop the ridges, which was stopped by the InGaAs layer (Fig. 4.3(c)). After CP, the InGaAs layer was removed and a 150 nm-thick PECVD SiN_x film was deposited for further current confinement (Fig. 4.3(d)). A 4 μm-wide contact-window stripe was opened in SiN_x for current injection (Fig. 4.3(e)). After evaporation of Ti/Au for the top contact (Fig. 4.3(f)), a 5 μm-thick Au layer was electroplated to further improve the heat dissipation of the devices. Fabricated structures were cleaved into 3 mm-long bars, after substrate thinning and backside metallization (Ge/Au/Ag/Au). A high reflectivity (HR) coating (Al_2O_3/Ti/Au/Al_2O_3) was evaporated on their back facets. Finally, laser chips were separated and mounted epi-side up for testing on highly thermal-conductive Cu submounts.
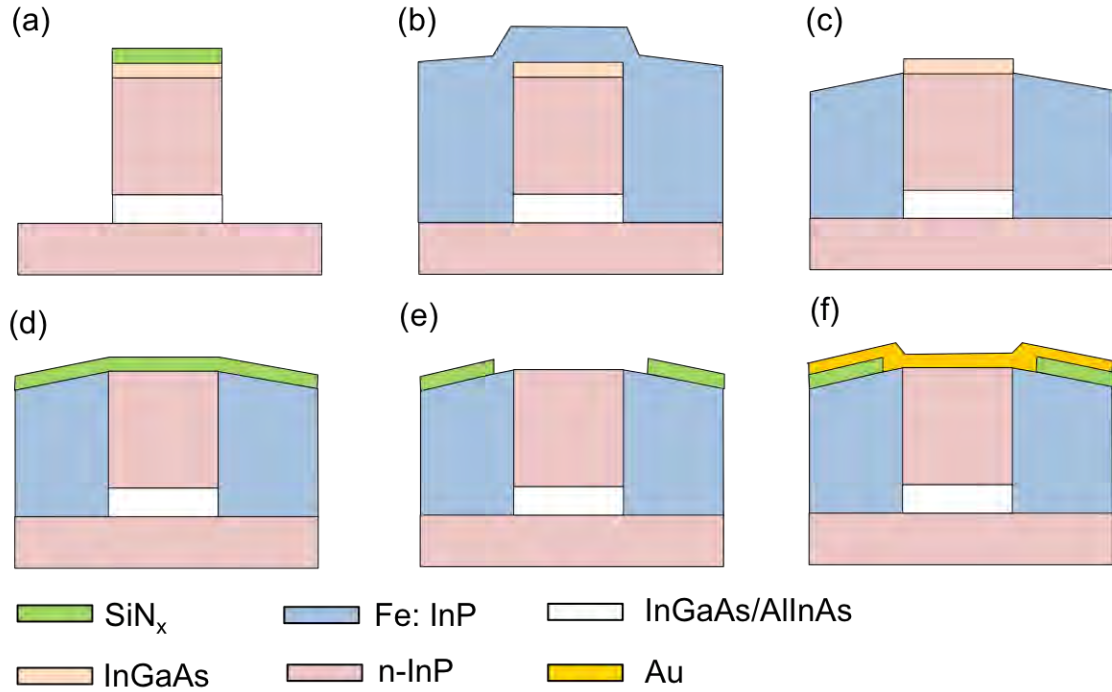
Fig. 4.3 Schematic of the main fabrication steps for BH-QCLs based on non-selective regrowth of Fe:InP and CP: (a) laser ridge formation by ICP etching followed by HBr wet etching; (b) non-selective regrowth of Fe:InP after removing the SiN$_x$ mask; (c) CP of excess regrown InP down to the InGaAs etch-stop layer; (d) deposition of SiN$_x$ layer for current confinement; (e) RIE of SiN$_x$ for current injection; and (f) metal evaporation.

4.4 Results and Discussion

Fig. 4.4(a) shows a low-magnification scanning electron microscopy (SEM) image of an etched QCL ridge of double- channel geometry after non-selective regrowth of Fe:InP. As can be seen, the overall surface morphology of the regrown Fe:InP basically follows that of the etched ridge before regrowth, and the ridge is completely buried in the regrown material. Although narrow dips in the regrown InP material are observed on both sides of the ridge (Fig. 4.4(b)), their effect on subsequent fabrication steps and device performance is negligible, as they are at least ~ 5 μm away from the ridge edges. After planarization via the CP step, as shown in Figs. 4.4(c) and 4.4(d), the Fe:InP layer regrown atop the ridge is completely removed; thus allowing for current injection. More importantly, the surface of the remaining regrown InP in the trenches is essentially featureless, extending smoothly from the ridge edge over large lateral distances (~ 25 μm). The overall planarity of the BH ridges after non-selective regrowth and CP can be further improved by significantly increasing the trench widths. Nevertheless, this non-selective regrowth/CP fabrication method for BH devices is quite robust, and can be easily applied to ridges oriented along any crystal orientation. By contrast, in the case of selective regrowth, the characteristics of regrown InP are strongly influenced by the orientation of the ridges. In particular, ridges tend to have either nearly vertical or severely re-entrant sidewall profile after wet etching, when are aligned along the [011] direction, for which the lateral growth rate underneath the dielectric mask is found to be rather large. That, in turn, often leads to considerable overgrowth on the mask, if the mask overhang length or thickness is not optimized. A complete BH-QCL device fabricated based on our method is shown in Fig. 4.5.
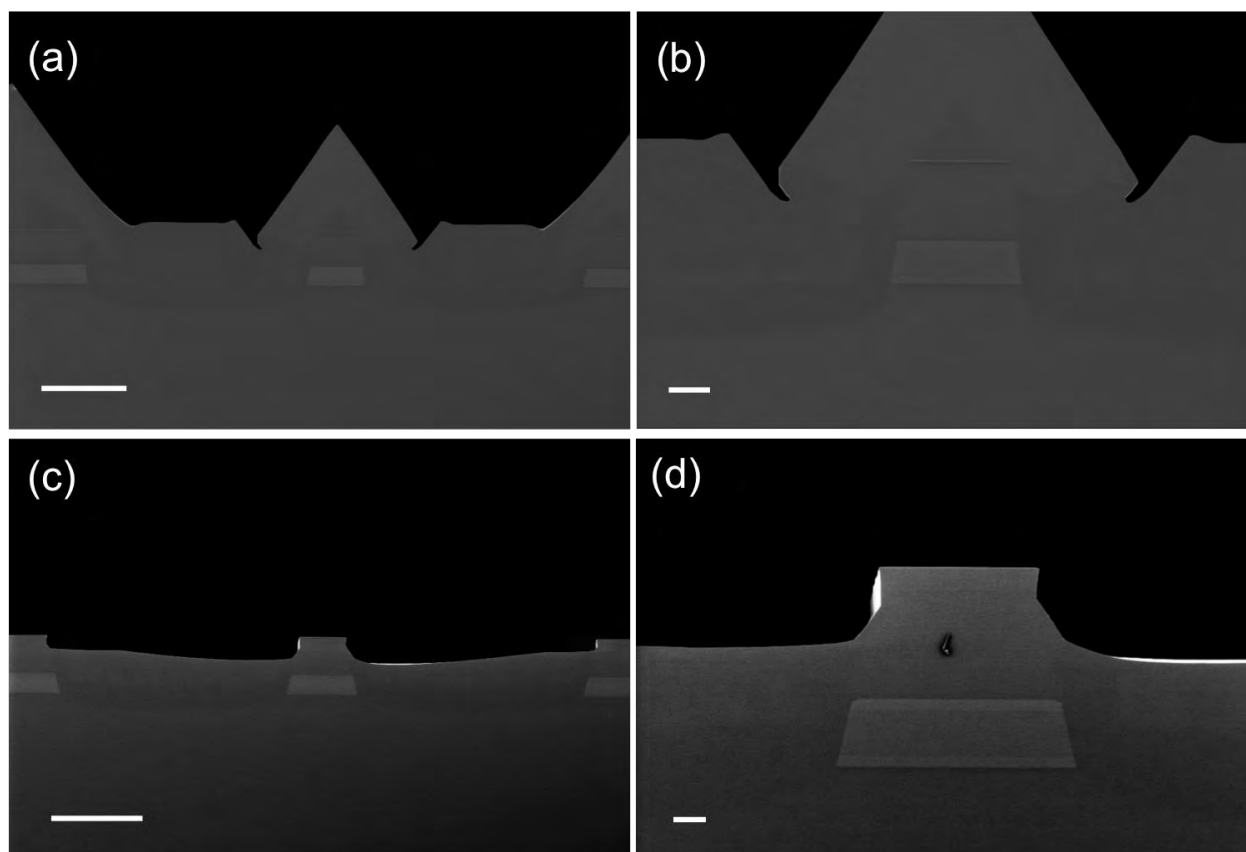
Fig. 4.4 Cross-section SEM images of: (a) an etched QCL ridge after non-selective Fe:InP regrowth; (b) an etched ridge after regrowth at higher magnification; (c) an etched ridge after CP; and (d) an etched ridge after CP at higher magnification. Scale bars are: (a) 10 μm; (b) 2 μm; (c) 10 μm; and (d) 1μm wide.
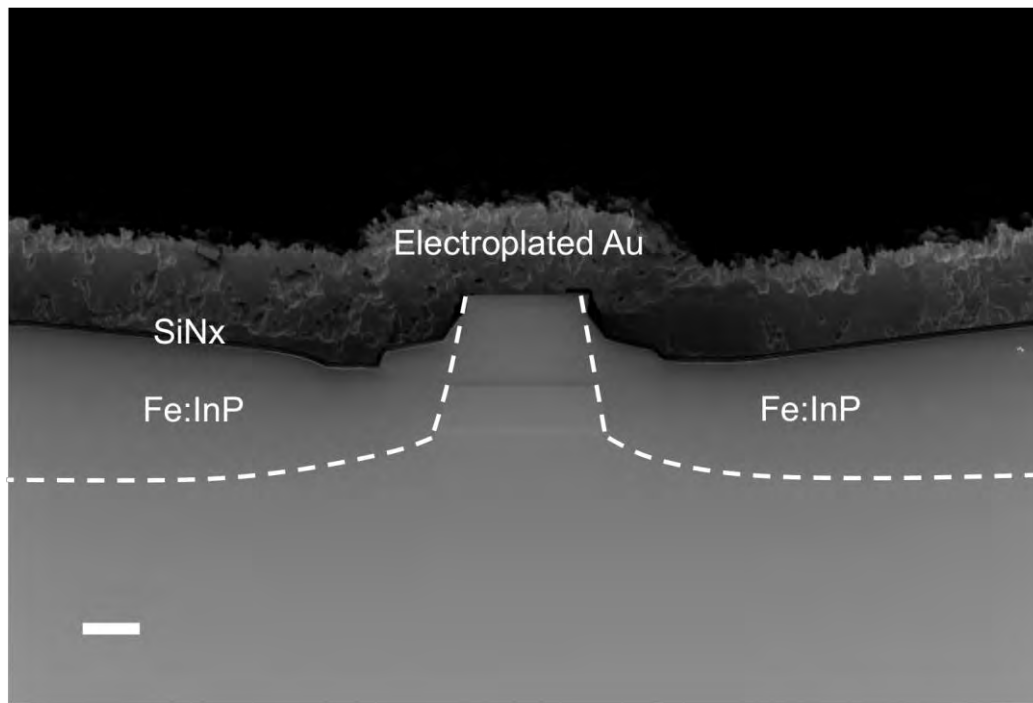
Fig. 4.5 Cross-section SEM image of a complete BH-QCL device. The scale bar is 2 μm wide.

Fig. 4.6(a) shows the light-current-voltage (*L-I-V*) characteristics of a fabricated BH-QCL device tested in CW operation at room temperature (*T*= 20°C). The optical power was measured and calibrated using a commercial thermopile. The threshold current of the device is 0.4 A, which corresponds to a threshold-current density of 1.78 kA/cm^2. The maximum output power is 170 mW, which could be further enhanced by epi-side down mounting using submounts with higher thermal conductivity such as diamond. For comparison, a reference device of similar active region width (~ 6.5 μm) without the regrown InP was also fabricated from the same wafer, and its maximum output power is

only 55 mW (Fig. 4.6(b)). Therefore, an ~ threefold enhancement in the maximum power is achieved by using the BH geometry due to better heat dissipation from the QCL core region [19].
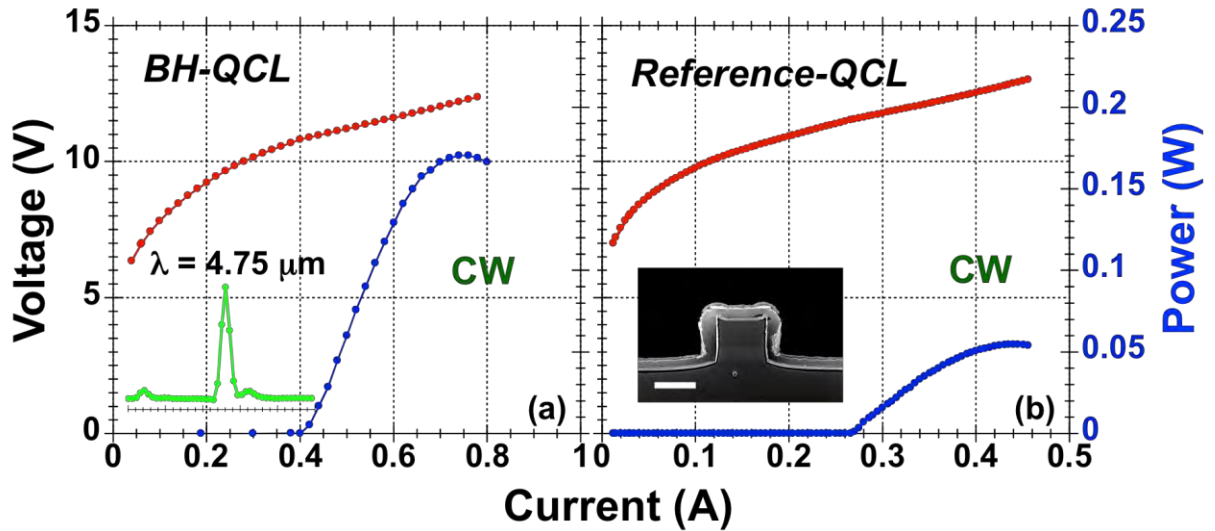
Fig. 4.6 *L-I-V* characteristics of fabricated BH-QCL (a); and reference-QCL (b). The insets show the emission spectrum and a cross-sectional SEM image of the reference QCL. The scale bar is 5 μm wide.

The fabrication method presented here can also be employed in making large emitting-aperture, phase-locked arrays of resonant leaky-wave coupled QCLs [20]. For such arrays, each laser element is typically only a few micrometers apart from one another, for a high degree of aperture filling, which poses a significant technological challenge as far as selectively regrowing Fe:InP in narrow openings while maintaining planarity over the entire device area. To serve as an example, we fabricated a prototype three-element QCL array with an interelement width of ~ 4.5 μm, based on non-selective regrowth and CP.

(Fig. 4.7) The laser elements were defined solely by ICP etching; hence their sidewalls are nearly vertical. Similar to the BH-QCL case, the entire array is buried after the InP regrowth, and the entire surface of the array device is completely planarized via CP.
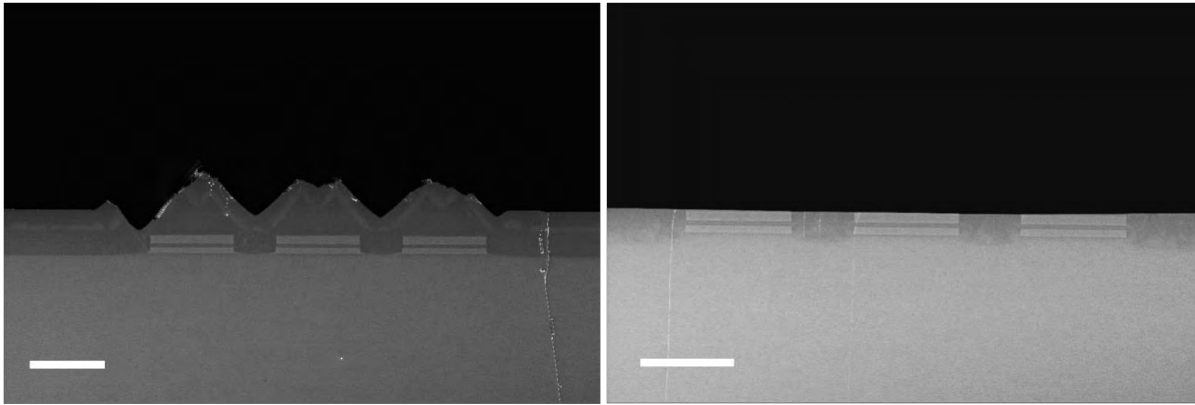
Fig. 4.7 SEM images of a fabricated three-element array after non-selective regrowth (a); and CP (b). The scale bars are 10 μm wide.

4.5 Conclusion

A novel fabrication method of BH-QCLs, based on non-selective regrowth using MOCVD and CP, is presented. The fabricated BH-QCLs provide ~ 3 times more CW output power compared to that from reference QCLs without regrown InP. This method is more flexible and robust compared to the selective-regrowth BH approach, and can be further employed for making large-emitting-aperture QCL arrays with narrow interelement widths.

Reference

[1] J. Faist, F. Capasso, D. Sivco, C. Sirtori, A. Hutchinson, and A. Cho. "Quantum cascade laser", *Science*, **264**, 553-556 (1994).

[2] J. Faist, F. Capasso, C. Sirtori, D. L. Sivco, A. L. Hutchinson, and A. Y. Cho. "Continuous wave operation of a vertical transition quantum cascade laser above T= 80 K", *Appl. Phys. Lett.*, **67**, 3057-3059 (1995).

[3] M. Beck, D. Hofstetter, T. Aellen, J. Faist, U. Oesterle, M. Ilegems, E. Gini, and H. Melchior. "Continuous wave operation of a mid-infrared semiconductor laser at room temperature", *Science*, **295**, 301-305 (2002).

[4] D. Hofstetter, M. Beck, T. Aellen, and J. Faist. "High-temperature operation of distributed feedback quantum cascade lasers at 5.3 μm", *Appl. Phys. Lett.*, **78**, 396 (2001).

[5] J. Faist, F. Capasso, C. Sirtori, D. L. Sivco, J. N. Baillargeon, A. L. Hutchinson, S.-N. G. Chu, and A. Y. Cho. "High power mid-infrared ($\lambda \sim 5$ μm) quantum cascade lasers operating above room temperature", *Appl. Phys. Lett.*, **68**, 3680-3682 (1996).

[6] C. Gmachl, M. Sergent, A. Tredicucci, F. Capasso, A. L. Hutchinson, D. L. Sivco, J. N. Baillargeon, S.-N. G. Chu, and A. Y. Cho. "Improved CW operation of quantum cascade lasers with epitaxial-side heat-sinking", *IEEE Photon. Technol. Lett.*, **11**, 1369-1371 (1999).

[7] D. Hofstetter, M. Beck, T. Aellen, J. Faist, U. Oesterle, M. Ilegems, E. Gini, and H. Melchior. "Continuous wave operation of a 9.3 μm quantum cascade laser on a Peltier cooler", *Appl. Phys. Lett.*, **78**, 1964-1966 (2001).

[8] M. Beck, J. Faist, C. F. Gmachl, F. Capasso, D. L. Sivco, J. N. Baillargeon, and A. Y. Cho. "Buried heterostructure quantum cascade lasers", *Proc*. *SPIE*, **3284**, 231-236 (1998).

[9] M. Beck, J. Faist, U. Oesterle, M. Ilegems, E. Gini, and H. Melchior. "Buried heterostructure quantum cascade lasers with a large optical cavity waveguide", *IEEE Photon*. *Technol*. *Lett*., **12**, 1450-1452 (2000).

[10] M. Beck, D. Hofstetter, T. Aellen, J. Faist, U. Oesterle, M. Ilegems, E. Gini, and H. Melchior. "Continuous wave operation of a mid-infrared semiconductor laser at room temperature", *Science*, **295**, 301-305 (2002).

[11] A. Evans, J. S. Yu, J. David, L. Doris, K. Mi, S. Slivken, and M. Razeghi. "High-temperature, high-power, continuous-wave operation of buried heterostructure quantum cascade lasers", *Appl*. *Phys*. *Lett*., **84**, 314-316 (2004).

[12] A. Evans, S. R. Darvish, S. Slivken, J. Nguyen, Y. Bai, and M. Razeghi. "Buried heterostructure quantum cascade lasers with high continuous-wave wall plug efficiency", *Appl*. *Phys*. *Lett*., **91**, 071101 (2007).

[13] Y. Bai, S. R. Darvish, S. Slivken, W. Zhang, A. Evans, J. Nguyen, and M. Razeghi. "Room temperature continuous wave operation of quantum cascade lasers with watt-level optical power", *Appl*. *Phys*. *Lett*., **92**, 101105 (2008).

[14] A. Lyakh, C. Pflügl, L. Diehl, Q. J. Wang, F. Capasso, X. J. Wang, J. Y. Fan, T. Tanbun-Ek, R. Maulini, A. Tsekoun, R. Go, and C. Kumar N. Patel. "1.6 W high wall plug efficiency, continuous-wave room temperature quantum cascade laser emitting at 4.6 μm", *Appl*. *Phys*. *Lett*., **92**, 111110 (2008).

[15] A. Lyakh, R. Maulini, A. Tsekoun, R. Go, C. Pflügl, L. Diehl, Q. J. Wang, F. Capasso, and C. Kumar N. Patel. " 3 W continuous-wave room temperature single-facet emission from quantum cascade lasers based on nonresonant extraction design approach", *Appl. Phys. Lett.*, **95**, 141113 (2009).

[16] Y. Bai, N. Bandyopadhyay, S. Tsao, S. Slivken, and M. Razeghi. "Room temperature quantum cascade lasers with 27% wall plug efficiency", *Appl. Phys. Lett.*, **98**, 181102 (2011).

[17] L. Cheng, J. Fan, D. Janssen, D. Guo, X. Chen, F. Towner, and F.-S. Choa. " Analysis of InP regrowth on deep-etched mesas and structural characterization for buried-heterostructure quantum cascade lasers", *J. Electron. Mater.*, **41**, 506-513 (2012).

[18] P. Bandaru and E. Yablonovitch. "Semiconductor surface-molecule interactions wet-etching of InP by α-Hydroxy acids", *J. Electrochem. Soc.*, **149**, G599-G602 (2002).

[19] C.-C. Chang, J. D. Kirch, P. Buelow, C. Boyle, T. F. Kuech, D. Lindberg III, T. Earles, D. Botez, and L. J. Mawst. "Buried-heterostructure mid-infrared quantum cascade lasers fabricated by non-selective regrowth and chemical polishing", *Electron. Lett.*, accepted (2015).

[20] D. Botez, L. J. Mawst, and G. Peterson. "Resonant leaky-wave coupling in linear arrays of antiguides", *Electron. Lett.*, **24**, 1328 (1988).

CHAPTER FIVE

FABRICATION OF PHASE-LOCKED ANTIGUIDED ARRAYS OF QUANTUM CASCADE LASERS

5.1 Phase-Locked Antiguided Arrays

Phase-locked antiguided arrays are linear arrays of antiguides based on resonant leaky-wave coupling [1-2]. At resonance, owing to the full transmission in the interelement regions, each element couples equally to all the other elements in the lateral direction. Due to this global coupling, full coherence across the entire array is established. This, in turn, ensures the maximized intermodal discrimination and hence the lasing of favorable resonant modes. Furthermore, the antiguided arrays are less vulnerable to the thermal- and injected-carrier-induced refractive-index variation, as well as gain spatial hole burning (GSHB), due to their large built-in refractive-index step ($\Delta n > 0.05$). As a result, these arrays exhibit greater optical mode stability at high current drive above the threshold. The full coherence and mode stability make phase-locked antiguided arrays an ideal candidate for large-emitting-aperture, high-power coherence sources with stable single spatial mode control.

Phase-locked antiguided arrays have been extensively studied over the past decades, and experimentally demonstrated in the near-infrared spectral region, producing high coherent output power in near-diffraction-limited beam patterns. Mawst et al. [3] in 1988 reported the first phase-locked antiguided arrays via MOCVD growth method. The high-index interelement regions of the arrays were formed by preferential chemical wet etching of the base structure, followed by non-selective regrowth of p-type $Al_{0.1}Ga_{0.9}As$,

$Al_{0.3}Ga_{0.7}As$, and GaAs layers. In these regions the fundamental transverse mode is primarily confined to the passive $Al_{0.1}Ga_{0.9}As$ layer rather than the active region, therefore the modal gain is lower compared to that in the elements. The lateral far-field patterns of the fabricated eight-element arrays exhibit resonant in-phase fundamental element mode near the threshold, but a mixture of resonant in-phase and out-of-phase modes at higher drive current, due to their similar threshold currents. In 1989 Botez et al. [4] further reported a ten-element, AlGaAs/GaAs resonant optical waveguide (ROW) diode laser arrays based on a similar structure, but with different AlGaAs layer thicknesses and Al composition. At the designed index step ($\Delta n \sim 2.8 \times 10^{-2}$), the resonant in-phase mode ($L = 18$) has the maximized intermodal discrimination against the upper adjacent mode ($L = 19$), due to the large radiation loss of mode 19. The resulting arrays show stable, diffraction-limited, in-phase mode operation up to a drive level in excess of three times threshold. By introducing both interelement loss and a monolithically integrated diffractive spatial filter at half Talbot distance, for the suppression of out-of-phase mode, Mawst et al. [5] demonstrated ten/eleven-element AlGaAs/GaAs phase-locked antiguided arrays which operate in diffraction-limited in-phase mode up to ten times threshold with an output power of 450 mW. In 1991, the first phase-locked antiguided arrays of diode lasers emitting diffraction-limited, watt-range coherent output power in pulsed mode were reported by Botez et al. [6]. In 1993, Zmudzinski et al. [7] demonstrated, for the first time, near-diffraction-limited ($1.7 \times$ D.L.), watt-level coherent output power (~ 1 W) in continuous-wave (CW) mode from phase-locked antiguided diode laser arrays.

In the recent years, tremendous progresses were made in optimizing the device performance of phase-locked antiguided diode-laser arrays. In 1997, Yang et al. [8] reported a 40-element, 200 μm-aperture, Al-free phase-locked antiguided arrays of diode lasers (λ = 0.98 μm) based on InGaAs/InGaAsP/InGaP material system. These arrays were designed to operate near the resonance of in-phase fundamental element mode on the high Δn-side of the resonance. Devices were fabricated by two-step self-aligned etch-and-regrowth process. 10 W peak-pulsed power in near-diffraction-limited beam (2 × D.L.), with 60% power in the central lobe, was demonstrated. From similar 40-element antiguided arrays but with a larger inde-step (Δn ~ 0.1), Yang et al. [9] successfully improved the CW coherent output power up to 1.6 W in a near-diffraction-limited (2 × D.L.) beam, with 1 W in the main lobe. The modeling of thermal effects in CW operation on the array modes also proves that the high index step is the key to maintaining high CW output power in near-diffraction-limited beams.

5.2 Coherent Power Scaling of Mid-Infrared QCLs

The output power of mid-infrared quantum cascade lasers (QCLs) has been significantly improved in recent years. The state-of-the-art QCLs (λ = 4.6 μm) have shown peak output powers of multiwatts in CW mode at room temperature. However, in order to reduce the device self-heating, the high-power QCL devices involve sophisticated processing and mounting techniques, and require expensive submounts such as diamond. On the other hand, the large-emitting-aperture, broad-area devices are also promising for producing high output power by increasing the volume of gain medium. Due to the increased emitting area, these devices support undesirable higher-order lateral modes, and

hence have fairly broad far-field beams. In addition, other nonlinear phenomena including hole burning and filamentation are more pronounced in the broad-area devices as the laser power increases. To improve the spatial beam quality, Vurgaftman et al. [10] in 2001 proposed a new type of broad-area laser device, called photonic crystal distributed feedback lasers (PCDFB). The PCDFB lasers, as illustrated in Fig. 5.1, where the grating is defined by etching a two-dimensional rectangular lattice of holes in the grating layer tilted with respect to the laser facets, are expected to offer the possibility of both high beam quality and spectral purity. In 2007, Bai et al. [11] demonstrated electrically pumped PCDFB lasers in the mid-infrared region by using 4.75 μm-emitting QCLs. Despite a low peak pulsed-power of < 300 mW, the fabricated 100 μm-wide PCDFB lasers indeed emit in a single spectral mode, and have a diffraction-limited far-field profile. By doubling the injector doping level, Bai et al. [12] further improved the power performance of PCDFB lasers, achieving a peak power of ~ 6 W per facet in pulsed mode at room temperature. However, these PCDFB lasers show a near-diffraction-limited beam at a current drive only 10% above the threshold, where the output power is merely 0.5 W per facet. Furthermore, the refractive index contrast of PCDFB structure, is only ~ 0.0008. The low index contrast of PCDFB lasers would therefore result in severe beam instability when operated at high current drive in quasi-CW and CW mode.

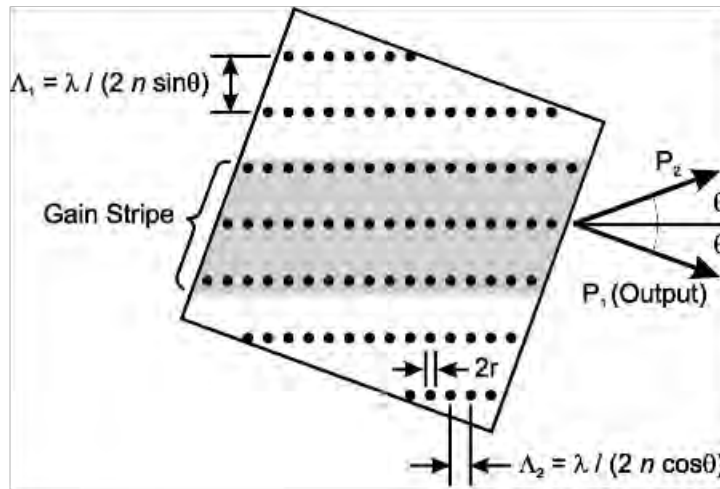
Fig. 5.1. Schematic of PCDFB lasers. The grating is defined by etching two-dimensional array of holes (black circles) in the grating layer prior to the regrowth of upper cladding layer. The gain stripe (shaded region) is tilted with respect to the facets. Two propagation axes are denoted as P_1 and P_2.

In addition to PCDFB lasers, several other broad-area devices using QCLs have been realized for coherent power scaling in the mid-infrared region using QCLs. Rauter et al. [13] demonstrated an array of master-oscillator power-amplifier (MOPA) based on mid-infrared QCLs. The fabricated multi-wavelength, MOPA-QCL array, as show in Fig. 5.2, consists of sixteen MOPA elements, where each element is designed to emit at a specific wavelength from $\lambda = 9.2$ to 9.8 μm. In each element, the output of a low-power, single-mode distributed feedback (DFB) QCL that acts as a master oscillator (MO), is coupled into a tapered quantum cascade power amplifier (PA) section. All array elements show single-mode operation with a side-mode suppression-ratio (SMSR) of at least 15 dB in

pulsed mode at room temperature. The peak output power of these 110 μm-wide MOPAs varies from 0.8 W to 3.9 W, due to the fabrication nonuniformity of the DFB sections. Their measured far-field patterns exhibit near-diffraction-limited beams ($\sim$ 6°) at peak powers. Despite the demonstrated high output power and excellent beam quality, the MOPA configuration is essentially unreliable for high-power devices in CW mode, in that they have no built-in index step for lateral optical mode confinement, and therefore are sensitive to thermal lensing under CW operation due to device self-heating. In addition, any random nonuniformities in the lateral direction of MOPA devices are likely to cause filamentation, and subsequent beam degradation. At $\lambda = 4.6$ μm, Lyakh et al. [14] reported tree arrays of buried-heterostructure (BH) QCLs connected by multiple Y-junctions (Fig. 5.3) using selective regrowth of Fe:InP via hydride vapor phase epitaxy (HVPE). Although single Y branch (i.e., two QCL elements) demonstrates 0.32 W of CW output power in a single-lobe far-field beam, the fabricated four-element QCL tree arrays have a fairly broad far-field pattern at a low output power level of 400 mW, indicative of the multi-mode operation. Similarly, by using BH ridges via HVPE regrowth of Fe:InP between array elements, de Naurois et al. [15] realized evanescent-wave coupled phase-locked arrays of QCLs emitting at $\lambda = 8.4$ μm, as shown in Fig. 5.4(a) and (b). As expected, these evanescent-type devices operate only in the out-of-phase array mode, as the measured far-field patterns (Fig. 5.4(c)) from both eight- and sixteen-element arrays show two distinctive lobes. To maintain single spatial-mode operation in a stable, diffraction-limited far-field beam at a high CW power, a broad-area array device needs to operate via strong parallel coupling between elements, and possess a large built-in index

step. Clearly, the QCL array devices demonstrated so far in the mid-infrared region are fundamentally impractical to achieve this goal.
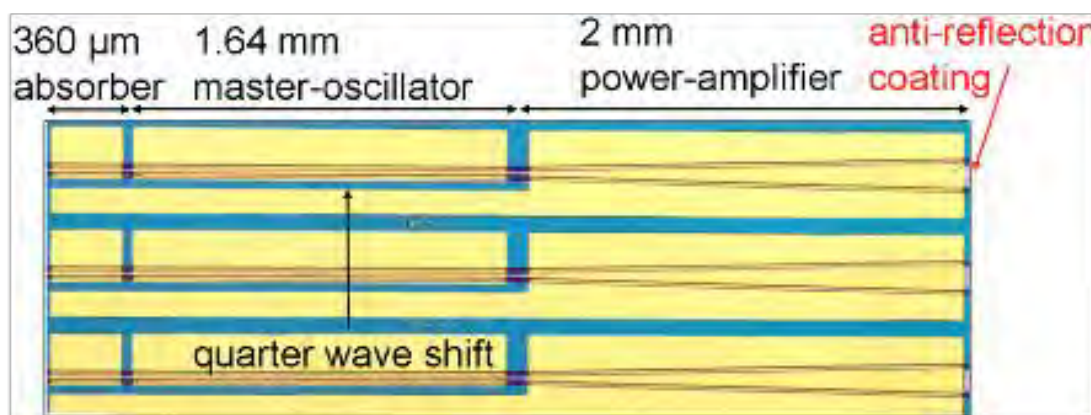
Fig. 5.2. Top view of fabricated MOPA-QCL array.
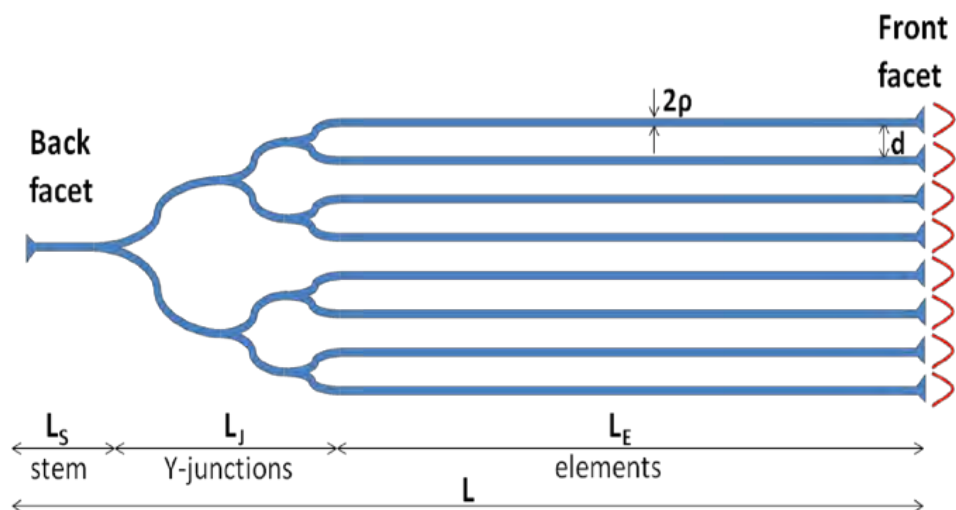
Fig. 5.3. Schematic of tree array of mid-infrared QCLs.
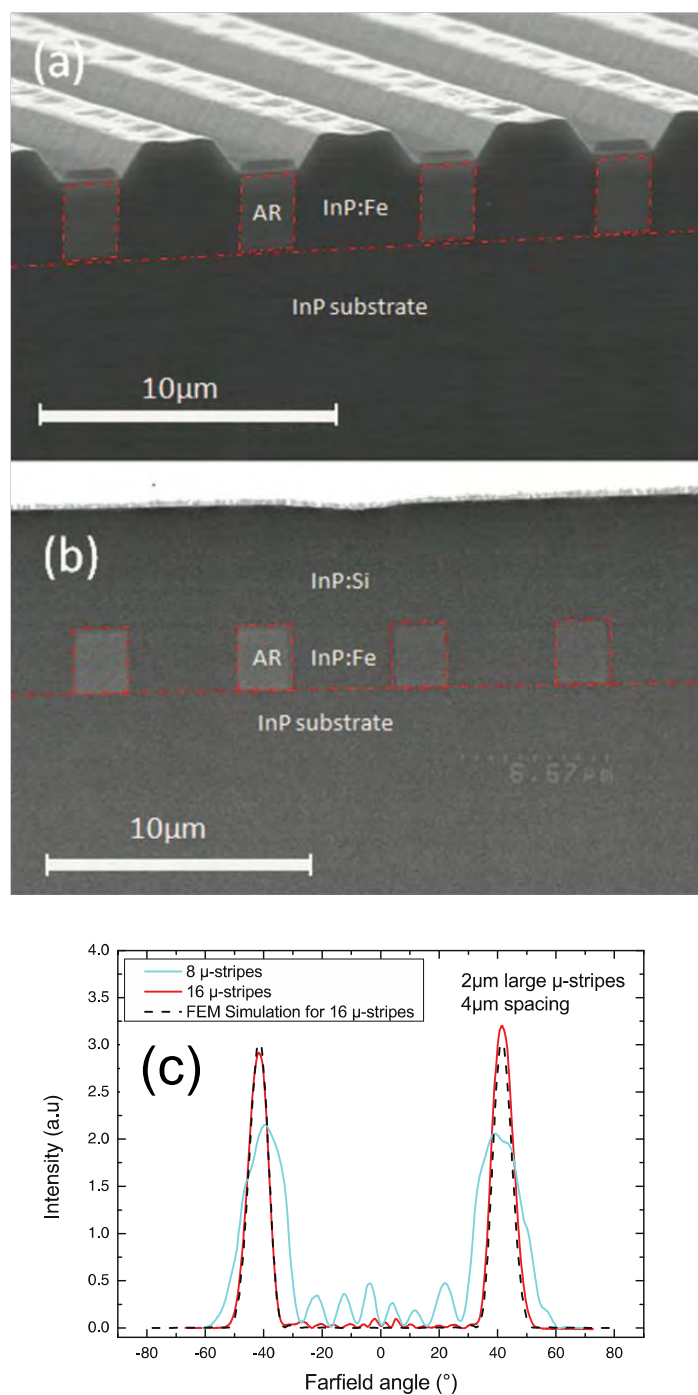
Fig. 5.4. Cross-section SEMs of evanescent-wave coupled QCL arrays (a) after Fe:InP regrowth between elements; and (b) after device fabrication. (c) Measured far-field patterns of eight- and sixteen-element arrays.

5.3 Phase-Locked Antiguided QCL Arrays

In our work, we demonstrated 8.36 μm-emitting phase-locked antiguided arrays of QCLs via resonant leaky-wave coupling. The structure of our five-element antiguided arrays of QCLs is illustrated in Fig. 5.5. The QCL active region is composed of upper and lower cores, separated by an InP interstack layer. This InP layer not only serves as an etch-stop layer in the device fabrication, but also provides better thermal dissipation in the lateral direction. The high-index, low-gain interelement regions are formed by first etching high-aspect-ratio trenches in the QCL base material, followed by the selective regrowth of high-index semiconductor materials, in our case, InGaAs, and the electroplating of thick Au, thus leading to a high built-in index-step ($\Delta n = 0.08 - 0.12$) in the arrays. In the high-index regions, the regrown InGaAs draws the field away from the active region in the growth direction, and in turn, leads to reduced field overlap and modal gain. Furthermore, the electroplated Au layer is lower in these regions compared to that in the elements. As a result, the competing modes in the interelement regions experience strong absorption losses to the metal layer, and can accordingly be suppressed by the interelement loss. Finally, due to the large element width ($d \sim 15$ μm), the edge-radiation losses (α_{RR}) are small as they scale inversely with d^3. Therefore, the array modes composed of coupled first-order element modes (array mode $L = 13$) can also compete for lasing, as their resonance condition is met close to that for in-phase coupled fundamental modes (array mode $L = 8$). In order to suppress the coupled first-order array modes peaking up close to the element edges, we etch the corners of element regions (~ 4 μm wide) by ~ 1 μm deep to introduce the absorption losses to the Au layer.

As shown in Fig. 5.6, the resonance of in-phase fundamental element modes (array mode $L = 13$) occurs when the interelement width s is equal to half of the lateral wavelength (m = 1). From the full-wave simulation using COMSOL, this resonance occurs when the interelement width s is approximately 6 µm. In addition, as can be seen in the dependence of simulated threshold current density (J_{th}) on the interelement width, the intermodal discrimination of the resonant in-phase mode against the upper ($L = 9$) and lower ($L = 7$) adjacent array modes is maximized, over a 1 µm-wide range in s values from 5.6 to 6.6 µm. This 1 µm-wide window is about an order of magnitude higher than that for the antiguided arrays in the near-infrared region, and thus provides larger fabrication tolerances.
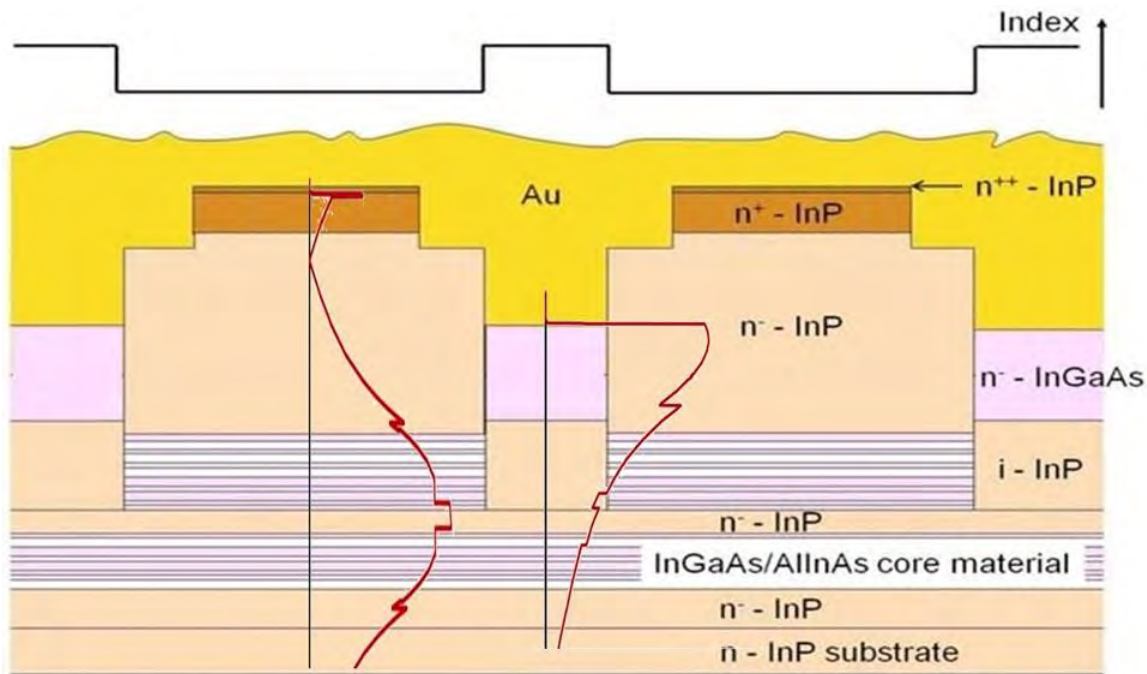
Fig. 5.5. Schematic cross-section of phase-locked antiguided arrays of QCLs.
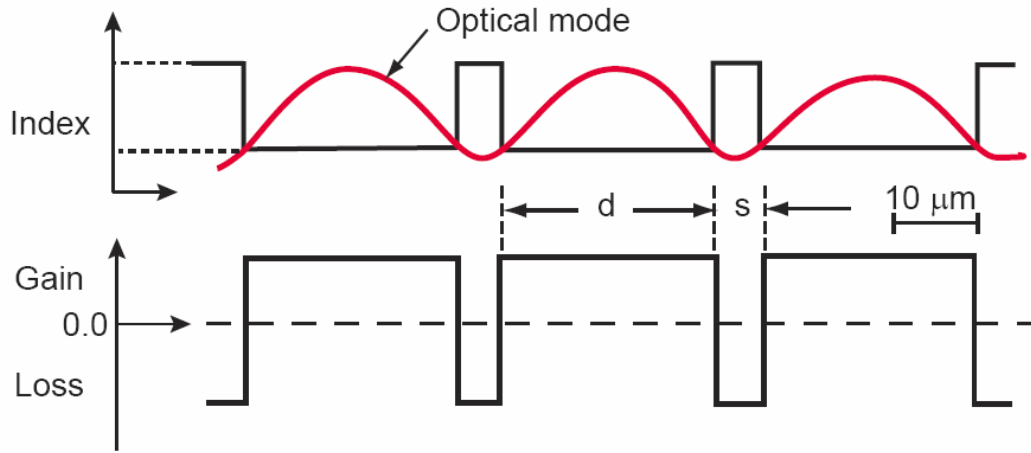
Fig. 5.6. Schematic representation of resonant leaky-wave coupled arrays of antiguides.

5.4 Device Fabrication

Initially, an 8.36 μm-emitting QCL was grown using metal-organic chemical vapor deposition (MOCVD) based on the active region design published by Z. Liu et al. [16]. The active region includes 46 stages with a 0.5 μm-thick InP spacer layer, and is sandwiched between 0.1 μm-thick InGaAs waveguide layers. Then, 2 μm-thick, low-doped (2×10^{16} cm^{-3}) InP cladding layer was first grown to minimize the waveguide loss, followed by another 2 μm-thick InP layer with higher doping (1×10^{17} cm^{-3}). Finally, a 5 $\times 10^{18}$ cm^{-3}-doped, 0.5 μm-thick InP plasmon layer was grown followed by a 2 $\times 10^{19}$ cm^{-3}-doped, 0.15 μm-thick InP cap layer to complete the growth of base material.

After the growth of base material, ~ 4.5 μm-wide openings were defined in a 500 nm-thick Si$_3$N$_4$ film deposited by plasma enhanced chemical vapor deposition (PECVD) using photolithography and reactive-ion etching (RIE), for etch and selective regrowth. Using Si$_3$N$_4$ hardmask, trenches were first wet etched in InP using H$_3$PO$_4$/HCl solution.

The etch rate and sidewall profile of InP wet etching using H_3PO_4/HCl-based solution depend highly on the stripe orientation, as well as the volume ratio of H_3PO_4 to HCl. As shown in Fig. 5.7, when the stripes are oriented along the $[01\bar{1}]$ direction, the etched trenches appear to have sloping sidewalls, regardless of the volume ratio of H_3PO_4 to HCl. The sloping sidewall profile is unfavorable for the array fabrication, since the trench width has to be precisely controlled in order to meet the resonance condition. On the other hand, when the stripes are aligned along the $[011]$ direction, trenches with nearly vertical sidewalls are formed after wet etching. The etch rate of InP can be further adjusted by varying the volume ratio of H_3PO_4 to HCl, as shown in Fig. 5.8. In the array device fabrication, we use H_3PO_4 to HCl = 3:1 solution to etch trenches with high aspect-ratio of ~ 1:1 in InP cladding layer, at an etch rate of ~ 1μm/ min. There is only little lateral undercut (~250 nm) observed using this etchant when stripes are aligned along $[011]$ direction. Furthermore, the H_3PO_4/HCl-based solution is a selective etchant of InP over InGaAs. Therefore, as shown in Fig. 5.9, the InP wet etching is stopped at 0.1 μm-thick InGaAs waveguide layer atop the QCL cores.
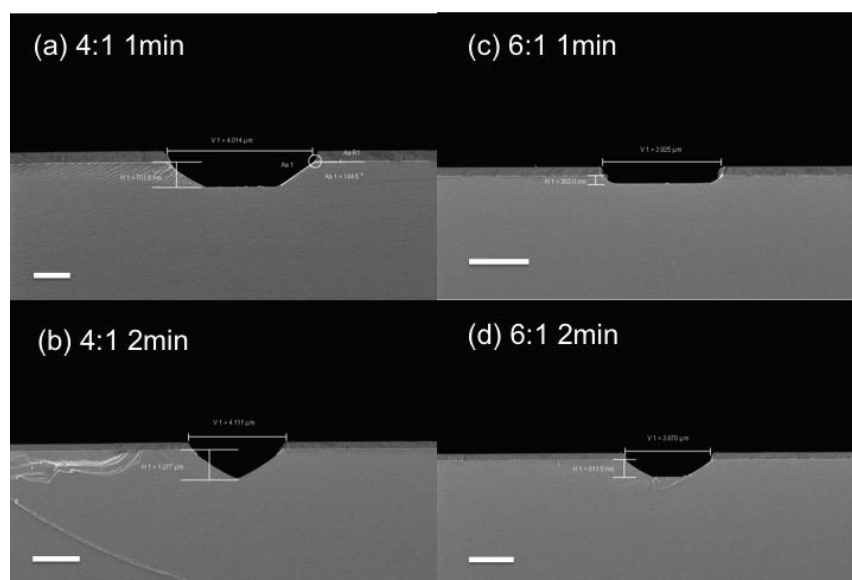
Fig. 5.7. SEMs of InP wet etching when stripes are aligned along $[01\bar{1}]$ direction using (a) H_3PO_4: HCl = 4:1 for 1 min; (b) H_3PO_4: HCl = 4:1 for 2 min; (c) H_3PO_4: HCl = 6:1 for 1 min; and (d) H_3PO_4: HCl = 6:1 for 2 min. Scale bars are (a) 1 μm; (b) 2 μm; (c) 2 μm; and (d) 2 μm.
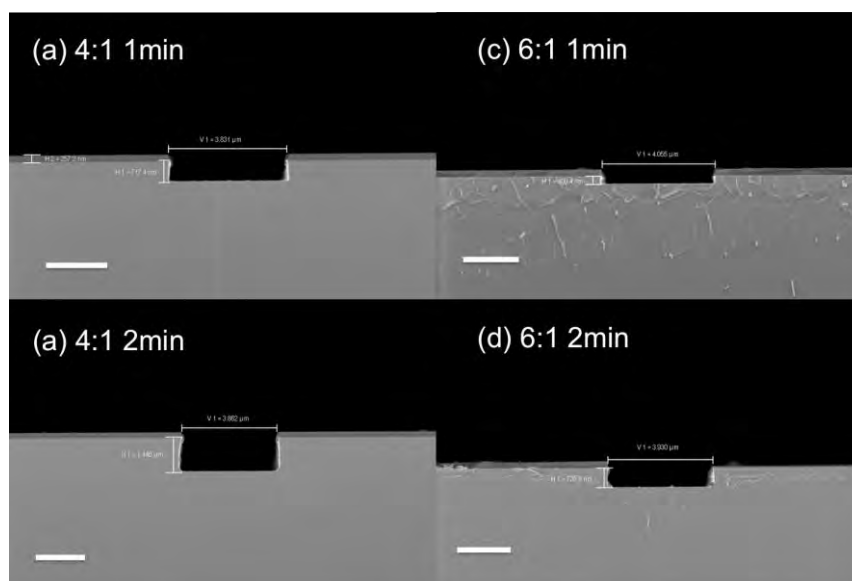
Fig. 5.8. SEMs of InP wet etching when stripes are aligned along [011] direction using (a) H_3PO_4: HCl = 4:1 for 1 min; (b) H_3PO_4: HCl = 4:1 for 2 min; (c) H_3PO_4: HCl = 6:1 for 1 min; and (d) H_3PO_4: HCl = 6:1 for 2 min. Scale bars are 2 μm.
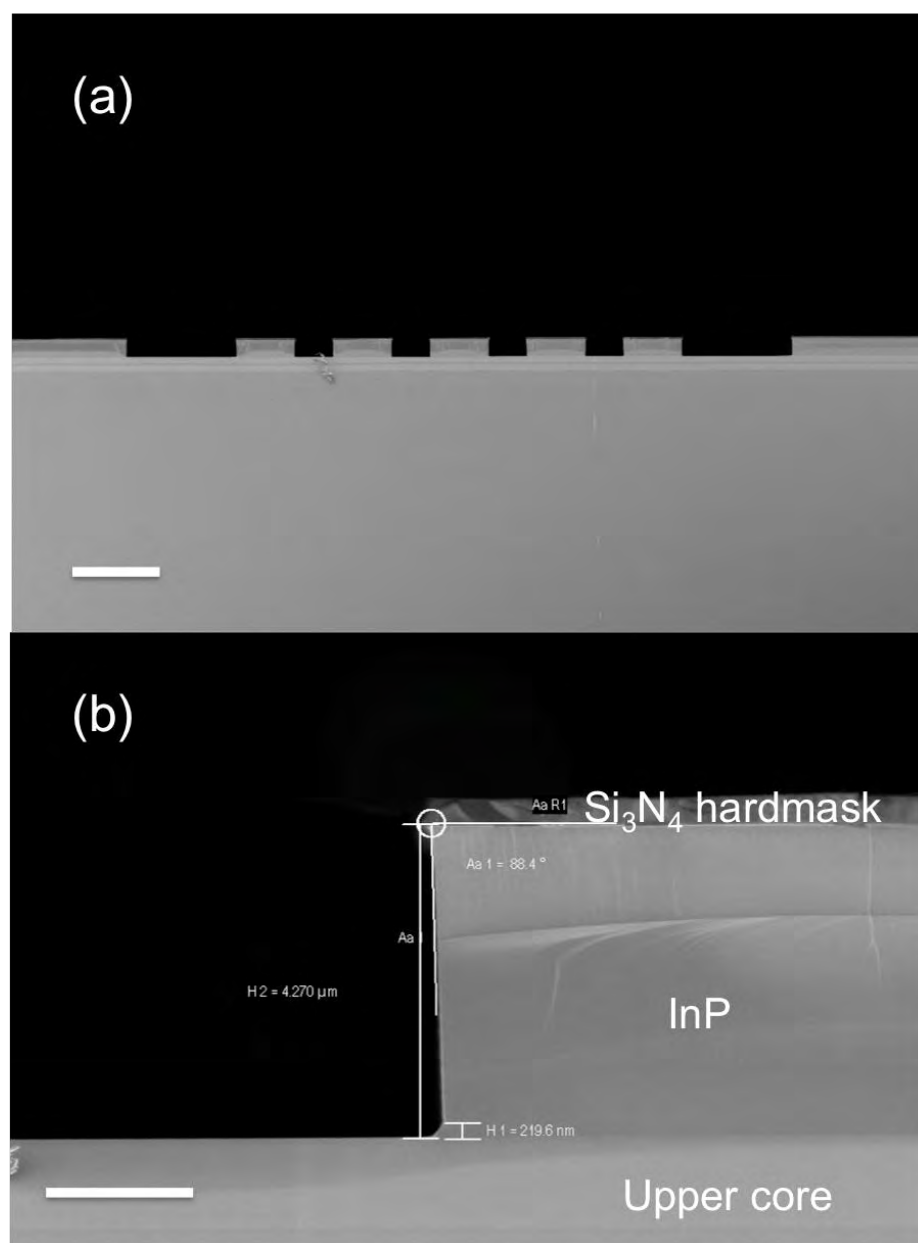
Fig. 5.9. SEMs of InP wet etching using H_3PO_4: HCl = 3:1 solution. Scale bars are (a) 20 μm; and (b) 2 μm.

After the trenches with nearly vertical sidewalls are formed in the InP cladding layer, the upper core, composed of ternary materials InGaAs and AlInAs, is etched by plasma dry etching. In our experiment the core materials are dry etched using electron-cyclotron resonance (ECR) plasma etching at $T = 20$ °C. In order to prevent polymer deposition during the etching, an etching process involving cyclic etching and oxygen-plasma cleaning steps are employed. Within each etching cycle, the sample is first briefly etched in the $CH_4/H_2/BCl_3/Ar/O_2$ ambient, and then exposed to oxygen plasma at 100 W for 2 min. After the oxygen-plasma cleaning step is completed, the chamber is purged with nitrogen, and the etching gases are flowed back into the chamber for the next cycle. Since the InGaAs/AlInAs superlattice etches at a rate of ~ 45 nm/cycle, total 24 cycles of etching and cleaning steps are needed to reach the target etch depth of ~ 1.0 μm, within ~ 0.5 μm from the InP spacer layer. Finally, to obtain a suitable trench profile and mask overhang required for the selective regrowth, the sample is etched in an HBr/HNO_3 solution after ECR dry etching. The representative trench profile after the etching process is shown in Fig. 5.10. Approximately 1.0 μm-wide of the Si_3N_4 mask overhang is needed to prevent considerable overgrowth on the mask and form "rabbit ears" around the mask edges after the regrowth. The re-entrant InP sidewall profile right underneath the Si_3N_4 mask is expected as the stripes are patterned along the [011] direction. The interelement width s is targeted at ~ 6 μm to meet the resonance condition for the in-phase coupled fundamental modes.
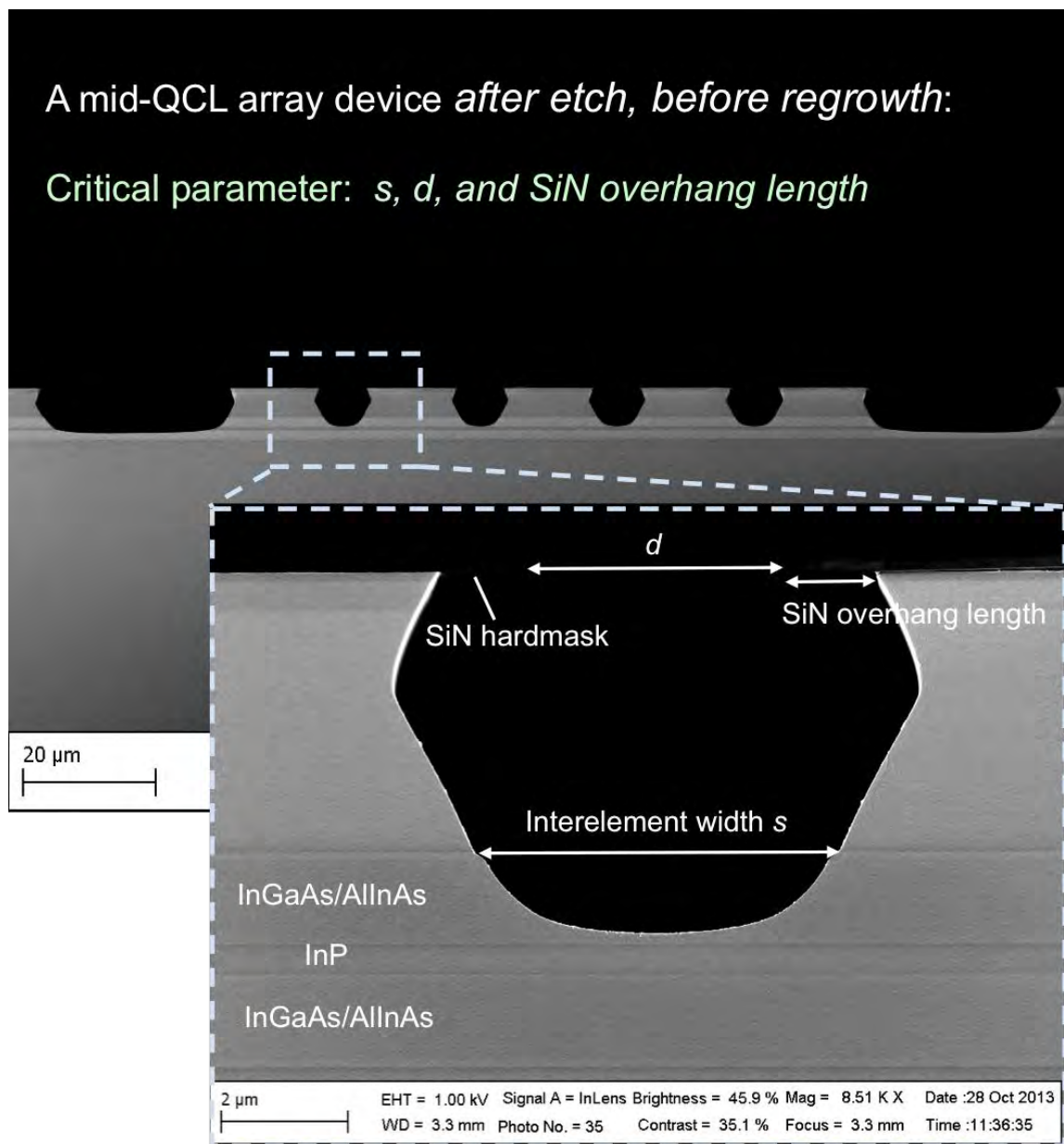
Fig. 5.10. SEMs of trench profile after wet and dry etching.

After the etch process, the sample is dipped in pure sulfuric acid (98%) for 30 sec to remove the surface oxide prior to the regrowth. Two curved interelement layers, Fe-doped InP and undoped InGaAs were then selectively regrown via MOCVD, which are targeted to have central thicknesses of 1.2 um and 1.1 um, respectively. In our early regrowth tests, we found out that the regrowths were not reproducible if we etched through the upper core and slightly exposed the InP spacer before the regrowth. By leaving ~ 0.2 μm-thick upper core after HBr/HNO$_3$ etch, the regrowths are reproducible and the typical regrowth results are shown in Fig. 5.10.
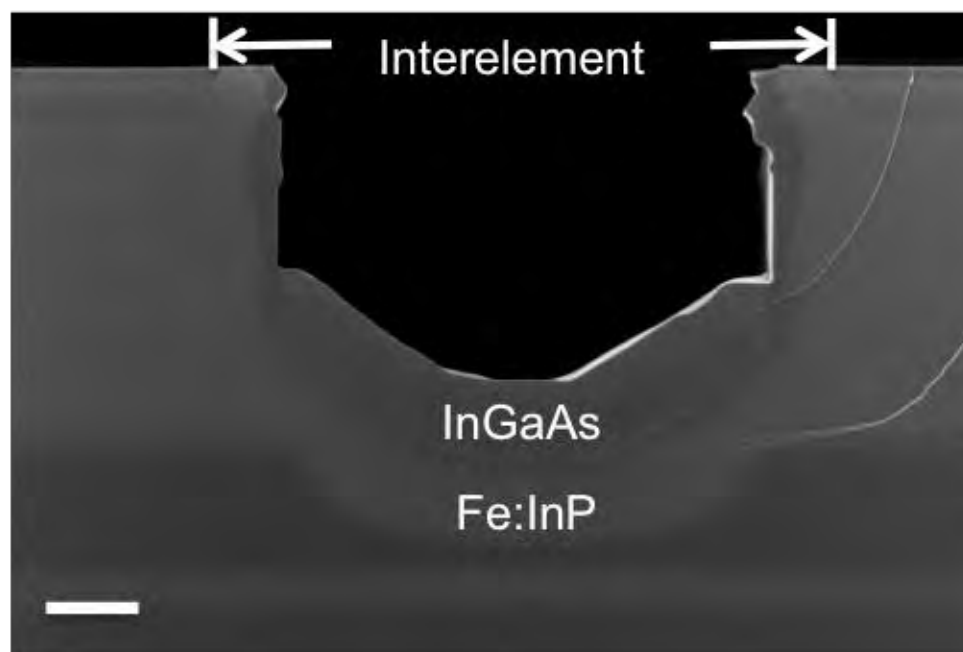
Fig. 5.11. SEMs of selective regrowth of interelement layers. Scale bar is 1 μm.

Subsequently, the Si_3N_4 mask is removed using HF (49%), and a 300 nm-thick PECVD Si_3N_4 mask was deposited, patterned and etched via RIE. Using Si_3N_4 mask, the corners (~3 μm-wide) of the element regions are etched to ~ 1 μm deep using H_3PO_4/HCl solution, as show in Fig. 5.12.
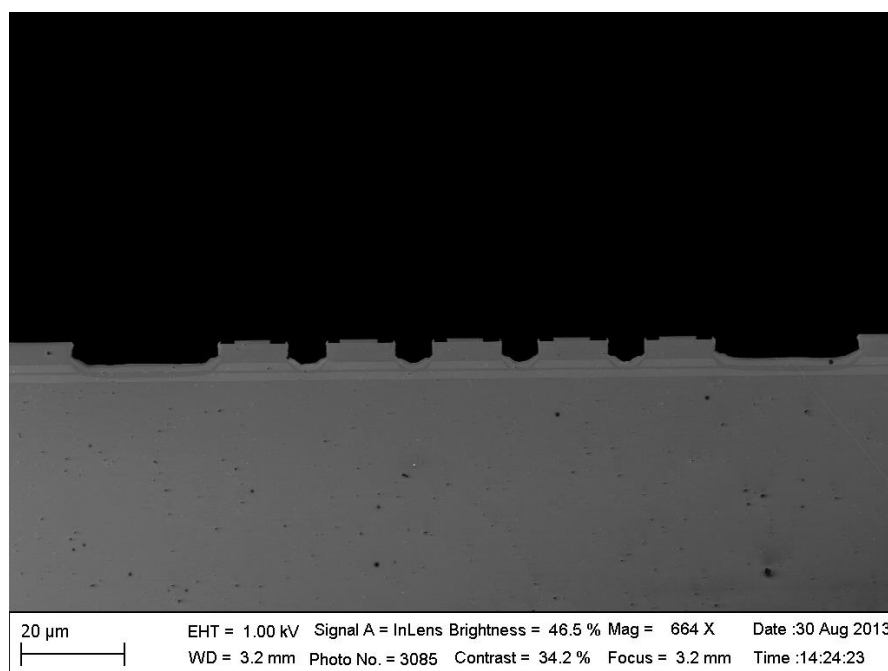
Fig. 5.12. SEMs after etch of corners of the element edges.

After the corner etch, the Si_3N_4 mask is removed by using HF (49%), and a 300 nm-thick PECVD Si_3N_4 mask was deposited and patterned for current confinement, 5 μm away from the array edges. Then, 10 nm Ti and 250 nm Au films were e-beam evaporated followed by electroplating of ~ 5 μm-thick Au. After thinning the substrate down and backside metallization (Ge/Au/Ag/Au), 4 mm-long bars were cleaved and HR coated. Laser chips were then mounted episide up on Cu submounts for testing. The cross-section SEM of a fabricated array device is shown in Fig. 5.13. It was found that

the regrown InGaAs layer was accidentally etched, within ~ 20 μm from the facets, by the metal etchant used in the cleaving vias.
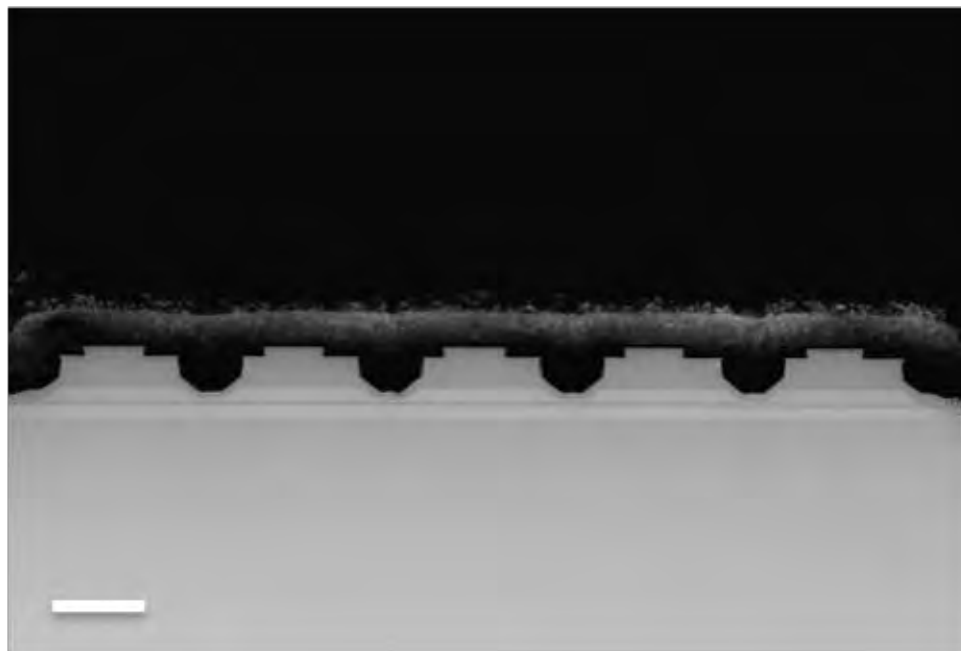
Fig. 5.13. SEM of a fabricated five-element QCL antiguided array device. Scale bar is 10 μm.

5.5 Results and Discussion

The fabricated five-element QCL antiguided arrays were tested in pulsed operation [17]. Watt-level output power in a near-diffraction-limited far-field beam was demonstrated. However, the threshold current densities for these preliminary devices were higher than expected, probably due partially to scattering caused by the inadvertent etching of the regrown InGaAs layer within 20 μm from the facets, and partially to the current spreading into interelement regions. Significant threshold-current reductions and slope-efficiency increases are expected by tightly confining the current to the element regions.

5.6 Planarized Process for Phase-Locked Antiguided QCL Arrays

To tightly confine the injection current to the element regions, the electrical resistance in the interelement regions needs to be significantly increased via, for example, proton implantation. To verify the effect of proton implantation on the electrical characteristics of strained InGaAs/AlInAs, we have grown materials with the same active region used in 8.36 μm-emitting QCL arrays, but without the InP upper cladding, and processed them into circular mesa devices with a diameter of ~ 300 μm. As can be seen from their measured current-voltage characteristics (Fig. 5.14), the voltage across the active region is substantially increased (V > 30 V at 0.2 A) after the proton implantation. However, the effect of proton implantation is completely removed, if the mesas are briefly annealed at 600 °C. Therefore, to retain the high electrical resistance, the proton implantation step needs to carried out after the selective regrowth of interelement layers in the array process. We have also developed a lithographic process to deposit a thick layer (> 10 μm) of baked photoresist on the array sample after the interelement regrowth before removing the Si_3N_4 mask, to serve as the masking layer for proton implantation (Fig. 5.15).
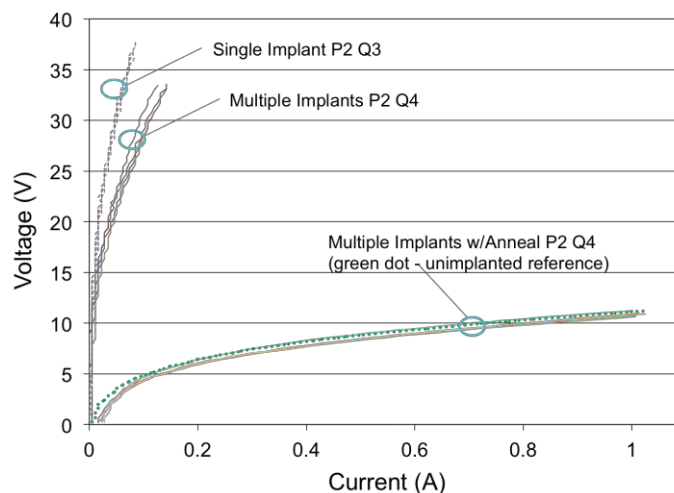
Fig. 5.14. I-V characteristics of mesas after proton implantation and thermal annealing.
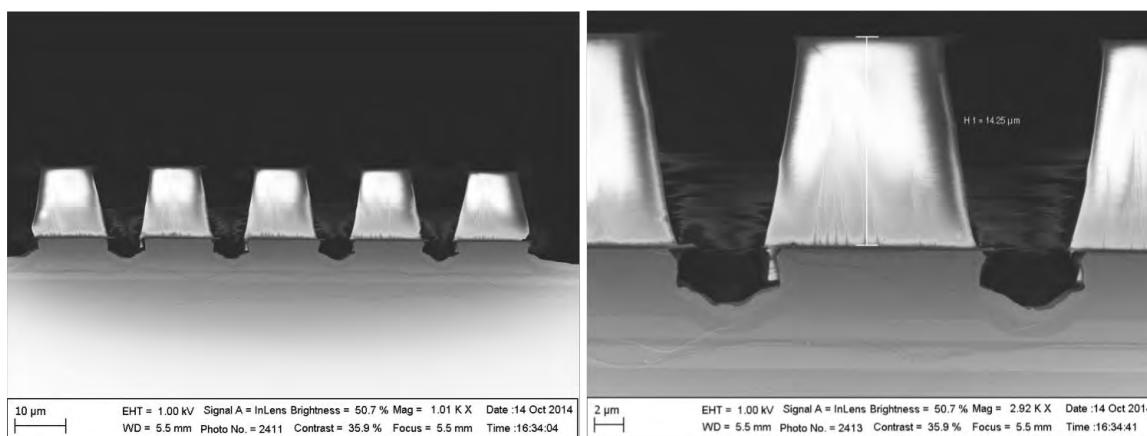
Fig. 5.15. SEMs of baked photoresist deposited on top of array samples after interelement regrowth serving as a mask layer for proton implantation process.

In addition to proton implantation, an alternative for reducing the current spreading in the interelement regions is to first etch both the upper and lower cores in the active region, and regrow semi-insulating Fe:InP in the etched trenches. To this end, we have recently developed a novel process for fabricating phase-locked anitiguided arrays of QCLs with a planar geometry. This refined fabrication process, not only addresses the problem of current spreading seen in the QCL arrays with a curved-layer geometry, but also allows for significantly improved control of the array geometry and the dimensions of element and interelement regions. As can be seen in curved-array fabrication process, in order to achieve reproducible results of selective regrowth of the interelement layers, it is imperative for the etched trenches to have a curved trench profile defined by the final wet etching using a HBr/HNO$_3$ solution. This requirement, however, makes it difficult to control the dimensions of interelement regions, which have a major impact on the performance of phase-locked antiguided arrays, as the resonance condition has to be satisfied for resonant in-phase mode operation. Moreover, the variation in the

interelement spacing also causes the slight deviations in the thicknesses of regrown interelement layers from the targeted values, and subsequently changes the refractive index profile of the arrays from their original design. These problems can be completely avoided in the newly developed process for making planarized antiguided arrays of QCLs.

The planarized process is based primarily on the non-selective regrowth of interelement layers and chemical polishing (CP). Fig. 5.16 shows the major processing steps for fabricating three-element phased-locked antiguided arrays of QCL. The base material has a similar layer structure to that depicted in section 5.4, but with the active region design reported by A. Evans et al. for the emitting wavelength of 4.6 μm. Additional thin InGaAs and InP layers were grown on top, to serve as etch stop layers in the CP steps. After defining three-element arrays in the PECVD Si_3N_4 hardmask, by using photolithography and CF_4-based RIE, the upper-core region was etched via ICP plasma etch with Cl_2-based chemistry to produce interelement trenches with vertical sidewalls. The Si_3N_4 hardmask was then removed, and ~ 4 μm-thick Fe:InP was regrown via MOCVD over the entire surface area, in order to fill the trenches. The result of nonselective regrowth of Fe:InP is shown in Fig. 5.16 (a). To ensure a planar geometry prior to the regrowth of interelement layers, a CP step, using an acetic acid/HCl solution, was utilized to polish down the overgrown Fe:InP, in order to planarize the surface. As can be seen in Fig. 5.16 (b), the CP step produced a fairly planar surface on top of element/interelement regions defined by ICP etching. After CP is completed, the interelement layers, consisting of InP/InGaAs/InP/InGaAs/InP, were non-selectively regrown, as shown in Fig. 5.16 (c). As opposed to the selective regrowth results shown

above in Fig. 5.11, here the regrown interelelment layers exhibit a very planar morphology and have uniform thicknesses over the surface polished via the CP step. Due to these smooth interelement layers, the control over the dimensions of interelement regions of final-array devices and their corresponding index profile can therefore be significantly improved.

After the regrowth of interelement layers, element regions were defined through ICP plasma etching by using Si_3N_4 as a hardmask, followed by nonselective regrowth of a 4 μm-thick InP upper cladding layer,.This is shown, after removing the nitride mask, in Fig. 5.16 (d). Finally, the second CP step was employed to polish the excess InP grown on top of interelement regions, and a heavily doped InP cap layer was grown on top for electrical contact. The completed structure of three-element, phase-locked antiguided arrays of QCLs based on this planarized process is shown in Fig. 5.17.
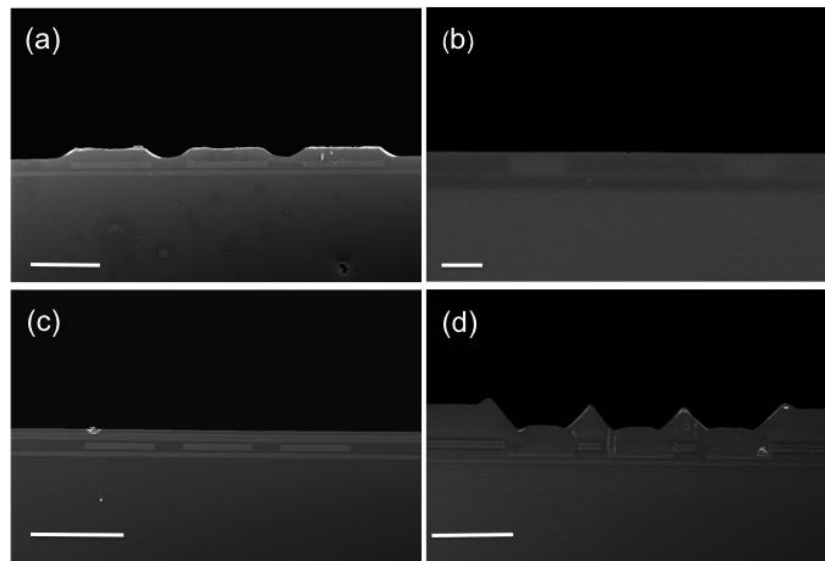
Figure 5.16. Cross-section SEM images of planarized process steps after (a) Fe:InP regrowth; (b) CP; (c) interelement layer regrowth; and (d) regrowth of InP cladding layer. The scale bars are (a) 10 μm, (b) 2μm, (c) 10 μm, and (d) 10 μm.
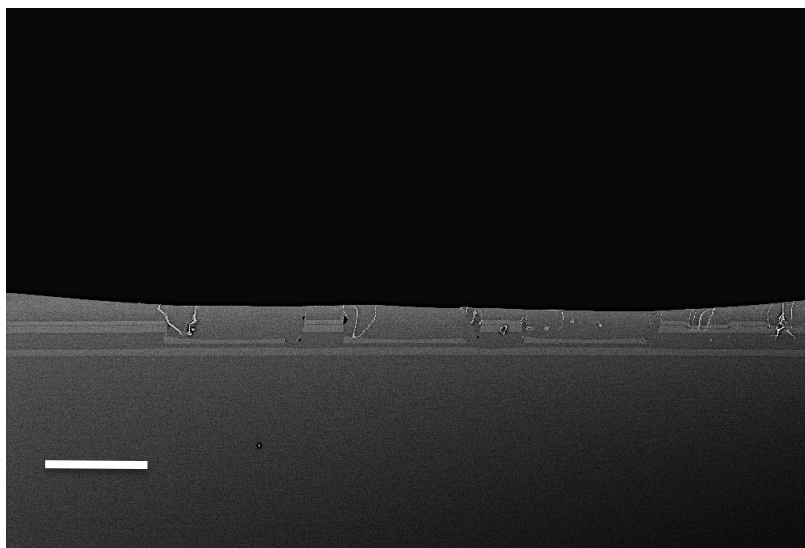
Figure 5.17. Cross-section SEM image of a completed structure of three-element, phase-locked antiguided array of QCLs based on planarized process. The scale bar is 10 μm.

Based on the planarized process described above, we have recently completed the fabrication of our first three-element APC QCL antiguided array devices for λ = 4.6 μm, as show in Fig. 5.18. These completed APC QCL array devices possess an overall good surface planarity. In order to further improve the planarity of future APC devices, we have designed a new photomask for defining APC interelement regions, in which the 25 μm-wide trenches on both sides of arrays are eliminated. Thus, the core materials between arrays would be completely removed during the ICP etch step and refilled by the regrown Fe:InP. We have processed a quarter of APC base material using this new photomask with the modified three-element array design. As shown in Fig. 5.19, by removing 25 μm-wide trenches on both sides of arrays, the surface morphology between arrays after the Fe:InP regrowth is essentially planar. More importantly, the field between

arrays is basically as high as the array regions. This ensures that the array-regions have a better contact with the polishing pad during the CP step, and therefore lead to more uniform polishing over the entire sample area, which can be seen in Fig. 5.20.
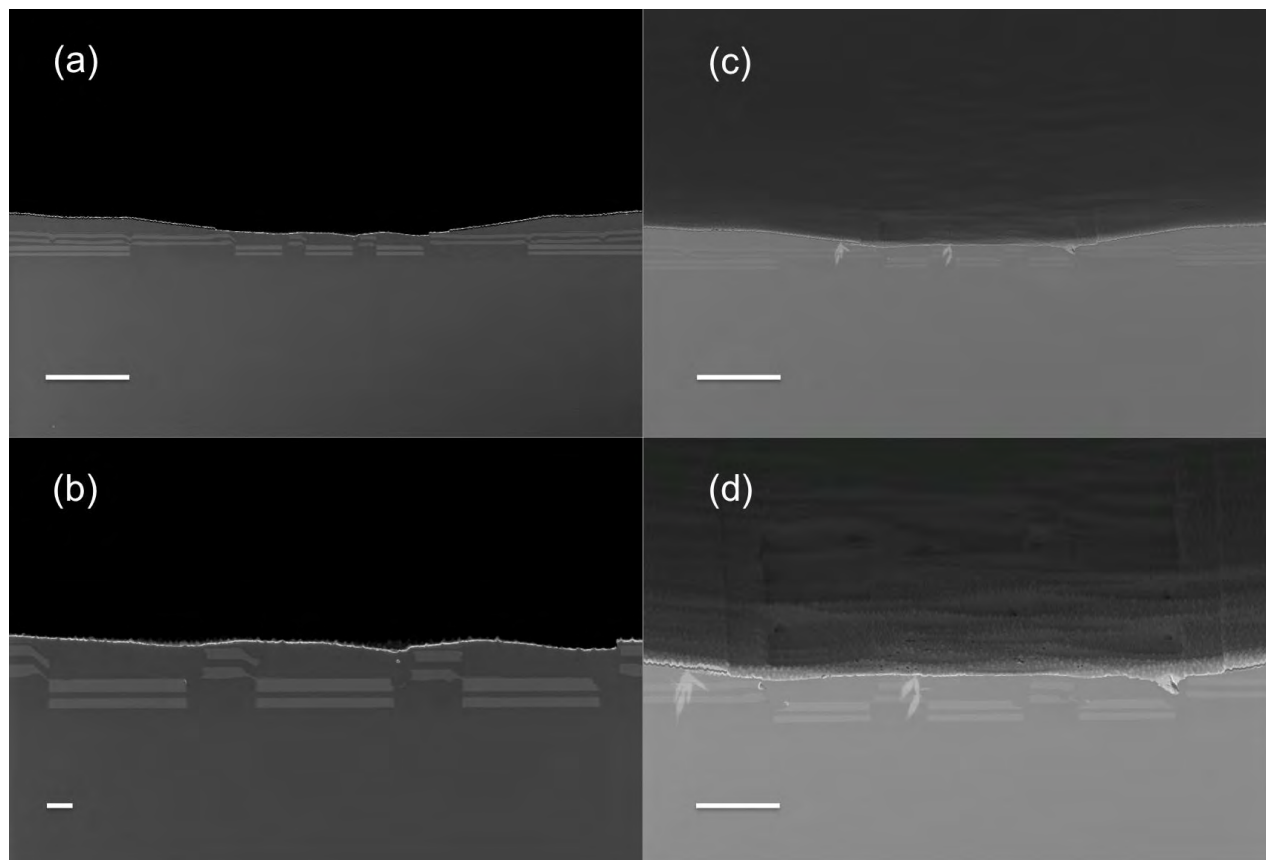
Figure 5.18. SEM images of fabricated three-element, phase-locked antiguided arrays of QCLs based on planarized process. The scale bars are (a) 20 μm; (b) 2 μm; (c) 20 μm; and (d) 10 μm.
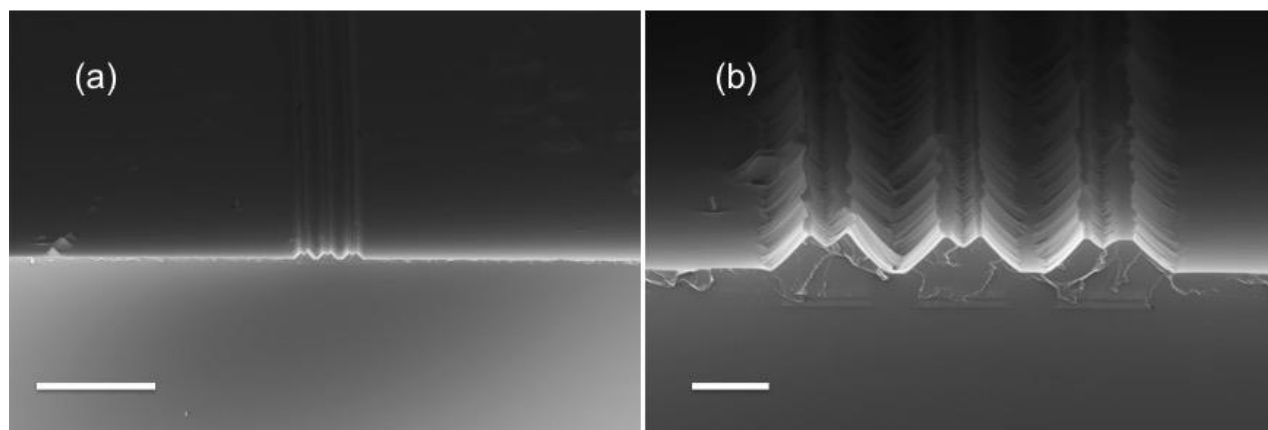
Figure 5.19. SEM images of APC base material after ICP etch and Fe:InP non-selective regrowth using modified array design. The scale bars are (a) 20 μm; and (b) 10 μm.
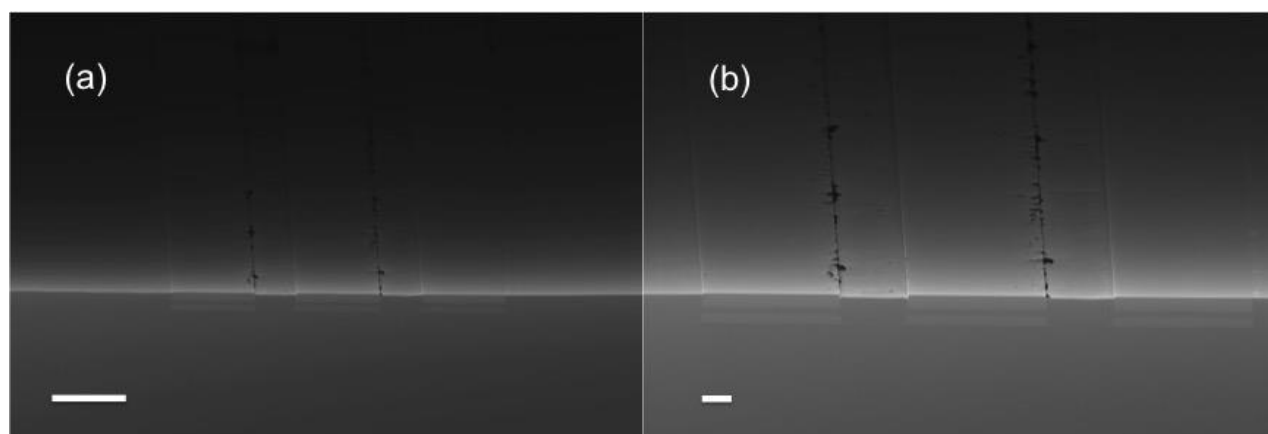
Figure 5.20. SEM images of APC base material after Fe:InP non-selective regrowth and CP using modified array design. The scale bars are (a) 10 μm; and (b) 2 μm.

We have tested our first batch of APC array devices under pulsed operation at room temperature. Unfortunately, we did not observe any electroluminescence or lasing from these devices regardless of the drive currents. Prior to the growth of APC base material, we grew two batches of full QC-laser structure with identical laser core as the APC material. These materials were processed into 21 μm-wide ridge lasers, and the devices from both materials have shown good lasing characteristics. One possible reason that no light emission is observed from our fabricated APC devices is the degradation of the core material during the device fabrication. As pointed out by Semtsiv et al. [18], the strain-compensated QCL cores, especially when containing high-strain materials such as AlAs layers, have relatively poor thermal stability, in that they are likely to relax during the post-growth high-temperature processes. To avoid crystal relaxation from post-growth annealing, they employed gas-source molecular beam epitaxy (GSMBE) to selectively regrow Fe:InP at a low growth temperature of 550 °C for buried-heterostructure (BH) QCLs. During our APC device fabrication, despite having a nominally low value of net strain in each QC-stage, the core material had undergone several prolonged annealing steps at temperatures higher than 600 °C. Specifically, these steps include the regrowth of 5 μm-thick Fe:InP, the regrowth of multiple interelement layer, the regrowth of 5 μm-thick n-doped InP cladding, and the regrowth of n-doped InP cap layer. Owing to a relatively slow growth rate of InP via MOCVD, the APC core materials were essentially annealed at high temperature for several hours during each regrowth step.

In an attempt to examine the thermal effect of these regrowth steps on the crystal quality of APC base materials, we have conceived a simple process for making BH ridge lasers which mimics the actual APC device fabrication process. As can be seen in Fig. 5.21, 8

μm-wide ridges are first formed in the APC core material via ICP etch using SiNx etch hardmask. Then, the dielectric hardmask is removed and 5 μm-thick Fe:InP was non-selectively regrown to bury the etched ridges. After CP to planarize the surface, the sample is annealed in the MOVCD reactor for the same growth time at same temperature, but without growing the APC interelement layers. After the annealing, a 5 μm-thick n-doped InP cladding layer is regrown followed by the regrowth of n-doped InP cap layer. A 350 nm-thick SiNx layer is then deposited via PECVD for current confinement, and a 4 μm-wide contact window is lithographically defined and etched via reactive-ion etching. Finally, the epi-side is metallized with Ti/Au using e-beam evaporation. For comparison, another sample will also be regrown and processed in parallel, which will be only subjected to the annealing during the regrowth of 5 μm-thick n-doped InP cladding as well as the cap layer. After the regrowth is completed, the material is processed into laser devices based on our typical laser ridge process. The fabricated devices from this material can serve as reference devices, since from our past experiences, the conventional QCL core materials are not affected when only subjected to the annealing during the regrowth of n-InP cladding and cap layers. By comparing the measured L-I-V characteristics of devices from both materials, the thermal effect on the core material can be extracted.
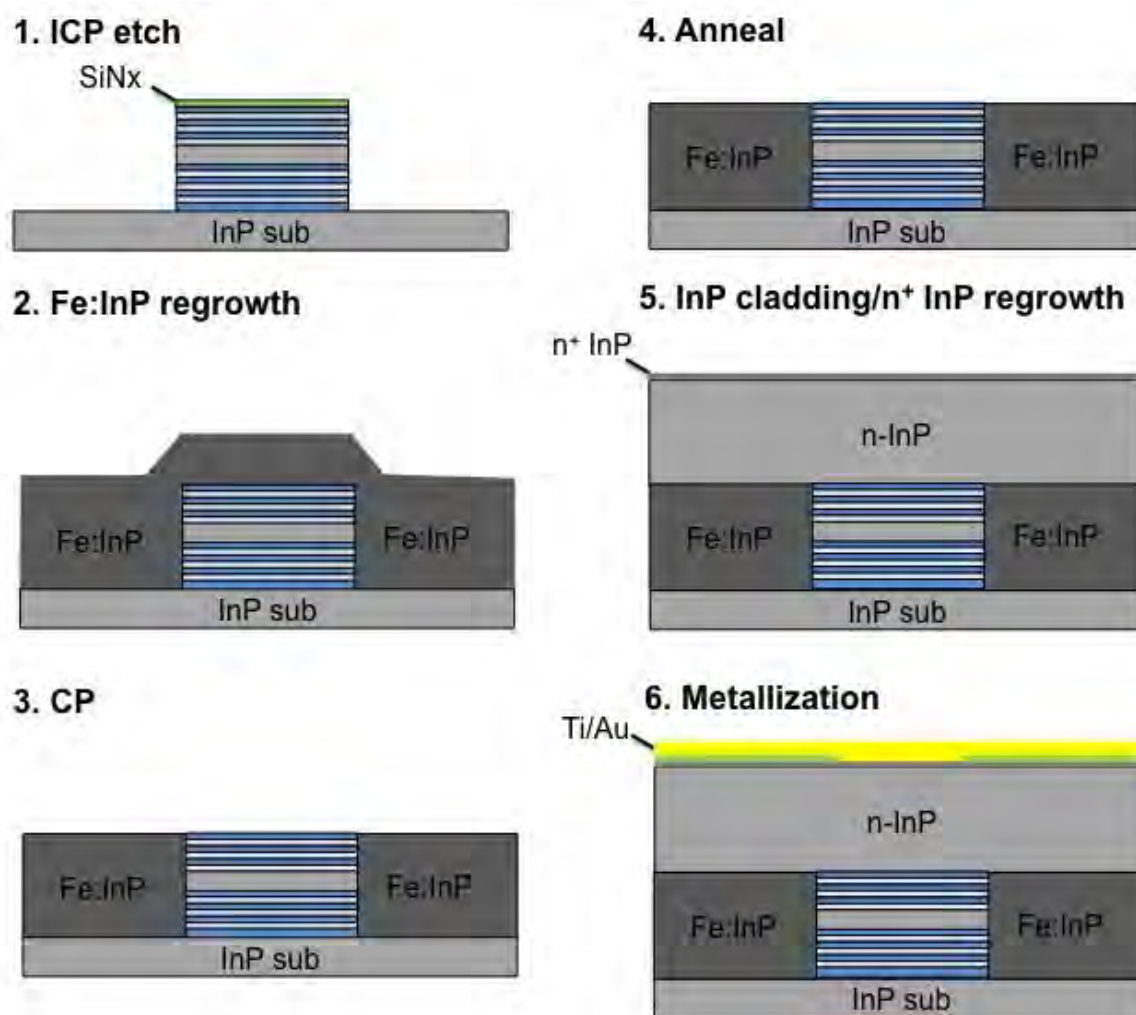
Figure 5.21. A simple BH ridge laser process for examining the thermal stability of APC base material.

In addition, instead of having a sharp turn-on voltage, the measured current-voltage (I-V) characteristic of these APC devices, as can be seen in Fig. 5.22, shows a roughly linear dependence of the voltage on the injection current up to ~ 20 A, resembling the behavior of a resistor. The observed linear I-V characteristic suggests that the regrown Fe:InP is by no means resistive, and there are severe shunt-current paths around the element regions of fabricated APC devices. Besides the potential leakage paths along the etched sidewall of interelement trenches, it is highly likely that the resistivity of regrown Fe:InP was significantly reduced or even removed during the subsequent regrowth steps in the APC process. It has been experimentally demonstrated [19] that the resistivity of as-grown Fe:InP is significantly influenced by the post-growth annealing at high temperatures (600 -900°C), and it depends highly on the annealing conditions, including the annealing temperature, annealing time, ambience, and the cooling method. To identify the root cause of the formation of shunt-current paths seen in our APC devices, we have grown n-doped InP cap/Fe:InP structures on n-InP substrates. These materials will first be subjected to thermal annealing in MOCVD reactor under several annealing conditions, and will then be processed into standard 300 μm-wide circular mesa devices. By measuring the I-V characteristic of these mesa devices, it will be clearer how the thermal annealing affects the resistivity of our regrown Fe:InP. This test result would thus allow us to refine the existing APC fabrication process accordingly.
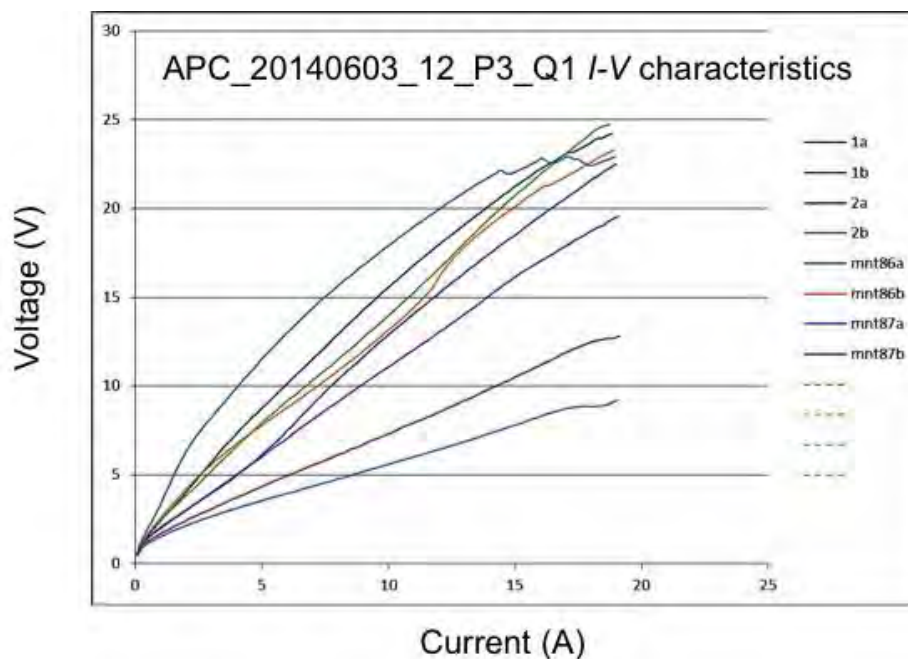
Figure 5.22. *I-V* characteristics of fabricated APC QCL-array devices.

5.7 Conclusion

A novel fabrication process for on-chip resonant leaky-wave coupling of quantum cascade lasers (QCLs) has been developed by selective regrowth of interelement layers in curved trenches, defined by dry and wet etching. The fabricated structure provides a large index step between antiguided-array element and interelement regions. A refined fabrication process has also been developed to produce phased-locked antiguided arrays of QCLs with planar geometry. The main fabrication steps in this process include non-selective regrowth of Fe:InP in interelement trenches, defined by inductive-coupled plasma (ICP) etching, a chemical polishing (CP) step to planarize the surface, non-selective regrowth of interelement layers, ICP selective etching of interelement layers, and non-selective regrowth of InP cladding layer followed by another CP step to form the

element regions. This new process results in planar interelement regions, which allows for significantly improved control over the array geometry and the dimensions of element and interelement regions. Such a planar process is highly desirable for the realization of 4.5-5.0 μm-emitting QCL antiguided arrays, where fabrication tolerances for single-mode operation are tighter compared to longer wavelengths in the infrared.

Reference

[1] D. Botez and D. R. Scifres. "*Diode Laser Arrays*", Cambridge University Press (1994).

[2] D. Botez, L. J. Mawst, G. Peterson, and T. J. Roth. "Phase-locked arrays of antiguides: modal content and discrimination", *IEEE J. Quantum Electron.*, **26**, 482-495 (1990).

[3] L. J. Mawst, D. Botez, T. J. Roth, G. Peterson, and J. J. Yang. "Diffraction-coupled, phase-locked arrays of antiguided, quantum-well lasers grown by metalorganic chemical vapor deposition", *Electron. Lett.*, **24**, 958-959 (1988).

[4] D. Botez, L. J. Mawst, G. Peterson, and T. J. Roth. "Resonant optical transmission and coupling in phase-locked diode laser arrays of antiguides: The resonant optical waveguide array", *Appl. Phys. Lett*, **54**, 2183-2185 (1989).

[5] L. J. Mawst, D. Botez, T. J. Roth, and G. Peterson. "High-power, in-phase-mode operation from resonant phase-locked arrays of antiguided diode lasers", *Appl. Phys. Lett*, **55**, 10-12 (1989).

[6] D. Botez, M. Jansen, L. J. Mawst, G. Peterson, and T. J. Roth. "Watt-range, coherent, uniphase powers from phase-locked arrays of antiguided diode lasers", *Appl. Phys. Lett*, **58**, 2070-2072 (1991).

[7] C. Zmudzinski, D. Botez, L. J. Mawst, C. Tu, and L. Frantz. "Coherent 1 W continuous wave operation of large-aperture resonant arrays of antiguided diode lasers", *Appl. Phys. Lett*, **62**, 2914-2916 (1993).

[8] H. Yang, L. J. Mawst, M. Nesnidal, J. Lopez, A. Bhattacharya, and D. Botez. "10W near-diffraction-limited peak pulsed power from Al-free, 0.98 μm-emitting phase-locked antiguided arrays", *Electron. Lett.*, **33**, 136-137 (1997).

[9] H. Yang, L. J. Mawst, and D. Botez. "1.6 W continuous-wave coherent power from large-index-step (Δn ≈ 0.1) near-resonant, antiguided diode laser arrays", *Appl. Phys. Lett*, **76**, 1219-1221 (2000).

[10] I. Vurgaftman and J. R. Meyer. "Photonic-crystal distributed-feedback lasers", *Appl. Phys. Lett*, **78**, 1475-1477 (2001).

[11] Y. Bai, S. R. Darvish, S. Slivken, P. Sung, J. Nguyen, A. Evans, W. Zhang, and M. Razeghi. "Electrically pumped photonic crystal distributed feedback quantum cascade lasers", *Appl. Phys. Lett*, **91**, 141123 (2007).

[12] Y. Bai, B. Gokden, S. R. Darvish, S. Slivken, and M. Razeghi. "Photonic crystal distributed feedback quantum cascade lasers with 12 W output power", *Appl. Phys. Lett*, **95**, 031105 (2009).

[13] P. Rauter, S. Menzel, A. K. Goyal, B. Gokden, C. A. Wang, A. Sanchez, G. W. Turner, and F. Capasso. "Master-oscillator power-amplifier quantum cascade laser array", *Appl. Phys. Lett*, **101**, 261117 (2012).

[14] A. Lyakh, R. Maulini, A. Tsekoun, R. Go, and C. Kumar N. Patel. "Continuous wave operation of buried heterostructure 4.6 μm quantum cascade laser Y-junctions and tree arrays", *Opt. Express*, **22**, 1203 (2014).

[15] G. M. de Naurois, M. Carras, B. Simozrag, O. Patard, F. Alexandre, and X. Marcadet. "Coherent quantum cascade laser micro-stripe arrays", *AIP Adv.*, **1**, 032165 (2011).

[16] Z. Liu, D. Wasserman, S. S. Howard, A. J. Hoffman, C. F. Gmachl, X. Wang, T. Tanbun-Ek, L. Cheng, and F.-S. Choa. "Room-temperature continuous-wave quantum cascade lasers grown by MOCVD without lateral regrowth", *IEEE Photon. Technol. Lett.*, **18**, 1347-1349 (2006).

[17] J. D. Kirch, C.-C. Chang, C. Boyle, L. J. Mawst, D. Lindberg III, T. Earles, and D. Botez. "5.5 W near-diffraction-limited power from resonant leaky-wave coupled phase-locked arrays of quantum cascade lasers", *Appl. Phys. Lett.*, **106**, 061113 (2015).

[18] M. P. Semtsiv, A. Aleksandrova, M. Elagin, G. Monastyrskyi, J.-F. Kischkat, Y. V. Flores, and W. T. Masselink. "Semi-insulating InP:Fe for buried-heterostructure strain-compensated quantum-cascade lasers grown by gas-source molecular-beam epitaxy", *J. Cryst. Growth*, **378**, 125-128 (2013).

[19] R. Fomari, A. Zappettini, E. Gombia, R. Mosca, K. Cherkaoui, and G. Marrakchi. "Conductivity conversion of lightly Fe-doped InP induced by thermal annealing: A method for semi-insulating material production", *J. Appl. Phys.*, **81**, 7604-7611 (1997).

CHAPTER SIX

NANOPATTERNING FOR INTERSUBBAND QUANTUM BOX SEMICONDUCTOR LASERS

6.1 Intersubband Quantum Box (IQB) Lasers

Quantum cascade lasers (QCLs) are semiconductor lasers based on intersubband transitions between two electronic quantized states in a multiple quantum well structure. The electron lifetime in the upper state, and hence the radiative transition efficiency, are influenced by other carrier scattering mechanisms, such as optical phonon scattering, acoustic phonon scattering, impurity scattering, electron-electron scattering, and interface roughness scattering. In particular, for mid-infrared (mid-IR) QCLs at room temperature, the scattering of electrons via emission and absorption of longitudinal optical (LO) phonons is the dominant scattering process. The lifetime for electrons in the upper state due to LO phonon scattering is typically on the order of picoseconds. In contrast, the radiative relaxation time for electrons in the excited states is on the order of nanosecond, that is, three orders of magnitude greater than that for non-radiative LO phonon scattering processes. As a result, due to the fast LO phonon scattering rate, the radiative transition efficiency of mid-IR QCLs is inherently limited, which, in turn, results in a low overall wallplug efficiency. In order to compensate for the low radiative efficiency by increasing the optical gain, the active region of mid-IR QCL structures usually consists of a stack of radiative stages (typical number of stages $N \sim 30 - 40$) in a cascaded scheme, where one electron is designed to contribute to N photon emissions. Unfortunately, the improved

optical gain achieved in the cascaded scheme of QCLs comes at the expense of much higher operating voltage. This fundamentally prevents mid-IR QCL devices from achieving high wallplug efficiencies, especially under continuous-wave (CW) operation at room temperature.

In the early theoretical studies [1-2], it has been shown that the non-radiative LO phonon scattering rate is significantly reduced in lower dimensional quantum-confined structures, such as quantum wires and quantum dots. In quantum-well based structures, electrons are confined only in the crystal growth direction. In the plane of quantum well layers, on the other hand, they behave like free electrons and have a continuous energy dispersion relationship. Electron energies are characterized by a series of discrete nearly parabolic sub-bands in the conduction band. Therefore, electrons can be easily scattered between sub-bands via LO phonon scattering processes, provided the condition of energy and momentum conservation are satisfied. For quantum dots, due to the additional quantum confinements, electron energy spectrum is fully quantized into discrete energy levels similar to atomic states. Thus, unless the energy difference between two discrete levels exactly matches the energy of an LO phonon, the electron relaxation by single phonon scattering process is inhibited. Electron relaxation can proceed instead by multi-phonon scattering processes. The reduction in electron relaxation rate in quantum dots due to the inefficient phonon scattering is often referred to as phonon bottleneck effect.

The existence of phonon bottleneck effect was however controversial. For transition energies close to an LO phonon energy ($\sim$ 40 meV), the reduction in electron relaxation rate in quantum dots was indeed observed in the experiments [3]. In self-assembled InAs/GaAs quantum dots, for example, electron relaxation was investigated using far-

infrared pump-probe spectroscopy, and the corresponding electron lifetime was found to be tens of picoseconds. The experimental results also showed a monotonic increase in electron lifetime with transition energy, from ~ 20 ps at 40 meV to the maximum of ~ 65 ps at ~ 53 meV. The electron lifetime decreases instead as the transition energy exceeds 53 meV. In another experiment reported by Mukai et al. [4], carrier dynamics in self-formed InGaAs/GaAs quantum dots grown by atomic layer epitaxy were characterized by using electroluminescence and temperature dependent time-resolved photoluminescence (PL) in the near-IR region. The authors claimed that the phonon bottleneck does exist, as the measured carrier relaxation lifetime (~ 1 ns) is comparable to the measured radiative recombination lifetime even at 300 K. On the contrary, the results of some other experimental works indicated little evidence for the existence of a significant phonon bottleneck effect in quantum dots. For example, Wang et al. [5] also performed the optical characterization of strained InGaAs/GaAs quantum dots using temperature dependent time-resolved PL. Despite an increased carrier lifetime by a factor of ~ 2 in quantum dots was observed as compared to that in quantum wells at low temperature, the integrated PL efficiency of quantum dots was comparable to that of quantum wells. This finding cannot be successfully explained by the phonon bottleneck effect, as the PL efficiency should have otherwise been lower in quantum dots under the presence of the phonon bottleneck.

It is clear that the role of electron-phonon scattering in electron relaxation processes in quantum dots needs to be theoretically re-examined to account for the discrepancy found in the experiments. Recently, it has been pointed out [6-7] that the interaction between electrons and phonons in quantum dots is not in the weak-coupling regime, and thus

cannot simply be treated within the semi-classical perturbative framework using Fermi's golden rule. Instead, the discrete natures of electronic excitations in the quantum dots are strongly coupled to the confined LO-phonon modes, and thus form the quasi-particle states called polarons. This strong coupling leads to the repeated energy exchange between electrons and phonons (i.e. Rabi oscillation), in the absence of any energy dissipation mechanisms. This, in turn, would result in significantly increased electron lifetime as compared to that in bulk or quantum well systems (~ 1 ps). However, in reality, the confined LO-phonon modes experience anharmonic decay into bulk acoustic phonon modes. Due to the instability of confined LO-phonon modes, the polarons decay rapidly shortly after their formation, and the energy of electrons is eventually dissipated through the LO phonons. Therefore, the decay time of polarons, on the order of several tens of picoseconds, provides a lower limit of the duration of phonon bottleneck before it is removed over a wide range of energy detuned from the LO-phonon energy.

The theoretical prediction of electron lifetimes in quantum dots based on this strong coupling model appears to agree with the experimental data. Specifically, the calculated polaron disintegration rate, and the corresponding polaron decay time in InAs/GaAs quantum dots depend highly on the polaron energy in the proximity of LO-phonon energy (~40 meV) [8]. For energy higher than the LO-phonon energy, the polaron decay time increases slowly with increasing energy and reaches a maximum value of ~ 80 ps at ~ 55 meV. The decay time, however, decreases as energies further increases. For low energy polarons, in particular for energy below 30 meV (< ~ 7.2 THz), the polaron decay time increases much faster with increasing detuning from the phonon energy. The substantially prolonged polaron decay time predicted in the terahertz range was

experimentally demonstrated in 2009 by Zibik et al. [9], where the measured decay time at 14 meV (~ 3.4 THz) is as high as 1.5 ns at $T = 10$ K, that is, three orders of magnitude higher than that in the quantum well-based systems. Moreover, the long decay time indeed decreases very rapidly with decreasing detuning towards higher energy side, having a value of ~ 2 ps at 30 meV (~ 7.2 THz).

The demonstrated long carrier relaxation time in self-assembled quantum dots is an important step forward towards the realization of high wallplug-efficiency mid-IR and especially terahertz (THz) intersubband semiconductor lasers. First, by using lower dimensional structures (i.e., quantum wires, quantum dots, nanopillars, etc.) in the active region rather than quantum wells, the carrier lifetime in the upper laser state is greatly enhanced, so that the population inversion can be established more easily, which would in turn require less injection current to reach the laser threshold. Furthermore, the optical gain per radiative stage is expected to be higher. This would eliminate the need for using multiple stages seen in typical QCL devices, and hence significantly reduce the operating voltage. With both reduced threshold current and operating voltage, the requirement of input power for these novel lasers is therefore lower, and much higher wallplug efficiency (> 30%) under CW operation at room temperature becomes possible.

Intersubband quantum box (IQB) semiconductor lasers for the mid- and far-infrared wavelengths ($\lambda \sim 3-10$ μm) have been proposed by Botez [10] and Hsu et al. [11]. The active region of proposed devices is composed of two-dimensional array of quantum box ministacks, called "active boxes", separated by current-blocking material (CBM) such as semi-insulating InP, as shown in Fig. 6.1. Each ministack consists of 2 to 4 QBs, sequentially arranged like the stages in the QCL structure. These ministacks of QBs with

low-doped, n-type InP layers constitute the core of optical waveguide, sandwiched between two heavily doped, n-type InP cladding layers. From simulation, for 4-QB-stack devices, the projected CW wallplug efficiency at room temperature is as high as 50% at $\sim$ 15 times threshold ($J_{th} \sim 0.1$ KA/cm^2), with a much lower operating voltage of < 1.7 V compared to that of typical mid-IR QCL devices (11- 12 V). In spite of this encouraging prediction, according to the strong-coupling model mentioned earlier, at these wavelengths, the corresponding transition energies ($\sim$100– 400 meV) are far detuned from the LO-phonon energy, where the phonon bottleneck effect is completely removed due to the rapid decay of polarons into other acoustic phonon modes. Thus far, progresses have been made by Tsvid. et al. [12] and Botez et al. [13] in device fabrication. The electroluminescence results at 80 K from IQB structures were also reported by Botez et al. [14]. On the other hand, in the THz region, the demonstrated long carrier lifetime in quantum dots have shown great promises for the realization of quantum-dot based THz lasers. The performance of quantum well-based THz QCLs has been greatly improved over the past years due to better active region designs and waveguide structures. Unfortunately, to date, the highest operating temperature for THz QCLs is still below 200 K, without resorting to the assistance of external magnetic field or nonlinear optical processes such as difference frequency generation. It is believed that room-temperature operation of THz QCLs will probably require the incorporation of lower dimensional structures like quantum dots or nanopillars as their active regions [15].
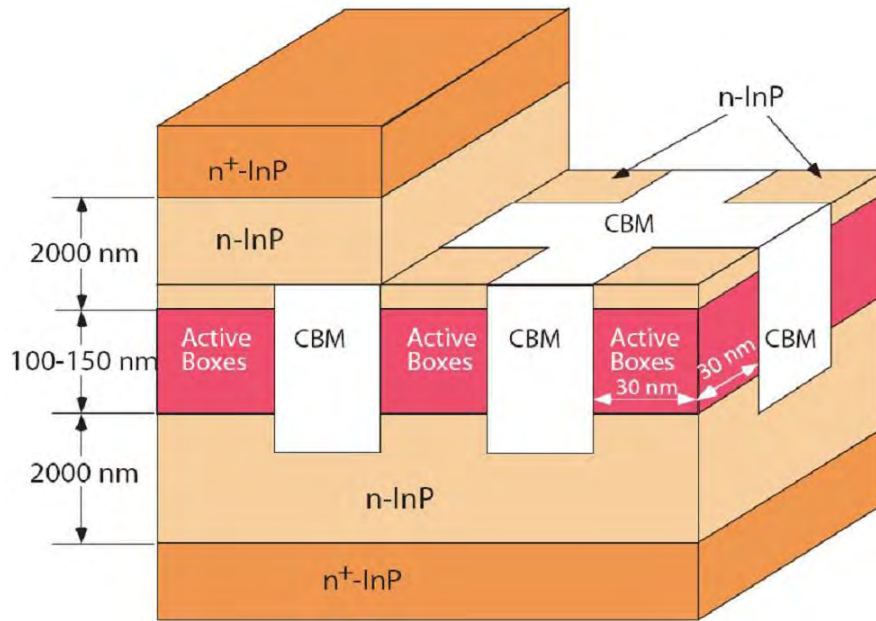
Figure 6.1. A schematic of the IQB laser structures. CBM is current blocking materials.

6.2 Fabrication of the Active Region of IQB Lasers

In principle, the active region of IQB lasers emitting at the mid-IR wavelengths can be realized by either bottom-up or top-down approach. In bottom-up method, low-dimensional structures such as quantum dots or quantum dashes are incorporated in the surrounding heterostructures by epitaxial growths. Wasserman et al. [16] have observed mid-IR electroluminescence from self-assembled InAs quantum dots grown in AlGaAs/GaAs hetereostructures at 77 K. In their experiment, multiple emission peaks were observed, and the light emission is orthogonally polarized in the growth plane, suggesting the anisotropy in the shape of InAs quantum dots. Fischer et al. [17] also reported intersubband electroluminescence at $\lambda = 22$ μm (57meV; TE-polarized), corresponding to the transition from first excited state to the ground state, in the self-assembled $In_{0.4}Ga_{0.6}As/GaAs$ quantum dots embedded in a quantum cascade

heterostructure. However, a relatively broad emission peak is also observed at higher energy (~ 115 meV), which is attributed to the undesirable transition from the wetting layer to the ground state of the quantum dots. The total power emitted from 22 μm-peak is 0.7 nW, which constitutes merely ~ 0.8% of the total integrated output power. The top-down approach, on the other hand, mainly involves the definition of quantum dots or boxes by lithography, pattern transfer into underlying quantum cascade layer structures by plasma etching, and planarization either by epitaxial regrowth of current blocking materials or by spin-on coating of low-loss polyimide. In this method, both the size and geometry of quantum dots/boxes can be precisely controlled during the lithographic step, thus allowing for tight confinement of the electrons. In addition, the emission wavelength of the resulting IQB lasers can also be designed at will by properly engineering the energies of subbands in the quantum dots/boxes.

The top-down approach requires high-resolution lithographic techniques to pattern arrays of high-density, nanometer-sized features over a millimeter-sized area. Conventional electron-beam (e-beam) lithography can routinely define features of 20 nm or smaller. However, since the e-beam exposure is done in a serial fashion, it is not a suitable technique for patterning over a large surface area. Nanoimprint lithography (NIL), on the other hand, enables patterning nanometer-sized features over a large area, by mechanically pressing the pre-patterned stamps into polymeric materials. However, in the imprint process there are several issues that need to be carefully addressed, such as the alignment between the stamps and the substrates, the amount of defects on the stamps, and the release of the stamps from the substrates after printing. Other lithographic methods, such as colloidal lithography or using anodic-aluminum oxide as

templates, have also been used for patterning of nanostructures over a large area. The smallest feature sizes that can be achieved by these approaches are typically a few hundreds of nanometers or larger.

In this chapter, a robust process to fabricate Ni etching hardmask for the fabrication of IQB lasers by using self-assembled block copolymer (BCP) templates and electrodeposition is presented. In the demonstrated process, PS-b-PMMA diblock copolymers were first self-assembled on heavily doped, n-type GaAs substrates. After selectively removing the PMMA cylinders, Ni was electroplated into the ~25nm-wide holes in the remaining PS template. Following the Ni electrodeposition, the PS template was removed by O_2-plasma reactive-ion etching (RIE), leaving behind an ultra-dense, large-area Ni nanopillar array on the substrate. The demonstrated process based on BCP lithography and metal electrodeposition provides a simple method for nano-patterning over a large area required for the realization of IQB lasers.

6.3 Metallic Nanostructures Fabricated by BCP Lithography

The self-assembled block copolymer (BCP) has emerged as a promising candidate for patterning features at sub-100 nanometer (nm) scales [18-19]. Other patterning techniques such as electron-beam (e-beam) and nanoimprint lithography can suffer from low throughput or are limited to a small area. BCP lithography serves as a rapid and cost-effective alternative for nanofabrication at full-wafer scale. In the past decade, functional nanostructures fabricated based on BCP lithography have shown a wide variety of applications, including bit-patterned media, surface enhanced Raman spectroscopy, photonic band gap materials, and III-V semiconductor quantum dots [20].

To make metallic nanostructures with BCP templates, the process typically begins with a metal film of interest sputtered on a host substrate. A BCP template is prepared on top of the film to serve as the etch mask. Reactive-ion etching (RIE) or ion-milling step [21] is employed to transfer patterns into the metal. The main fabrication steps in this process are illustrated in Fig. 6.2. This approach, however, often experiences the difficulty of inherent low metal-etch rate, and hence poor etch selectivity with respect to the metal, leading to a low fidelity of pattern transfer. As a result, high-aspect-ratio structures are difficult to achieve when using this direct pattern-transfer scheme.
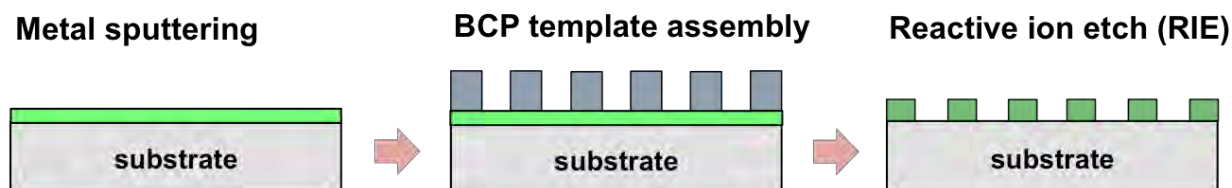
Figure 6.2. Schematic of the main fabrication steps for metallic nanostructures by using BCP templates and metal reactive-ion etching.

One method that has been widely used to address the problem seen in the above process is based on the metal liftoff process. As shown in Fig. 6.3, in this approach, a BCP template is first introduced on a host substrate. Then, a thin layer of metal is evaporated onto the template and lifted off to leave the desired pattern [22]. This self-assembled BCP liftoff process has recently been employed to demonstrate metal-nanodot memory devices on silicon (Si) substrates [23]; yet, in order to completely remove the BCP template, the metal-liftoff step often entails the use of an aggressive chemical treatment at an elevated temperature; for example, the use of heated 'piranha' solutions. The thickness of the

metal structure is also typically limited to a fraction of the polymer thickness. As a result, it is difficult to incorporate this process into conventional compound-semiconductor device manufacturing for optoelectronics applications.

BCP template preparation   **Metal evaporation**   **Liftoff**
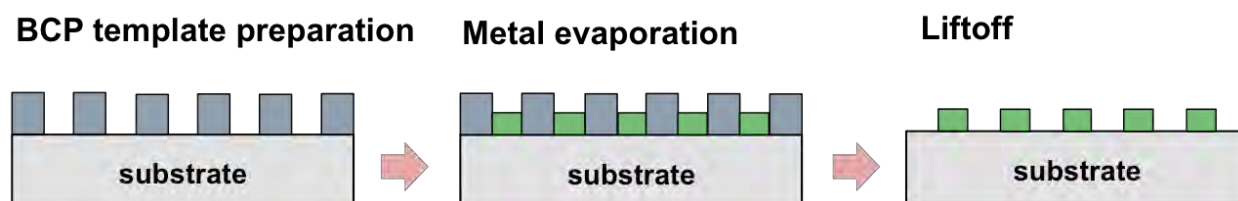
Figure 6.3. Schematic of the main fabrication steps for metallic nanostructures by using BCP templates and metal liftoff.

To address the problems described above, we present a new fabrication process for making large-area, ultra-dense nickel (Ni) nanopillar arrays on gallium arsenide (GaAs) substrates by Ni electrodeposition using poly(styrene-block-methyl methacrylate) (PS-b-PMMA) diblock copolymer lithography. With the cylinder-forming PS-b-PMMA BCP as a template, the fabricated two-dimensional Ni nanopillar arrays exhibit a fundamental hexagonal symmetry, a high pillar density of $\sim 10^{11}/cm^2$, and a uniform size of ~24 nm in diameter or smaller over an entire employed area of $\sim$ 1 cm $\times$ 1 cm of GaAs substrate. Although considerable research has been devoted to similar template-based, bottom-up approaches to fabricating sub-50 nm metal nanodot or nano-hole-arrays, little work has been reported on the realization of metallic nanostructures with a comparable feature size and dot (or hole) density uniformly across an area of a square centimeter or larger on III-V semiconductor substrates. The present work represents the realization of large-area, highly dense sub-30 nm metal nanopillar arrays on III-V semiconductor substrates.

Furthermore, electrodeposition processes typically require that the host substrate be metalized prior to the formation of templates. However, Scheck *et al*. [24] have shown that metal electrodeposition can be initiated directly on n-doped GaAs surfaces (n~ 7×10^{17} cm^{-3}) after an applied voltage exceeds a threshold value. For the process described here, Ni was electrodeposited, into the nanoscale holes of a PS template, directly onto bare GaAs substrates. Therefore, by eliminating conductive seed layers, this *seedless* electrodeposition, in combination with BCP lithography process, opens up an effective route to manufacture highly dense, sub-50 nm metal nanostructures at a full-wafer scale, and provides considerable fabrication latitude for further integration with III-V optoelectronic devices to enhance their performance and functionalities.

6.4 Fabrication Process

The details of the fabrication process for our Ni nanopillar arrays are summarized in Figure 6.4. A 3-inch, Si-doped GaAs (100) wafer with a carrier concentration of 10^{18} cm^{-3} was first spin-coated with a random copolymer consisting of polystyrene-polymethyl methacrylate (PS-r-PMMA) . This cross-linkable random copolymer, referred to as a "brush layer", was ~ 6 nm thick, and provided a non-preferential affinity to both block types of the cylinder-forming diblock copolymer PS-b-PMMA. This brush is essential to the formation of cylindrical domains perpendicular to the substrate surface. After the brush layer was annealed at 190ºC for 4 hours, a 1% (w/w) toluene solution of PS-b-PMMA [Polymer Source Inc. Molecular Weight: 46 kg/mol for PS and 21 kg/mol for PMMA, polydispersity index (PDI) of 1.09] was spin-coated onto a pretreated wafer at 4000 rpm and then annealed at 190 °C under vacuum for more than 24 hours. The

polymer was then exposed with UV irradiation (wavelength = 254 nm; intensity= 1 Joule/cm^2) and the exposed PMMA blocks were selectively removed by a subsequent acetic- acid development. The resulting template was a 35 nm-thick PS film perforated with nanoscopic vertically-orientated cylindrical holes, uniformly across the entire GaAs wafer.

After the BCP template formation, a short oxygen (O$_2$) plasma RIE step, typically 6-8 sec at a power of 150 W, was utilized to break through the brush layer within each hole and thus expose the GaAs surface for Ni electrodeposition. The wafer was then cleaved into 1×1 cm^2 pieces to accommodate our electrodeposition apparatus. The Ni electrodeposition was performed in a plating cell using a Ni foil (99%) as the anode, and the highly doped GaAs substrate as the cathode. The Ni electrodeposition bath was a commercially available, nickel sulfamate [Ni(NH$_2$SO$_3$)$_2$] solution (Transene, Inc.) consisting of 20-30% (w/w) nickel sulfamate, 1-5% boric acid, and < 1% nickel chloride. The bath temperature was maintained at a temperature of ~50ºC and a pH of ~ 4. A constant current density of 25-125 μA/cm^2 was used, and the deposition time was estimated based on Faraday's law, in order to avoid overfilling the holes. Finally, following the Ni electrodeposition, the PS template was removed by O$_2$-plasma RIE, leaving behind an ultra-dense, large-area Ni nanopillar array on the substrate. LEO 1530 VP, high-resolution scanning electron microscopy (SEM) was used to characterize the self-assembled BCP-based templates and the fabricated Ni nanopillar arrays.
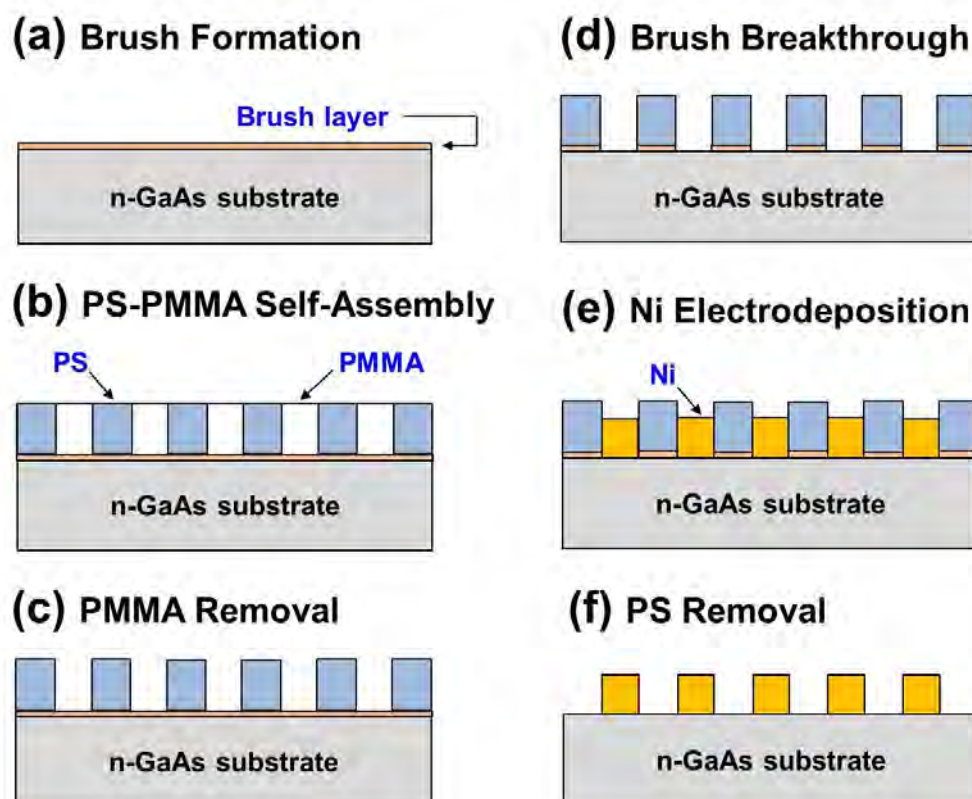
Figure 6.4. A schematic of the process flow for fabricating Ni nanopillar arrays on n-GaAs substrates: (a) neutral brush layer formation by spin coating; (b) PS-b-PMMA diblock copolymer self-assembly on the brush layer; (c) selective removal of PMMA cylinders by UV exposure and acetic-acid development; (d) removal of the brush layer within each hole of the PS template using O_2 plasma reactive ion etching (RIE) to expose the highly-doped GaAs surface for Ni electrodeposition; (e) Ni nanopillars formation within each hole of the PS template by electrodeposition; and (f) removal of PS template using O_2 plasma, leaving behind Ni nanopillar arrays on n-GaAs substrates.

6.5 Results

Figure 6.5(a) shows a plane-view SEM micrograph of the PS template formed on GaAs substrates after the PMMA blocks were removed by UV exposure and acetic-acid development. As can be seen, the prepared template exhibits a high degree of uniformity of nanoscopic holes over a large surface area. The holes are hexagonally arranged with a short-range lateral ordering over regions of 0.25-1 μm separated by grain boundaries. Each hole in the PS matrix, as shown in Figure 6.5(b), is round with a diameter of ~18 nm, and the hole center-to-center spacing, or the pitch, is ~ 34 nm. As reported elsewhere [25], a key process-step to achieving a well-ordered template morphology, including uniform distribution of the hole size and reduced hole eccentricity, is to maintain an optimal film thickness (35 nm in this work) of PS-b-PMMA polymer close to its hole center-to-center spacing value (i.e.,~ 34 nm). In Figure 6.5(c), a low-magnification SEM image of a large area (~ 3.2 μm × 2.4 μm) of the fabricated Ni nanopillar arrays is presented. The resulting Ni nanopillar arrays are well replicated from the PS template, possessing a fundamental hexagonal symmetry within each grain as well as uniform distribution of nanopillar size throughout the entire surface area. The Ni nanopillars shown in a high-magnification SEM [Figure 6.5(d)] exhibit a circular cross-section of an average diameter of ~ 24 nm. The Ni nanopillars are ~ 25 nm in height as measured from tilted-view SEM micrographs [Figure 6.6(a) and (b)]. Few Ni nanopillars are observed to be slightly coalesced [Figure 6.5(d)], and this imperfection is probably due to the fact that the holes were broadened and merged to their respective neighboring holes due either to lateral etching in the O_2-plasma RIE step, for brush-layer removal, or to defects formed in

the initial BCP self-assembly process. Based on the SEM images, the fabricated Ni nanopillar arrays are estimated to have a pillar density close to 10^{11}/cm^2.
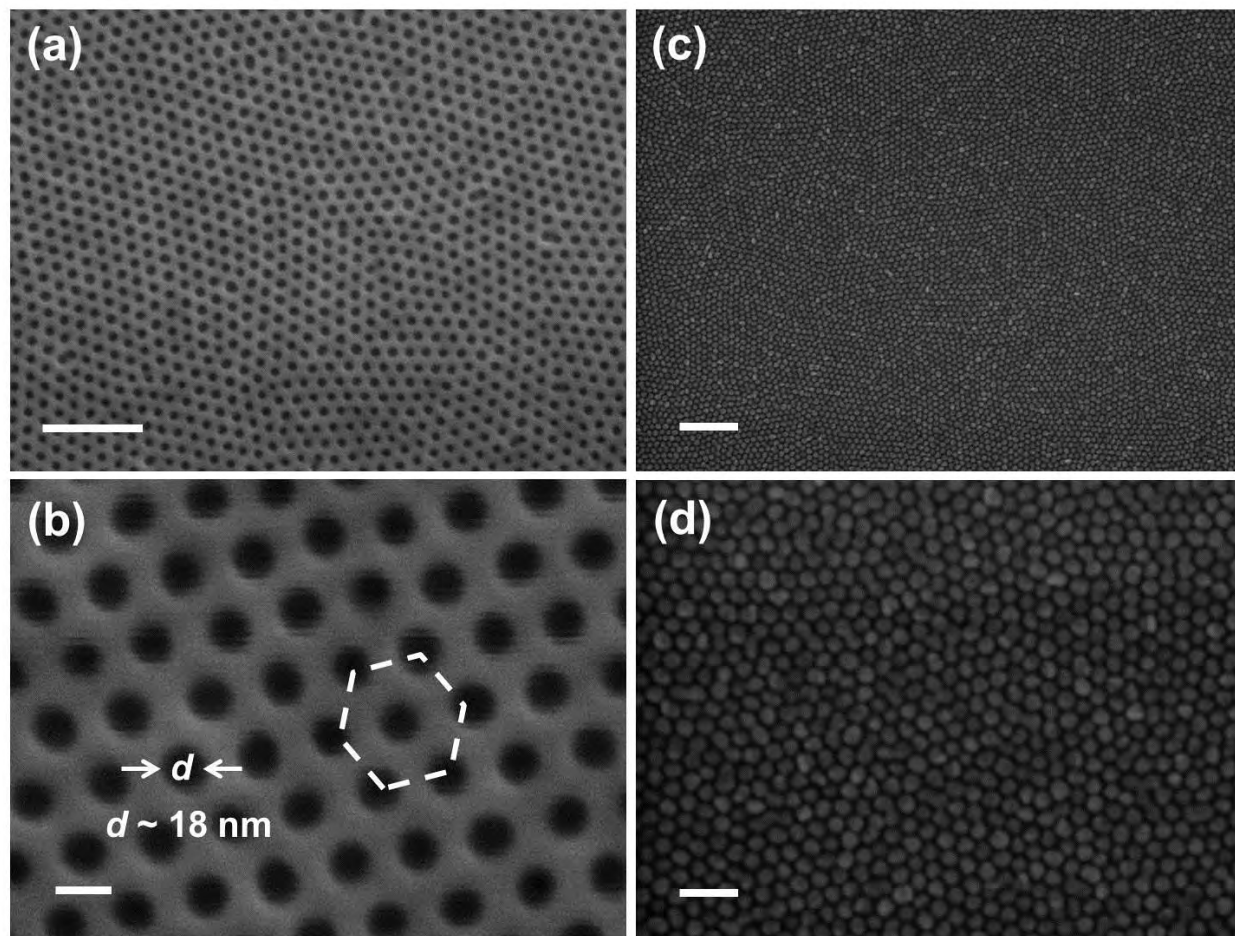
Figure 6.5. Plane-view scanning electron micrograph (SEM) images of: (a) large-area PS template on a n-GaAs substrate after selective removal of PMMA cylinders; (b) the PS template at higher magnification, with holes hexagonally arranged, of ~18 nm diameter and a center-to-center spacing of ~34 nm; (c) large-area fabricated Ni nanopillar arrays on a n-GaAs substrate; and (d) the fabricated Ni nanopillar arrays at higher magnification. Scale bars are (a) 200 nm, (b) 20 nm, (c) 300 nm, and (d) 100 nm wide.
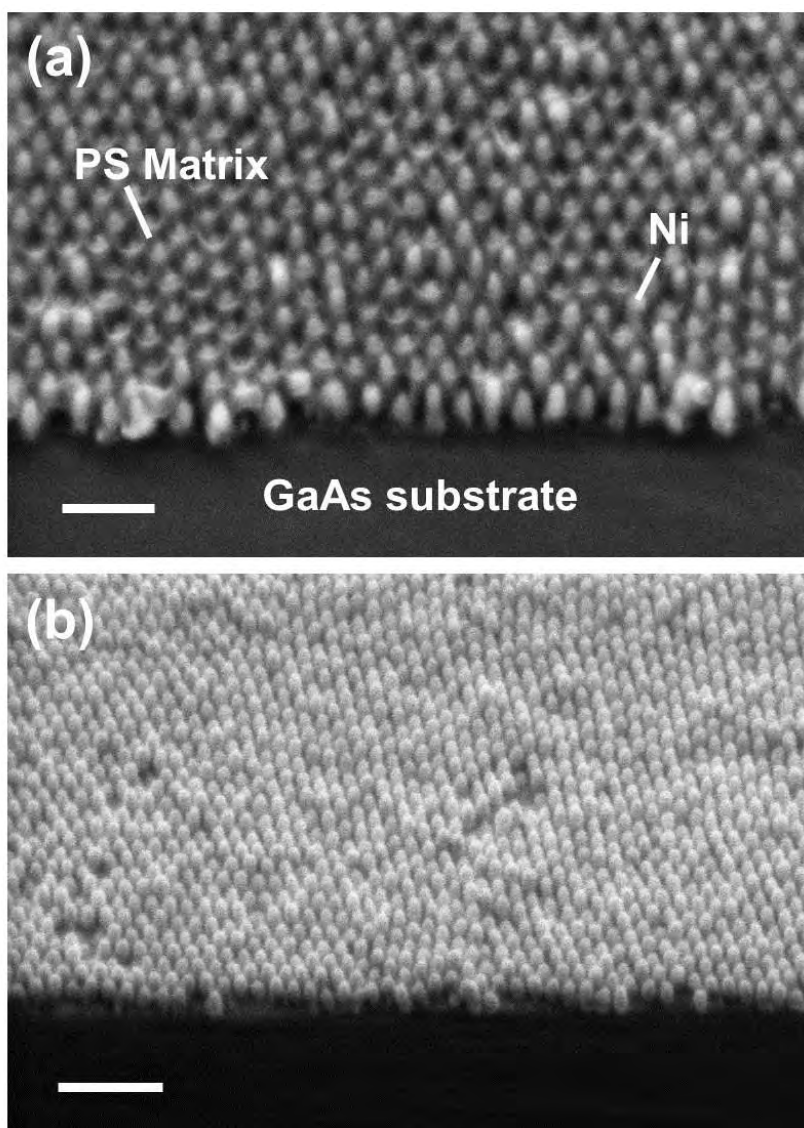
Figure 6.6. (a) Tilted SEM image of PS template after Ni electrodeposition. (b) Tilted SEM image of Ni nanopillar arrays after PS removal via O_2 plasma. Scale bars are: (a) 100 nm, and (b) 200 nm wide.

6.6 Discussion

Over the past two decades, various approaches to the template-based fabrication of metallic nanostructures have been highly developed, by employing various patterning techniques such as e-beam lithography and nanoporous anodic-aluminum-oxide (AAO) templates. In the case of e-beam lithography, Krauss *et al*. [26] and Xu *et al*. [27] reported in their studies on the fabrication of Ni nanopillar arrays with a density of 65 Gbits/in^2 on Si substrates using a silicon dioxide or PMMA template defined by e-beam lithography and Ni electrodeposition. While e-beam lithographic patterns with an ultrahigh density of one terabit/in^2 (1 Tbit/in^2 = 1.55× 10^{11}/cm^2) or higher have recently been demonstrated [28] for magnetic-recording applications, the pattern areas are nonetheless restricted to a relatively small area, often of the order of square micrometers. The nanoporous AAO template, on the other hand, can be prepared at a full-wafer scale with a well-ordered hexagonal array of nanopores. The smallest interpore distances that can be achieved, depending on the electrolytes and anodization parameters, are in general about 50- 60 nm range [29]. This is equivalent to a maximum areal density of only ~ 3× 10^{10}/cm^2. The AAO process also involves additional process steps over the present BCP-based process. In contrast to these results, by using BCP templates, the Ni nanopillar arrays in this work achieve both a high areal density of ~ 10^{11}/cm^2 as well as a large patterned area up extendable to a full wafer. Furthermore, the fabrication method reported here, similar to the fabrication scheme proposed by Park *et al*. [30], the work by Asakura *et al*. [31], and elsewhere [32], involves only few processing steps, which is simpler and more cost-effective compared to other top-down approaches as well as to the self-assembled BCP liftoff process.

The distribution of the diameter of holes in the PS matrix and the diameter of the fabricated Ni nanopillars were determined. Figures 6.7 (a) and (b) present the statistics of the diameter of holes in the PS matrix after acetic-acid development and after brush-layer removal using 8 sec of 150 W O_2-plasma RIE, respectively. Figure 6.7(c) shows the distribution of the diameter of Ni nanopillar arrays after removing the PS template. Gaussian fittings were also performed and plotted to extract the mean value and the standard deviation for each distribution. As seen from Figures 6.7(a) and 6.7(b), the holes in PS template are broadened during the O_2-plasma step, from a mean diameter of 18 nm (standard deviation = 2.2 nm) to 24 nm (standard deviation = 2.9 nm). This hole broadening is due to the duration and isotropy of the O_2-plasma RIE step. On the other hand, the fabricated Ni nanopillar arrays appear to have a similar mean diameter after brush removal, albeit with a slightly increased standard deviation of 5.8 nm [Figure 6.7(c)]. Hence, it is evident that the brush-layer removal step has a significant impact on the diameter of the fabricated Ni nanopillars. To tailor the diameter of these Ni nanopillars, one possible method is to adjust the O_2-plasma etching time necessary for removing the brush layer. For example, Figure 6.7(d) shows a plane-view SEM image of the PS template after only 6 sec of O_2-plasma RIE and the corresponding statistical parameters. The holes in the template possess a smaller mean diameter of ~ 21 nm after the shorter plasma exposure, which consequently results in a Ni nanopillar array with a similar small diameter, as shown in Figure 6.7(e). Therefore, without changing the molecular weight ratios of the PS-b-PMMA BCP for different hole diameters and pitches, here we show that we can fabricate Ni nanopillar arrays with modulated diameters by tuning the O_2-plasma etching time in the brush-layer removal step.
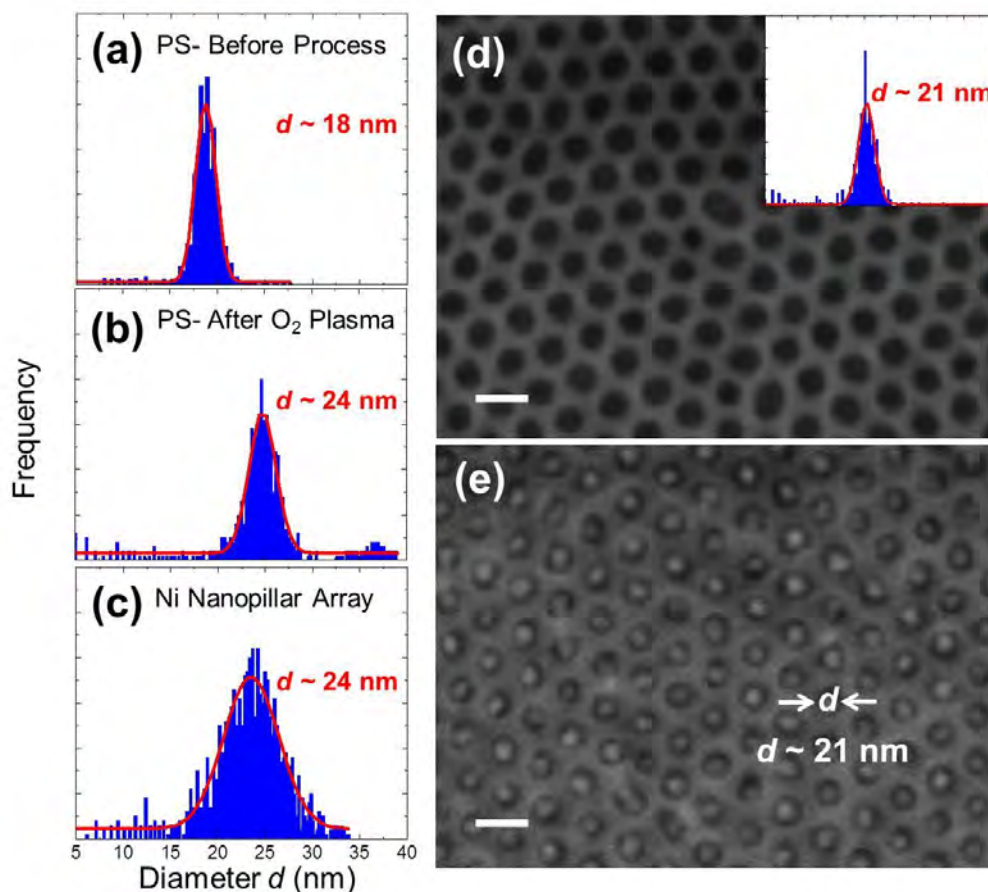
Figure 6.7. The hole-diameter distribution of the PS template after: (a) PMMA cylinder removal; (b) 8 sec of 150-W, O_2-plasma RIE to remove the brush layer within each hole; and (c) the Ni-nanopillar diameter distribution after removing the PS template [see Fig. 2(d)]. The red curves in (a)-(c) are computed Gaussian fitting curves, for which the calculated mean diameters are 18, 24, and 24 nm, respectively. (d)-(e) Plane-view SEM images of the PS template after only 6 sec of 150-W, O_2-plasma RIE for brush removal before and after Ni electrodeposition. The mean diameter of the holes in the PS template [inset in (d)] is ~ 21 nm. Scale bars are 40 nm wide.

In early experiments, we also attempted to electrodeposit Ni into the nanoscale holes of PS templates prepared on a 5 nm-thick Ni conductive seed layer which had been evaporated on GaAs substrates. However, Ni electrodeposition occurred only in a few holes over the entire PS template. As shown in Figure 6.8(a), most of the holes in the template remained empty (holes with a darker contrast under SEM) after the Ni electrodeposition, whereas a few holes were overfilled with Ni (brighter contrast). A similar behavior was also observed when the electrodeposition was carried out right after a brief acid dip of the sample, in order to activate the surface of the Ni seed layer. Based on these results, we believe that an insulating layer was formed on the Ni seed layer surface, probably due to the oxidation of the Ni seed layer during the O_2-plasma RIE step. This insulating layer inhibits the charge transfer between the Ni sulfamate solution and the seed layer. In order to circumvent this problem, a short *in-situ* electrochemical etch step was performed prior to the Ni electrodeposition by reversing the polarity of the electrodes in our plating cell. Figures 6.8(b)− 5(d) highlight the results of the Ni electrodeposition after an *in-situ* etch step (reverse current = 25 µA) using a plating-current density of 25, 100, and 125 µA/cm^2, for the same deposition time, respectively. At a current density of 25 µA/cm^2 [Figure 6.8(b)], although Ni was found in a majority of holes, the hole-filling was fairly poor and non-uniform across the entire PS template. At larger plating currents, the hole-filling seemingly improved, with some Ni nanopillars appearing to be higher, indicative of a high local current density. At yet larger plating currents, a non-uniform Ni nanopillar array was obtained [Figure 6.8(c)]; however larger plating current led to higher areal density of irregular Ni islands randomly scattered over the area [Figure 6.8(d)]. Therefore, it clearly appears that Ni-nanopillar-array formation

by electrodeposition into PS-template holes having a seed layer is unfavorable for the purpose of achieving uniform nanostructures over a large surface area or at full-wafer scale due to the presence of the initial oxidized Ni surface and the complications in the uniform removal of this insulating layer.
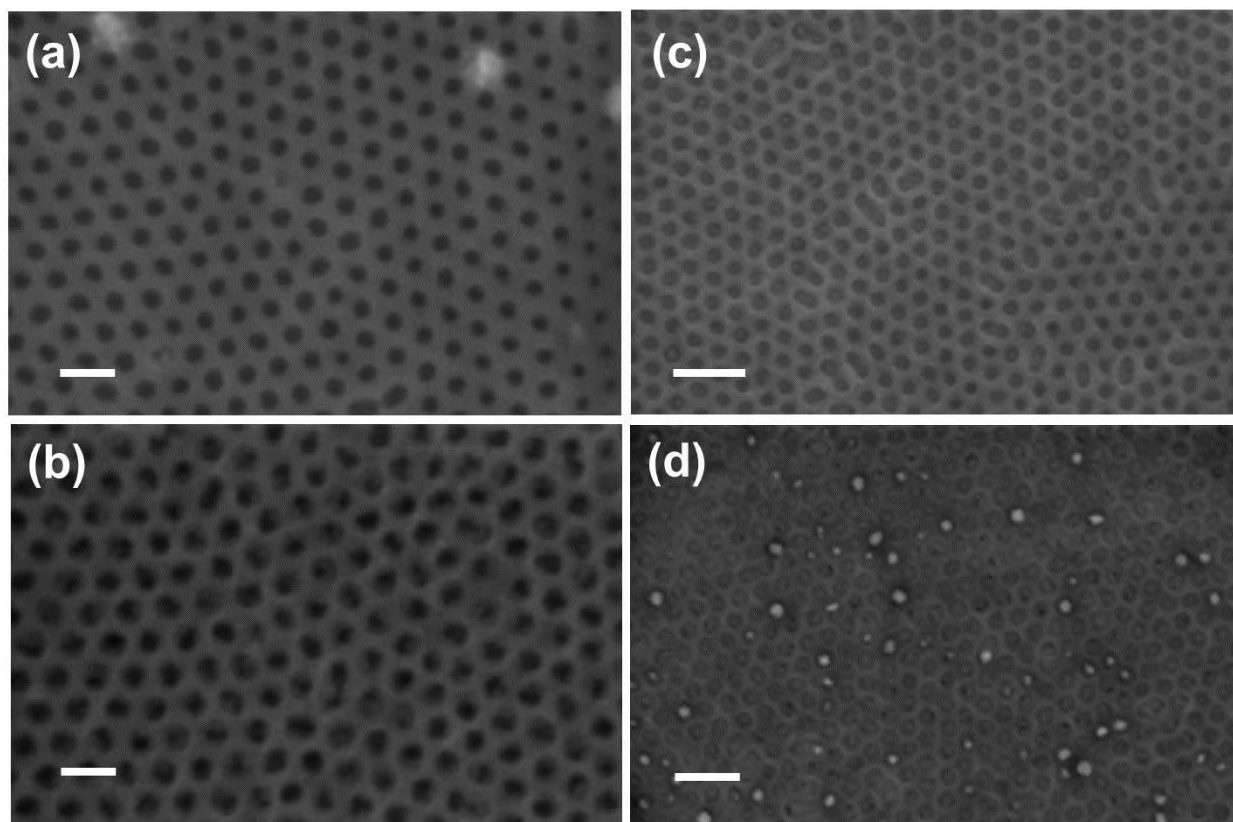
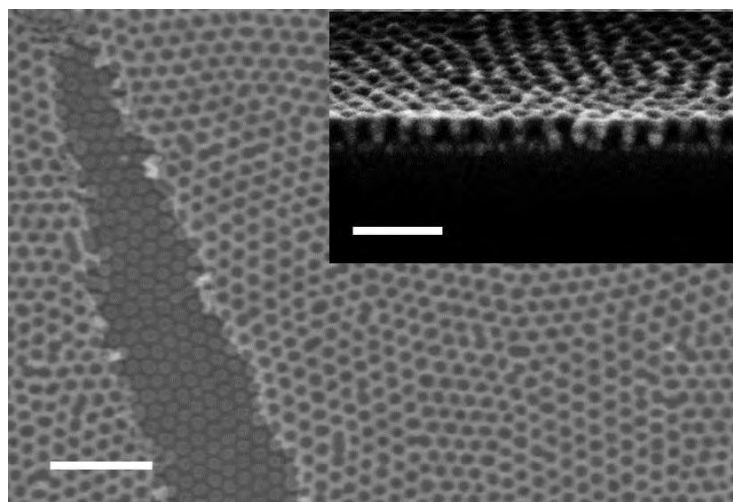**Figure 6.8**. Plane-view SEM image of PS templates prepared on a 5 nm-thick Ni, conductive seed layer evaporated on GaAs substrates (a) after Ni electrodeposition at a plating current density of 25 $\mu A/cm^2$; and (b)-(d) after an *in-situ* etch step and Ni electrodeposition at a plating current density of 25, 100, and 125 $\mu A/cm^2$, respectively. Scale bars are (a) 50 nm, (b) 50 nm, (c) 100 nm, and (d) 100 nm wide.

The present electrodeposition process combined with BCP patterning does have advantages over the metal liftoff process that also involves BCP templates. The present process ensures the fidelity of pattern transfer which can often be difficult when employing a top-down process involving RIE, i.e. using a BCP template as an etch mask. A reproducible metal pattern using BCP templates as a metal liftoff mesh requires the BCP template to be several times thicker than the deposited metal, and the holes in the template need to have a reentrant sidewall profile, in order to facilitate the template removal. These requirements are in general not met with BCP templates. Park *et al.* [30] and Vedrine *et al.* [33] both implemented a trilayer scheme to fabricate large-area periodic gold (Au) nanodot arrays on Si substrates by integrating additional dielectric and polyimide layers with BCP to increase the aspect ratio of the liftoff template. Gowrishankar *et al.* [34] addressed this problem by using an oblique-angled argon (Ar) sputter-etch step to etch away the undesirable metal over-coated onto the template sidewall before liftoff. Shin *et al.* [22] removed the excess metal and the PS template with the assistance of a series of steps including sonication, UV irradiation, and O_2 RIE. These publications offer approaches to overcome the aforementioned difficulties; however, at the expense of an enhanced complexity of the metal-liftoff process when based on BCP templates. By way of comparison to the electrodeposition approach, samples were prepared via e-beam deposition of a 3 nm-thick Ni onto a PS template on GaAs, after removal of the brush layer. The sample surface was held normal to the metal-vapor flux. After Ni deposition, the template removal was carried out by immersion in a III-V compatible solvent, [N-methylpyrrolidone (NMP)] at 75 ℃, with constant sonication for 1.5 hours, followed by room-temperature UV-Ozone exposure for an hour.

Results of this metal liftoff process are seen in Figure 6.9. The process resulted in a Ni-coated PS template over most of the sample except in small isolated regions. The thickness of the PS template was ~30 nm after O_2-plasma RIE and the evaporated Ni was about only one tenth the PS height. Therefore, the result here suggests that the underlying cause of the liftoff problem is the absence of a reentrant PS sidewall profile [Figure 6.9 inset], in agreement with the work by Kang *et al*. [35].

Utilizing the same PS templates, the electrodeposited Ni nanopillars reported on in this work can reach heights up ~ 25 nm [Figure 6.6(b)] and the template can easily be removed in an aqueous solvent or O_2 plasma. Thus, the use of electrodeposition combined with BCP templates appears to be a quite robust route to fabricating large-area, ultra-dense periodic metallic nanostructures with a higher aspect-ratio at sub-50 nm scales.

Figure 6.9. Plane-view SEM image of a PS template on a GaAs substrate after e-beam evaporation of 3 nm of Ni and liftoff. Inset: tilted SEM image of the PS template after brush-layer removal within each hole (scale bar corresponds to 100 nm). Scale bars are 200 nm wide.

6.7 Conclusion

In summary, the fabrication of Ni nanopillar arrays on GaAs substrates employing diblock copolymer lithography and Ni electrodeposition has been demonstrated. The fabricated Ni nanopillar arrays, have an average diameter of 24 nm, a density of about $10^{11}/cm^2$, and are formed over an area of 1 cm ×1 cm. These results are among the largest, highly dense metal-nanopillar arrays with a feature size of sub-30 nm fabricated on III-V semiconductor substrates. These arrays could be used in other pattern-transfer processes, such as in the process for making quantum boxes or quantum dots in the active region of IQB lasers. They could also serve as nanostructures in their own right. This process presented here provides a generalized method of forming such arrays of metal nanopillar.

Reference

[1] U. Bockelmann and G. Bastard. "Phonon scattering and energy relaxation in two-, one-, and zero-dimensional electron gases", *Phys. Rev. B*, **42**, 8947-8951 (1990).

[2] U. Bockelmann. "Exciton relaxation and radiative recombination in semiconductor quantum dots", *Phys. Rev. B*, **48**, 637-640 (1993).

[3] E. A. Zibik, L. R. Wilson, R. P. Green, G. Bastard, R. Ferreira, P. J. Phillips, D. A. Carder, J-P. R. Wells, J. W. Cockburn, M. S. Skolnick, M. J. Steer, and M. Hopkinson. "Intraband relaxation via polaron decay in InAs self-assembled quantum dots", *Phys. Rev. B*, **70**, 161305 (2004).

[4] K. Mukai, N. Ohstuka, H. Shoji, and M. Sugawara. "Phonon bottleneck in self-formed $In_xGa_{1-x}As$/GaAs quantum dots by electroluminescence and time-resolved photoluminescence", *Phys. Rev. B*, **54**, R5243-R5246 (1996).

[5] G. Wang, S. Fafard, D. Leonard, J. E. Bowers, J. L. Merz, and P. M. Petroff. "Time-resolved optical characterization of InGaAs/GaAs quantum dots", *Appl. Phy. Lett.*, **64**, 2815-2817 (1994).

[6] X.-Q. Li, H. Nakayama, and Y. Arakawa. "Phonon bottleneck in quantum dots: Role of lifetime of the confined optical phonons", *Phys. Rev. B*, **59**, 5069-5073 (1999).

[7] O. Verzelen, R. Ferreira, and G. Bastard. "Polaron lifetime and energy relaxation in semiconductor quantum dots", *Phys. Rev. B*, **62**, R4809-R4812 (2000).

[8] T. Grange, R. Ferreira, and G. Bastard. "Polaron relaxation in self assembled quantum dots: Breakdown of the semiclassical model", *Phys. Rev. B*, **76**, 241304 (2007).

[9] E. A. Zibik, T. Grange, B. A. Carpenter, N. E. Porter, R. Ferreira, G. Bastard, D. Stehr, S. Winnerl, M. Helm, H. Y. Liu, M. S. Skolnick, and L. R. Wilson. "Long

lifetimes of quantum-dot intersublevel transitions in the terahertz range", *Nature Mater.*, **8**, 803-807 (2009).

[10] D. Botez, P. Zory, and C. F. Hsu. "Intersubband quantum box semiconductor laser", *U.S. Patent*, **5**, 5,953,356 (1999).

[11] C.-F. Hsu, O Jeong-Seok, P. Zory, and D. Botez. "Intersubband quantum-box semiconductor lasers", *IEEE J. Sel. Top. Quantum Electron.* **6(3)**, 491-503 (2000).

[12] G. Tsvid, M. D'Souza, D. Botez, B. Hawkins, A. Khandekar, T. Kuech, and P. Zory. "Towards intersubband quantum box lasers: Electron-beam lithography update", *J. Vac. Sci. Technol. B*, **22**, 3214 (2004).

[13] D. Botez, G. Tsvid, M. D'Souza, M. Rathi, J. C. Shin, J. Kirch, L. J. Mawst, T. Kuech, I. Vurgaftman, J. Meyer, J. Plant, and G. Turner. "Progress towards intersubband quantum-box lasers for highly efficient continuous wave operation in the mid-infrared", *J. Nanophoton.* **3**, 031606 (2009).

[14] D. Botez, G. Tsvid, M. D'Souza, J. C. Shin, Z. Liu, J. H. Park, J. Kirch, L. J. Mawst, M. Rathi, T. F. Kuech, I. Vurgaftman, J. Meyer, J. Plant, G. Turner, and P. Zory. "Intersubband quantum-box lasers: Progress and potential as uncooled mid-infrared sources", Chapter in *Future Trends in Microelectronics: From Nanophotonics to sensors to energy*, p. 49-64, Wiley-IEEE Press, June 2010.

[15] A. Tredicucci. "Long life in zero dimensions", *Nature Mater.*, **8**, 775-776 (2009).

[16] D. Wasserman and S. A. Lyon. "Midinfrared luminescence from InAs quantum dots in unipolar devices", *Appl. Phy. Lett.*, **81**, 2848-2850 (2002).

[17] C. H. Fischer, P. Bhattacharya, and P.-C. Yu. "Intersublevel electroluminescence from $In_{0.4}Ga_{0.6}As$ quantum dots in quantum cascade heterostructure with GaAsN/GaAs superlattice", *Electron. Lett.*, **39**, 1537-1538 (2003).

[18] I. W. Hamley. "Nanostructure fabrication using block copolymers", **14**, R39 (2003).

[19] J. Bang, U. Jeong, D. Y. Ryu, T. P. Russell, and C. J. Hawker. "Block copolymer nanolithography: Translation of molecular level control to nanoscale patterns", *Adv. Mater.*, **21**, 4769 (2009).

[20] T. F. Kuech and L. J. Mawst. "Nanofabrication of III-V semiconductors employing diblock copolymer lithography", *J. Phys. D*, **43**, 183001 (2010).

[21] K. Liu, S. M. Baker, M. Tuominen, T. P. Russell, and I. K. Schuller. "Tailoring exchange bias with magnetic nanostructures", *Phys. Rev. B*, **63**, 060403(R) (2001).

[22] K. Shin, K. A. Leach, J. T. Goldbach, D. H. Kim, J. Y. Jho, M. Tumoinen, C. J. Hawker, and T. P. Russell. "A simple route to metal nanodots and nanoporous metal films", *Nano Lett.*, **2**, 933 (2002).

[23] A. J. Hong, C. C. Liu, Y. Wang, J. Kim, F. Xiu, S. Ji, J. Zou, P. F. Nealey, and K. L. Wang. "Metal nanodot memory by self-assembled block copolymer lift-off", *Nano Lett.*, **10**, 224 (2010).

[24] C. Scheck, P. Evans, R. Schad, G. Zangari, L. Sorba, G. Biasiol, and S. Heun. "Selective metal electrodeposition through doping modulation of semiconductor surfaces", *Appl. Phy. Lett.*, **86**, 133108 (2005).

[25] K. W. Guarini, C. T. Black, and S. H. I. Yeung. "Optimization of diblock copolymer thin film self assembly", *Adv. Mater.*, **14**, 1290 (2002).

[26] P. R. Krauss, P. B. Fischer, and S. Y. Chou. "Fabrication of singledomain magnetic pillar array of 35 nm diameter and 65 Gbits/in.^{2} density", *J. Vac. Sci. Technol. B*, **12**, 3639 (1994).

[27] W. Xu, J. Wong, C. C. Cheng, R. Johnson, and A. Scherer. "Fabrication of ultrasmall magnets by electroplating", *J. Vac. Sci. Technol. B*, **13**, 2372 (1995).

[28] J. K. W. Yang, Y. Chen, T. Huang, H. Duan, N. Thiyagarajah, H. K. Hui, S. H. Leong, and V. Ng. "Fabrication and characterization of bit-patterned media beyond 1.5 Tbit/in^2", *Nanotechnology*, **22**, 385301 (2011).

[29] K. Schwirn, W. Lee, R. Hillebrand, M. Steinhart, K. Nielsch, and U. Gösele. "Self-ordered anodic aluminum oxide formed by H_2SO_4 hard anodization", *ACS Nano*, **2**, 302 (2008).

[30] M. Park, P. M. Chaikin, R. A. Register, and D. H. Adamson. "Large area dense nanoscale patterning of arbitrary surfaces", *Appl. Phy. Lett.*, **79**, 257 (2001).

[31] S. Asakura, A. Hozumi, and A. Fuwa. "Fabrication of a Cu nanodot array based on electroless plating employing a diblock copolymer nanotemplate", *J. Vac. Sci. Technol. A*, **23**, 1137 (2005).

[32] S. Anandakumar, V. S. Rani, B. P. Rao, S. S. Yoon, J. R. Jeong, and C. Kim. "Ultra high density nanopore arrays using self assembled diblock copolymer", *IEEE Tran. Magn.*, **45**, 4063 (2009).

[33] J. Vedrine, Y.-R. Hong, A. P. Marencic, R. A. Register, D. H. Adamson, and P. M. Chaikin. "Large-area, ordered hexagonal arrays of nanoscale holes or dots from block copolymer templates", *Appl. Phy. Lett.*, **91**, 143110 (2007).

[34] V. Gowrishankar, N. Miller, M. D. McGehee, M. J. Misner, D. Y. Ryu, T. P. Russell, E. Drockenmuller, and C. J. Hawker. "Fabrication of densely packed, well-ordered, high-aspect-ratio silicon nanopillars over large areas using block copolymer lithography", *Thin Solid Films*, **513**, 289 (2006).

[35] G. B. Kang, S.-I. Kim, Y. T. Kim, and J. H. Park. "Fabrication of metal nano dot dry etching mask using block copolymer thin film", *Curr. Appl. Phys.*, **9**, S82 (2009).